THESIS FOR THE DEGREE OF DOCTOR OF PHILOSOPHY

Enabling technologies for scalable graphene electronics

Naveen Shetty

Department of Microtechnology and Nanoscience (MC2)
Quantum Device Physics Laboratory
Chalmers University of Technology
Gothenburg, Sweden, 2023

Enabling technologies for scalable graphene electronics

NAVEEN SHETTY
ISBN 978-91-7905-955-2

Doktorsavhandlingar vid Chalmers tekniska högskola
Ny serie nr. 5421
ISSN 0346-718X

Department of Microtechnology and Nanoscience (MC2)
Quantum Device Physics Laboratory
Chalmers University of Technology
SE-412 96 Gothenburg, Sweden
Phone: +46 (0)31 772 1000
`www.chalmers.se`

Printed by Chalmers Reproservice
Gothenburg, Sweden, December2023

Dedicated to my beloved mother

Abstract

This thesis addresses the challenges in scaling up graphene-based technologies, with a focus on the epitaxial growth of graphene (epigraphene) over SiC substrates and the establishment of reliable low-contact resistance electrical contacts. The scalable graphene growth and contact fabrication have enabled the development of three epigraphene-based devices, including large-scale Quantum Hall Arrays, highly sensitive Hall effect magnetometers with minimal noise, and quantum-limited ultraviolet (UV) detectors.

Hall sensors utilizing epigraphene with their carrier density tuned close to neutrality, outperform the most advanced graphene-based Hall sensors documented in existing literature. Given the exceptionally high epitaxial growth temperatures (~ 1850 °C) in SiC, crystal imperfections are significantly minimized, leading to remarkably low noise performance. Consequently, SiC-based magnetic field sensors achieve sensitivities of $B_{MIN} = 27$ nT/$\sqrt{\text{Hz}}$ at room temperature. By connecting them in parallel, it is possible to increase the sensitivity even further to $B_{MIN} = 9$ nT/$\sqrt{\text{Hz}}$, setting a new record for lowest magnetic field detection in epigraphene-based Hall sensors.

This thesis demonstrates the largest ever functional quantum Hall arrays with 236-element Hall bars for practical precision resistance metrology. This results in $R_K/236 \approx 109$ Ω with 0.2 part-per-billion (nΩ/Ω) accuracy and critical current $I_C \geq 5$ mA (R_K the von Klitzing constant). An essential aspect of the study involves investigating the long-term stability of molecularly doped epigraphene Quantum Hall Resistance Standard (QHRS) and analyzing the influence of storage conditions and dopants on device stability and performance over a period of 3 years. With a relative deviation of 0.01 %/day in carrier density, the estimated life of these samples is more than 20 years. Molecular dopants are utilized in every epigraphene-based application that requires charge carrier modulation. Hence, this study is essential to understand the long-term stability of real-life applications based on epigraphene.

Furthermore, the technologies developed in this work allowed the exploration of epigraphene as solar-blind UV detectors, using SiC as absorber and graphene as transparent contact, leading to a peak external quantum efficiency (η) of approximately 85 % (limited by reflection losses) for wavelengths (λ) in the range of 250 to 280 nm.

The refinements in epitaxial growth of graphene on SiC and device fabrication strategies have been tested and verified in three applications of epigraphene. Each of them reflects the true scalability of the epigraphene technologies developed in this work and led to devices that surpass conventional material technologies in specific domains. Altogether, the advancements demonstrated in this thesis open up new avenues for the use of epigraphene in multiple practical applications.

Keywords: Graphene, Edge contact, Metrology, Array, Hall effect, 1/f

List of Publications

This thesis includes the following publications:

Paper A **Naveen Shetty**, Hans He, Richa Mitra, Johanna Huhtasaari, Konstantina Iordanidou, Julia Wiktor, Sergey Kubatkin, Saroj P. Dash, Rositsa Yakimova, Lunjie Zeng, Eva Olsson, Samuel Lara-Avila. "Scalable Fabrication of Edge Contacts to 2D Materials: Implications for Quantum Resistance Metrology and 2D Electronics." ACS Applied Nano Materials 6, no. 7 (2023): 6292-6298.

Paper B Hans He, **Naveen Shetty**, Thilo Bauch, Sergey Kubatkin, Timo Kaufmann, M. Cornils, Rositsa Yakimova, and Samuel Lara-Avila. "The performance limits of epigraphene Hall sensors doped across the Dirac point." Applied Physics Letters 116, no. 22 (2020)

Paper C Hans He, **Naveen Shetty**, Sergey Kubatkin, Pascal Stadler, Tomas Löfwander, Mikael Fogelström, José Carlos Miranda-Valenzuela, Rositsa Yakimova, Thilo Bauch, and Samuel Lara-Avila. "Highly efficient UV detection in a metal–semiconductor–metal detector with epigraphene." Applied Physics Letters 120, no. 19 (2022).

Paper D Hans He, Karin Cedergren, **Naveen Shetty**, Samuel Lara-Avila, Sergey Kubatkin, Tobias Bergsten, and Gunnar Eklund. "Accurate graphene quantum Hall arrays for the new International System of Units." Nature Communications 13, no. 1 (2022): 6933.

Paper E **Naveen Shetty**, Tobias Bergsten, Gunnar Eklund, Samuel Lara-Avila, Sergey Kubatkin, Karin Cedergren, and Hans He. "Long-term stability of molecular doped epigraphene quantum Hall standards: single elements and large arrays ($R_K/236 \approx 109\ \Omega$)." Metrologia (2023).

Paper F **Naveen Shetty**, Federico Chianese, Hans He, Johanna Huhtasaari, Shima Ghasemi, Kasper Moth Poulsen, Sergey Kubatkin, Thilo Bauch, Samuel Lara Avila. "Ultra low 1/f noise in epigraphene devices" (Submitted)

Publications not included in this thesis:

Paper G Konstantina Iordanidou, Richa Mitra, **Naveen Shetty**, Samuel Lara-Avila, Saroj Dash, Sergey Kubatkin, and Julia Wiktor. "Electric field and strain tuning of 2D semiconductor van der Waals heterostructures for tunnel field-effect transistors." ACS Applied Materials & Interfaces 15, no. 1 (2022): 1762-1771.

Paper H Filippo Fabbri, Manuela Scarselli, **Naveen Shetty**, Sergey Kubatkin, Samuel Lara-Avila, Mathieu Abel, Isabelle Berbezier et al. "Silicene nanosheets intercalated in slightly defective epitaxial graphene on a 4H-SiC (0001) substrate." Surfaces and Interfaces 33 (2022): 102262.

Paper I Bayan Karimi, Hans He, Yu-Cheng Chang, Libin Wang, Jukka P. Pekola, Rositsa Yakimova, **Naveen Shetty**, Joonas T. Peltonen, Samuel Lara-Avila, and Sergey Kubatkin. "Electron-phonon coupling of epigraphene at millikelvin temperatures measured by quantum transport thermometry." Applied Physics Letters 118, no. 10 (2021).

Paper J Karsten Hinrichs, **Naveen Shetty**, Sergey Kubatkin, Per Malmberg, Samuel Lara-Avila, Andreas Furchner, and Jörg Rappich. "Field Manipulation of Band Properties in Infrared Spectra of Thin Films." Advanced Photonics Research (2023): 2300212.

Acknowledgments

I am deeply grateful to my supervisor Samuel Lara for his invaluable guidance, support, and mentorship throughout this research journey. Your insightful advice, expertise, and constructive feedback have significantly contributed to my personal and professional growth. I am fortunate to have had the opportunity to work with you, and I will always cherish the valuable lessons and insights you have imparted to me during our visits to Process Lab 3. My sincere appreciation also goes to my co-supervisor at RISE, Hans He for his insightful contributions and continuous engagement in my work. Thank you for offering a helping hand whenever I needed one in the cleanroom, as well as for instructing me in the nuances of metrology. I extend my gratitude to the esteemed examiner Sergey Kubatkin for providing me the opportunity to work in this group. Your thorough evaluation and valuable feedback significantly enriched the quality of this work. I hope my work has reached your expectations and will help the future researchers in the group.

I would like to acknowledge the contributions of my dedicated group members: Kyong Ho Kim, Johanna Huhtasaari, Federico Chianese, Aditya Jayaraman, Andrey Danilov, and Richa Mitra, whose collaboration and teamwork have been integral to the successful completion of this thesis. My heartfelt thanks to Saroj Prasad Dash, Thilo Bauch, and August Yurgens for their support and encouragement during this research endeavor. I extend my gratitude to Tobias Bergsten, Gunner Eklund, and Karin Cedergren from RISE for their support and collaboration with our group. I am grateful to Lunjie Zeng and Eva Olsson for their assistance with the TEM analysis, which greatly enriched the findings of this study.

Most of the research work is carried out in the cleanroom and laboratories in Chalmers, which are well equipped and maintained, thanks to the dedicated staff who ensure the smooth operation of tools and machinery. My sincere appreciation to Niclas Lindvall, Marcus Rommel, Alexei Kalaboukhov, Bengt Nilsson, Mats Hageberg, Henrik Fredriksen, and Jhon Andersson for their assistance and support in the cleanroom facility.

I am deeply indebted to the European Union's Horizon 2020 research and innovation program under the Marie Sklodowska-Curie Grant Agreement No. 766025 (QuesTech), for funding most of the research work and providing the opportunity to collaborate with a diverse group of researchers across Europe. Special thanks to David Wander from CNRS-Grenoble, for his expertise in the development of the Python script, which was instrumental in the data analysis process. I would also express my gratitude to Diego Subero and Vivek Sharma, individuals I encountered on this journey, for offering moral support throughout this five-year period.

Lastly, I wish to extend my sincere gratitude to all the individuals from the QDP group, especially Alessia Garibaldi, Núria Alcalde Herraiz, Lars Sjöström, Munis Khan, Kiryl Niherysh, Roselle Ngaloy, and Anamul Md Hoque, for accompanying me in excursions and adventures and for being my partners in crime. My journey over the past five years would not have been as lively and fulfilling without your companionship.

Acronyms

2D	two-dimensional
ADC	Analog to Digital Converter
AFM	Atomic Force Microscopy
BL	bilayer
BZ	Brillouin Zone
CCC	Cryogenic Current Comparator
CVD	Chemical Vapor Deposition
DOS	Density of States
EBL	Electron Beam Lithography
EELS	Electron Energy Loss Spectroscopy
F4TCNQ	2, 3, 5, 6-Tetrafluoro-tetracyanoquinodimethan
FWHM	Full-Width Half Maximum
LEED	Low-Energy Electron Diffraction
LL	Landau Level
ML	monolayer
MSM	Metal-Semiconductor-Metal
NEP	Noise Equivalent Power
PMMA	Poly(methyl-methacrylate)
PSD	Power Spectral Density
QHA	Quantum Hall Array
QHARS	Quantum Hall Array Resistance standard
QHE	Quantum Hall Effect
QHRS	Quantum Hall Resistance Standard
SQUID	Superconducting Quantum Interference Device
STEM	Scanning Transmission Electron Microscopy
TEM	Transmission Electron Microscopy
TLM	Transfer Length Method
UV	Ultraviolet
vdP	van der Pauw
vdW	van der Waals

Contents

III Appendices 115

IV Papers 125

I Overview

CHAPTER 1

Introduction

1.1 Graphene

Graphene, a two-dimensional (2D) material (Figure 1.1), has been a focal point of scientific research and technological innovation since its discovery. It possesses an array of properties that make it a captivating subject across various disciplines, from physics and materials science to electronics, nanotechnology, composites, coatings, and energy storage.

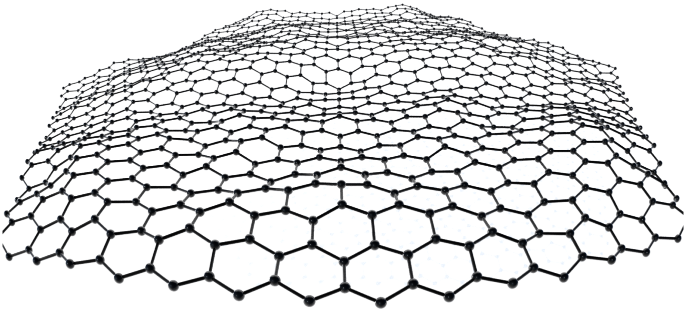

Figure 1.1: Rendered image of graphene sheet

In terms of electronic properties, graphene does not have a band gap and its charge carrier density can be tuned by an externally applied electric field. Graphene's linear dispersion relation at low Fermi energies leads to effectively massless carriers which result in exceptionally high carrier mobilities with a speed of about $c/300 \approx 1 \times 10^6$ m/s. This results in room temperature mobilities up to 2.5×10^5 cm^2/(Vs) in specially prepared samples [1], which is two orders larger compared to silicon ($\approx 1.5 \times 10^3$cm^2/(Vs)) [2]. As for the optical properties, due to zero bandgap, graphene absorbs light in a broad range of frequencies, and its optical absorption is defined by the fine structure constant α as $\pi\alpha = 2.3$ % [3]. Graphene is the thinnest material (0.34 nm) stable at room temperature and ambient conditions, it has a large specific surface area making it attractive for sensing applications. Additionally, it exhibits a thermal conductivity of $\sim 2 - 4 \times 10^3$ W/(mK) [4], [5], outperforming copper by an order in magnitude while being lighter. These properties make graphene highly attractive for a number of applications, including electrical, chemical, photonics, and biological applications.

Ever since the Nobel Prize in physics was awarded to research in Graphene in 2010, it has opened the floodgates for researchers to exploit graphene's remarkable properties to develop inventions that surpass existing technologies. Even though many succeeded in demonstrating the exceptional properties of graphene in laboratory settings, it is still a challenge to integrate graphene into scalable applications.

This thesis demonstrates that the SiC platform provides a solution for scalable growth, interface, doping, contact, and design, addressing several challenges listed in the integration of graphene with existing technology [6], [7].

1.2 Choosing the right graphene

At present, there are essentially two ways to produce monolayer (ML) graphene over large scale [8], [9]: Chemical Vapor Deposition (CVD), and epitaxial growth. In the CVD synthesis method, it is possible to grow up to a 100-meter scale using roll-to-roll apparatus [10]. Graphene produced in this way tends to be polycrystalline with typical domain sizes limited below 300 µm. Recent developments in the CVD growth process do result in millimeter-sized graphene single crystals but have limited coverage with randomly positioned domains making them unsuitable for large-scale device production [11]. Another challenge with this technique is the direct growth on insulating substrates. Usually, the graphene is grown over metallic substrates (like Cu, Ni) because the growth rate is extremely slow and nonuniform over insulating substrates [12].

Epitaxial growth of graphene on silicon carbide (epigraphene) is a promising technology where single crystalline monolayer graphene can be epitaxially grown over Si face (0001) of the silicon carbide (SiC) substrate [13]–[15]. Epitaxial graphene is grown primarily on hexagonal polytypes, 6H-SiC or 4H-SiC (≈ 3.3 eV bandgap). Since graphene is grown directly over an insulating substrate it eliminates the need for the transfer of grown graphene and allows direct fabrication of electronic devices over the SiC.

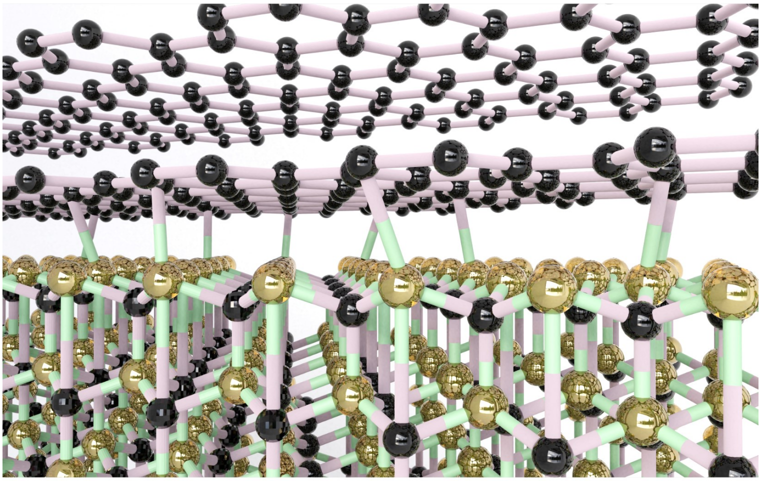

Figure 1.2: Rendered image of epitaxial graphene, buffer layer over SiC substrate. Top most honeycomb lattice represents epitaxially grown graphene, the middle layer represents the buffer layer, SiC substrate is shown with carbon (black) and Si (yellow) atoms.

1.3 Motivation of the thesis

This thesis addresses the solutions to the scalability of graphene-based technologies, exploring the epitaxial growth on the SiC platform. This results in:

- Scalable material with uniform properties, produced in up to 4-inch substrates.
- Robust and scalable formation of electrical contacts with low contact resistance, required to demonstrate devices with exceptional performance.

Research in this thesis starts with optimizing the epitaxial growth of graphene over SiC substrate. The growth of epitaxial graphene on Si (0001) face of 4H-SiC is not a self-limiting process. However, it can be controlled to a thickness down to a monolayer. This requires advances in SiC substrate preparation, crucible design, and

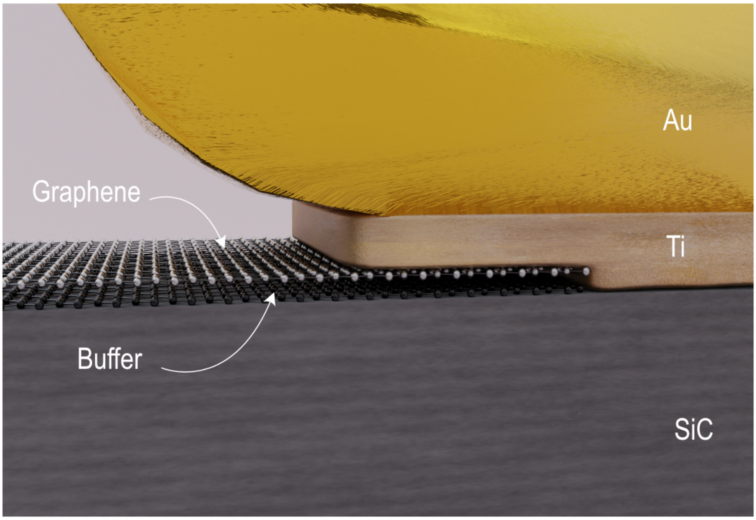

Figure 1.3: Illustration of the edge contact. Here, graphene and buffer layers are in contact with Ti metal. Au serves as a capping layer.

growth temperature/pressure control. Initially, efforts were made to grow large area single crystalline graphene so that further studies to explore its electrical properties could be performed.

Growth optimization entails the reduction of bilayer graphene inclusions (currently $< 0.1\,\%$ bilayer inclusions over 7 mm × 7 mm). For devices, much emphasis is placed on developing process techniques to fabricate low contact resistance (R_C) electrical contacts to epigraphene. Electrical contacts are of paramount importance when working with any material because they serve as the conduits through which charge carriers are injected into the material, R_C plays a crucial role in ensuring the optimal operation of the device. This thesis presents the fabrication of scalable edge contacts that results in quantum-limited contact resistance [16].

The possibility to grow single crystalline monolayer graphene over SiC wafers and low contact resistance electrical edge contacts has allowed the development of two magnetotransport-based epigraphene devices in this thesis.

- Largest functional Quantum Hall Arrays.
  Epigraphene QHAs for quantum resistance metrology utilizes both the scalability and low contact resistance of edge contacts to its benefit. Quantum Hall resistance metrology deals with the definition and precise measurement of the unit of resistance Ohm (Ω), down to part-per-billion accuracy.

- Record low noise Hall effect magnetometers.
  Hall sensors are magnetic field detection devices that work on the principle of the classical Hall effect, by measuring the Hall voltage V_H induced by an external field B. Graphene is a natural candidate for highly sensitive Hall element due to its high mobility and possibility to tune the carrier density n towards charge neutrality (Dirac point), which increases the Hall coefficient, $R_H = V_H/(IB) = (1/ne)$.

Since the technologies developed in this utilize SiC as the substrate, its wide band gap ($E_g = 3.26$ eV for the 4H polytype at 300 K) is taken into advantage to develop solar-blind UV detectors. These photodetectors work on the principle of photoelectric effect to sense light or other electromagnetic radiation. The approach involves using SiC as an absorber and graphene as a transparent contact, resulting in a peak external quantum efficiency (η) of approximately 85 % (limited by reflection losses) for wavelengths (λ) ranging from 250 to 280 nm.

1.4 Scope of the research

This thesis summarizes works presented in **Paper A** though **Paper F**.

Paper A deals with the development of scalable fabrication of edge contact to the epigraphene and two-dimensional (2D) materials. It explains the different stages of fabrication steps, two different methods to extract R_C, and the statistics involved in determining the median value of R_C.

Paper B explains one of the initial large-scale fabrications of Hall sensors using epigraphene and edge contact process. Here the performance of the Hall sensor is studied across the Dirac point, by modulating the carrier density using molecular doping technique [17]. Thermal stability of the device is also assessed for temperatures up to 150° C. Our work demonstrates that epigraphene doped close to the Dirac point could potentially outperform III-V Hall elements in the extended and military temperature ranges.

Paper C presents centimeter-sized epigraphene Metal-Semiconductor-Metal (MSM) type UV photo detector. This utilizes a large area of monocrystalline epigraphene, resulting in peak external quantum efficiency $\eta \sim 85\%$ for wavelengths $\lambda = 250 - 280$ nm, corresponding to nearly 100 % internal quantum efficiency when accounting for reflection losses.

Paper D utilizes both the scalability of graphene growth and edge contact fabrication process to fabricate epigraphene QHAs for resistance metrology. The quantization accuracy of a 236-element QHA is demonstrated to result in $R_K/236 \approx 109\ \Omega$ with 0.2 part-per-billion (nΩ/Ω) accuracy and $I_C \geq 5$ mA, (R_K the von Klitzing

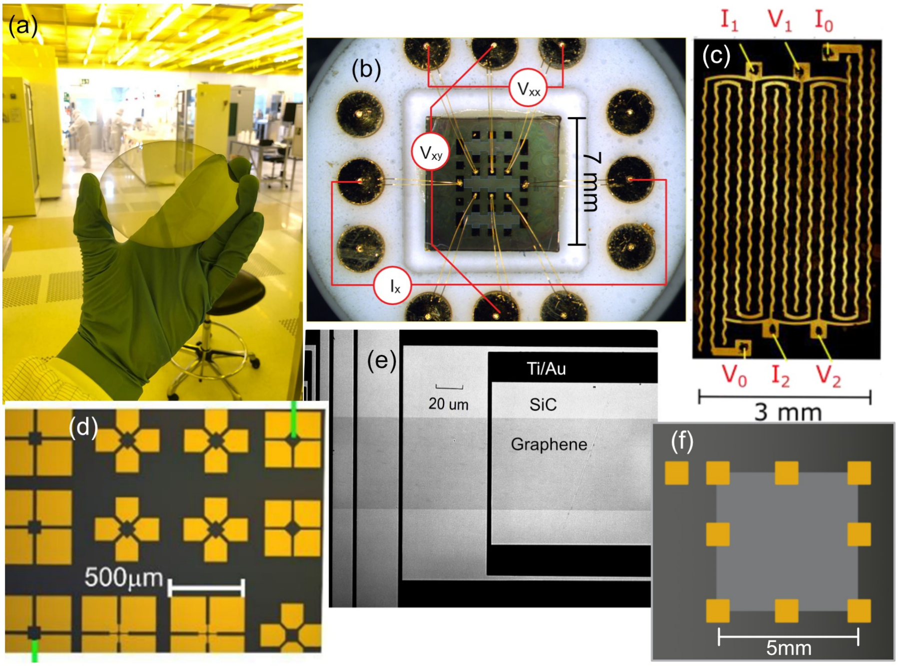

Figure 1.4: Collage of different types of devices fabricated in this thesis using epitaxially grown graphene over 4H-SiC. (a) Example of epigraphene grown on 4-inch SiC substrate. (b) Hall bars of the size ∼ 5 mm × 2 mm were used for stability analysis of molecular dopants. (c) Quantum Hall Array (QHA) consisting of 236 Hall elements, with a footprint of 3 mm × 6 mm. (d) Large area fabrication of Hall sensors. (e) Transfer length geometry fabricated to analyze the contact resistance of scalable edge contacts (f) Ultraviolet (UV) detector spanning nearly 5 mm × 5 mm area over a 7 mm × 7 mm chip. (b) to (f) Device geometry ranges from a few micrometers to several millimeters, indicating true scalability of growth as well as fabrication methods.

constant). The array accuracy, comparable to the most precise universality tests of QHE, together with the scalability and reliability of this approach, paves the road for wider use of graphene in the new SI and beyond.

Paper E investigates the long-term stability of epigraphene quantum Hall resistance standards, including single devices and an array device composed of 236 elements providing $R_K/236 \approx 109\ \Omega$. All devices utilize the established technique of chemical doping via molecular dopants to achieve homogenous doping and control over carrier density [17]. However, optimal storage conditions and the long-term stability of molecular dopants for metrological applications have not been widely studied. This paper aims to identify simple storage techniques that use readily available and cost-effective materials that provide long-term stability for devices without the need for advanced laboratory equipment.

Paper F approaches the study on graphene quality from a different perspective. Here, the low-frequency noise, also known as 1/f noise's Power Spectral Density (PSD) in epigraphene is measured using a cross-correlated spectrum analyzer. Noise PSD in Epigraphene Hall sensor devices with characteristic device length ranging from $L = 1$ µm to 1 mm is measured, resulting in a clear trend that epigraphene follows according to Hooge's empirical relation. Influence of Poly(methyl-methacrylate) (PMMA), chemical dopant 2, 3, 5, 6-Tetrafluoro-tetracyanoquinodimethan (F4TCNQ), and solid electrolyte CF_3SO_3Li over $1/f$ noise performance is also tabulated, reporting lowest ever recorded noise PSD 4.4×10^{-16} (1/Hz) at 10 Hz in a PMMA encapsulated 1 mm length Hall sensor device.

1.5 Thesis outline

The thesis is organized as follows:

- Chapter 2 explains concepts and theory related to graphene and magnetotransport in the classical and quantum limits.
- Chapter 3 describes experimental techniques used in this work. With a brief explanation to the microfabrication process utilized in this thesis. It explains tools and steps involved in magnetotransport measurement in fabricated devices.
- Chapter 4 briefs about the epitaxial graphene growth procedure and different methods used for the growth optimization process.
- Chapter 5 describes the fabrication and development of edge contacts, different methods involved in assessing the performance of these contacts, and the outcome of the edge contact fabrication process (**Paper A**).
- Chapter 6 informs about epigraphene-based Hall sensors, their linearity, thermal stability (**Paper B**), and noise performance (**Paper F**).

- Chapter 7 describes about fabrication and characterization of Quantum Hall Array Resistance standard (QHARS) (**Paper D**). It also explains investigations made for the long-term stability of epigraphene-based QHRS and QHARS (**Paper E**).
- Chapter 8 provides a summary of the main results and outlook for the topics described. Additionally, it outlines a novel avenue for research in the realm of photodetectors based on epigraphene (refer to **Paper C**) and suggests potential future investigations in this context.

CHAPTER 2

Basic concepts

Graphene is an 2D allotrope of carbon, which results from the sp^2 hybridization of carbon atoms. This chapter will start with exploring the electronic properties of graphene emerging from the honeycomb structure. Later sections will describe general magnetotransport in two dimensions.

2.1 Graphene properties

Graphene forms its honeycomb lattice, as a result of sp^2 hybridization of carbon atoms, i.e. superposition of 2s and two 2p orbitals ($\mid 2p_x\rangle$ and $\mid 2p_y\rangle$). These orbitals are oriented in $xy-$plane and have mutual 120° angle as shown in Figure 2.1 (a). Due to this, each carbon atom forms a σ bond with its three nearest neighbors, separated by $\sim 120^\circ$ giving its peculiar honeycomb structure. The remaining $2p_z$ orbital forms out-of-plane π bonds, in which the electrons are delocalized over the entire crystal.

The crystal structure of graphene is shown in Figure 2.1 (b). Taking two carbon atoms per unit cell, the Bravais lattice is triangular and has two lattice vectors

$$a_1 = \frac{a}{2}\left(3, \sqrt{3}\right), \; a_2 = \frac{a}{2}\left(3, -\sqrt{3}\right), \tag{2.1}$$

where $a \approx 1.42$ Å is the carbon-carbon distance. The triangular lattice is decomposed into unit cells comprising two identical triangular sub-lattices A and B. The nearest-neighbor vectors are

$$\delta_1 = \frac{a}{2}\left(1, \sqrt{3}\right), \; \delta_2 = \frac{a}{2}\left(1, -\sqrt{3}\right), \; \delta_3 = a\left(-1, 0\right), \tag{2.2}$$

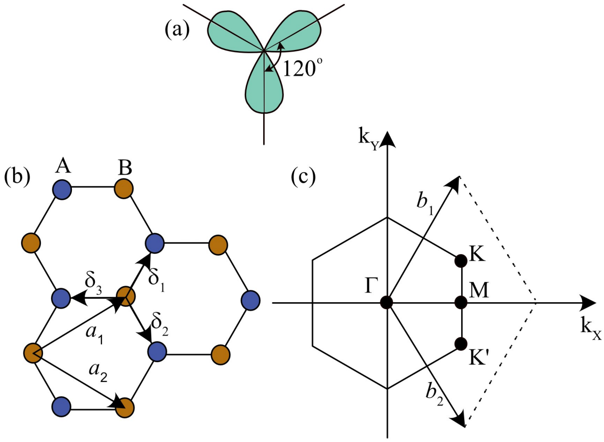

Figure 2.1: (a)Schematic view of the sp^2 hybridization. The orbitals form angles of 120°. (b) Real space representation of the graphene crystal lattice. The lattice is decomposed into two sublattices A and B per unit cell. a_1 and a_2 are the lattice vectors, δ_i, i = 1, 2, 3 are the nearest neighbor vectors. (c) Graphene in reciprocal space, with hexagonal Brillouin Zone (BZ). b_1 and b_2 are lattice vectors. K and K$'$ points are Dirac points.

The reciprocal lattice vectors b_1 and b_2 span the 1st BZ (see Figure 2.1 (c)), are

$$b_1 = \frac{2\pi}{3a}\left(1, \sqrt{3}\right), \; b_2 = \frac{2\pi}{3a}\left(1, -\sqrt{3}\right), \tag{2.3}$$

The nonequivalent points K and K$'$ are given by

$$\mathrm{K} = \left(\frac{2\pi}{3a}, \frac{2\pi}{3\sqrt{3}a}\right), \; \mathrm{K}' = \left(\frac{2\pi}{3a}, -\frac{2\pi}{3\sqrt{3}a}\right), \tag{2.4}$$

Here the electronic band structure is derived using the tight binding model. This model takes into account the interaction between nearest neighbor carbon atoms. Here, generalization is made from the unit cell to the entire solid by using the Bloch function as ansatz. The tight binding Hamiltonian is described by the 2 × 2 matrix

$$H(\boldsymbol{k}) = \begin{pmatrix} 0 & tS(\boldsymbol{k}) \\ tS^*(\boldsymbol{k}) & 0 \end{pmatrix}, \tag{2.5}$$

where $\boldsymbol{k}$ is the wave vector and the energy bands have the form [18], [19]

$$E(\boldsymbol{k}) = \pm t\,|S(\boldsymbol{k})| = \pm t\sqrt{3 \pm f(\boldsymbol{k})}, \tag{2.6}$$

where $t \approx 2.8$ eV is the nearest-neighbor hopping energy and

$$f(\boldsymbol{k}) = 2\cos(\sqrt{3}k_y a) + 4\cos\left(\frac{\sqrt{3}k_y a}{2}\right)\cos\left(\frac{3k_x a}{2}\right), \tag{2.7}$$

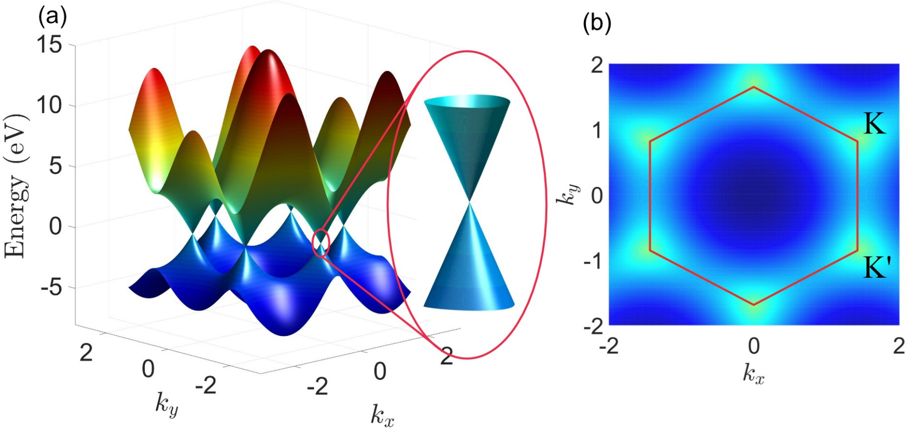

Figure 2.2: (a) Band structure of graphene calculated using the nearest neighbor tight-binding model. Inset in (a) shows a zoom-in of the energy bands around one of the Dirac points. (b) Top-down view of the band structure. At zero Fermi level, red lines are drawn to join the corners of the 1st Brillouin Zone (BZ).

At low energy, Hamiltonian 2.5 can be Taylor expanded around the two inequivalent K and K′ and they are related to sub-lattices A and B, resulting in,

$$H_{\mathrm{K,K'}}(\boldsymbol{q}) = \hbar v_F \begin{pmatrix} 0 & q_x \mp iq_y \\ q_x \pm iq_y & 0 \end{pmatrix} = \hbar v_F \boldsymbol{\sigma} \cdot \boldsymbol{q}, \tag{2.8}$$

$$E(\boldsymbol{q}) = \pm\hbar v_F\,|\boldsymbol{q}|, \tag{2.9}$$

where $\boldsymbol{q} = \boldsymbol{k} - \mathrm{K}$ and $\boldsymbol{k} - \mathrm{K}'$ is the momentum measured relatively to the Dirac points, v_F is the Fermi velocity $= \frac{1}{\hbar}\frac{\partial E}{\partial k} = \frac{3at}{2} \approx 10^6$ m/s, and $\boldsymbol{\sigma}$ represeants Pauli spin matrices:

$$\boldsymbol{\sigma_x} = \begin{pmatrix} 0 & 1 \\ 1 & 0 \end{pmatrix}, \boldsymbol{\sigma_y} = \begin{pmatrix} 0 & -i \\ i & 0 \end{pmatrix}, \boldsymbol{\sigma_z} = \begin{pmatrix} 1 & 0 \\ 0 & -1 \end{pmatrix}. \tag{2.10}$$

From 2.8 an interesting feature of the graphene energy dispersion emerges, i.e. at Dirac points K and K′, it shows the linear energy-momentum relationship, as shown in the Figure 2.2(a). This is similar to the behavior of quasi-relativistic particles at zero rest mass m_0 with the energy-momentum relation $E = \sqrt{|\boldsymbol{p^2}|\, c^2 + m_0^2 c^4} = \hbar c\,|k|$, which is identical to graphene. Indeed, the Fermi velocity v_F in graphene is about $c/300$.

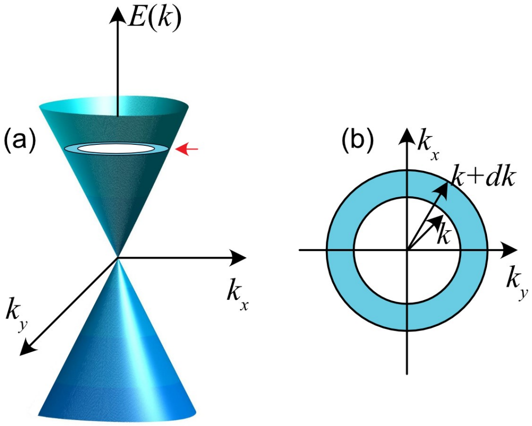

Figure 2.3: (a)Linear energy-momentum dispersion near one of the Dirac points. The red arrow indicates the cross section in k_x and k_y plane. (b) Top view of the cross-section of the dispersion relation along k_x and k_y plane. The blue circular region is the annulus covered by the radius k and infinitesimal length dk, used to calculate the number of states present in the area $2\pi k dk$.

The number of electronic states near the Dirac point in Figure 2.3(a), can be calculated as the area of the annulus from the cross-section of conical dispersion, divided by the area of one state. i.e,

$$\begin{aligned} N(k)dk &= \frac{2\pi k dk}{(2\pi/L_x)(2\pi/L_y)} \times 2 \times g_v \\ &= A g_v \frac{kdk}{\pi} \end{aligned} \tag{2.11}$$

From the equation 2.9, due to the linear dispersion relation, kdk can be written as,

$$\begin{aligned} dE/dk &= \pm\hbar v_F \\ kdk &= \frac{EdE}{(\hbar v_F)^2} \end{aligned} \tag{2.12}$$

Substituting Equation 2.12 in 2.11

$$N(k)dk = A g_v \frac{EdE}{\pi(\hbar v_F)^2} \tag{2.13}$$

From this we can calculate the Density of States (DOS) = Number of states/Area, i.e. $N(k)dk/A$,

$$DOS(E) = \frac{2\,|E|}{\pi\hbar^2 v_F^2} \tag{2.14}$$

From the Equation 2.14, DOS has a linear dependency with energy and is zero at the Dirac point. In theory, graphene should behave as an insulator at the Dirac point, because of the absence of electronic states for the fermions to occupy. In practice, in real samples at finite temperatures, there exists some residual charge carrier density due to disorder with equally probable regions spacial density fluctuations in electron-rich and hole-rich puddles [20]–[22], leading to finite measured resistance value.

From the general expression of carrier density, it is possible to derive the relation between carrier density and Fermi energy.

$$n = \int_0^\infty DOS(E) f(E) dE \tag{2.15}$$

Assuming zero temperature, where Fermi distribution $f(E)$ turns into the Heaviside step function i.e. $f(E) = 1$ for $E \leq E_F$, zero otherwise, the expression in 2.15 becomes,

$$n = \frac{E_F^2}{\pi(\hbar v_F)^2}, \text{ in other words, } E_F = \hbar v_F \sqrt{\pi n} \tag{2.16}$$

2.2 Magnetotransport characterization: Hall effect

The Drude model provides a fairly accurate depiction of electron transport, utilizing the kinetic theory of gases to explain the movement of electrons within solids. In

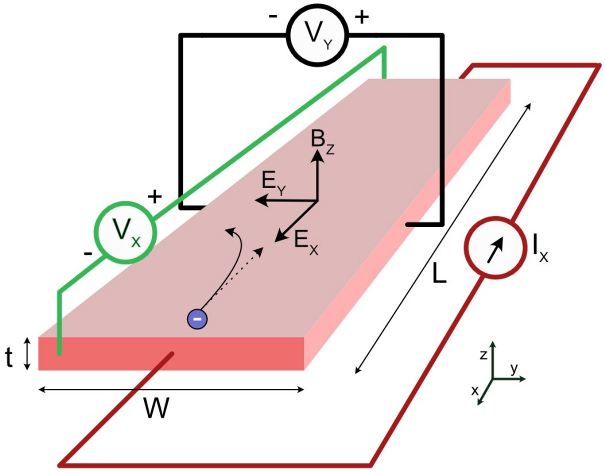

Figure 2.4: Schematic representation of a Hall bar sample geometry with width W, length L, and thickness t. As $t \to 0$, the sample is considered a 2D electron gas, graphene being one of the examples. In the presence of the magnetic field perpendicular to the plane of the sample (B_Z), charges accumulate on one side of the Hall bar and it develops an internal electric field E_Y, resulting in transverse voltage V_Y, also known as Hall voltage V_H.

this model, electrons are regarded as independent particles that react to external forces by accelerating and traversing a mean free path λ, until they dissipate their momentum upon collisions.

In the context of magnetotransport, the external forces acting on electrons are the electric and magnetic fields. Consider Figure 2.4, if the magnetic field $\boldsymbol{B}$ is applied in the direction perpendicular to the motion of the charges, the Lorentz force $\boldsymbol{F}$ acts on the moving charges perpendicular to both the magnetic field and the electric current,

$$\boldsymbol{F} = q(\boldsymbol{E} + \boldsymbol{v} \times \boldsymbol{B}) \tag{2.17}$$

By calculating the net momentum of electrons at time $t + \delta t$ one can derive the relation between current density and electric field, in the presence of the magnetic field. If $\boldsymbol{p}$ is the momentum of the electron, $\boldsymbol{p}(t + \delta t) = \boldsymbol{p}(t) + \boldsymbol{p}(\delta t)$. For a constant force $\boldsymbol{F}$ this can be written as $\boldsymbol{p}(t) + \boldsymbol{F}\delta t$. If the probability of electrons that undergo collision in time δt is $\delta t/\tau$, then the net momentum of electrons that do not undergo collision is,

$$\boldsymbol{p}(t+\delta t) = \left(1 - \frac{\delta t}{\tau}\right)(\boldsymbol{p}(t) + \boldsymbol{F}\delta t) \tag{2.18}$$

Ignoring the second-order terms for simplicity and in the limit $\delta t \to 0$,

$$\frac{\mathrm{d}\boldsymbol{p}(t)}{\mathrm{d}t} = \boldsymbol{F} - \frac{\boldsymbol{p}(t)}{\tau} \tag{2.19}$$

Substituting the forces due to electric field and magnetic field,

$$\begin{aligned} \frac{\mathrm{d}\boldsymbol{p}(t)}{\mathrm{d}t} &= q\boldsymbol{E} - e(\boldsymbol{v} \times \boldsymbol{B}) - \frac{\boldsymbol{p}(t)}{\tau} \\ m^* \frac{\mathrm{d}\boldsymbol{v}(t)}{\mathrm{d}t} &= q\boldsymbol{E} - e(\boldsymbol{v} \times \boldsymbol{B}) - m^* \frac{\boldsymbol{v}}{\tau} \end{aligned} \tag{2.20}$$

Here, m^* is the effective mass of the electron, which takes into consideration of electrostatic interactions with surrounding electrons, and lattice ions and bundles into an average effect. Under the steady state condition $\frac{\mathrm{d}\boldsymbol{v}(t)}{\mathrm{d}t} = 0$. With a perpendicular magnetic field to the x-y plane, the solutions for the 2D system are given by,

$$\begin{aligned} 0 &= -eE_X - eBv_Y - m^* \frac{v_X}{\tau} \\ 0 &= -eE_Y - eBv_X - m^* \frac{v_Y}{\tau} \end{aligned} \tag{2.21}$$

Multiplying by $\tau en/m^*$ on both sides of the Equation 2.21 and substituting current density $\boldsymbol{J} = nq\boldsymbol{v}$,

$$\begin{aligned} \sigma_0 E_X &= \omega_c \tau J_Y + J_X \\ \sigma_0 E_Y &= -\omega_c \tau J_X + J_Y \end{aligned} \tag{2.22}$$

Equation 2.22 describes the relation between electric field $\boldsymbol{E}$ and current density $\boldsymbol{J}$ in the presence of magnetic field $\boldsymbol{B}$. Without the magnetic field, this simply reduces to Ohm's law $\boldsymbol{J} = \sigma_0 \boldsymbol{E}$ and the term $\sigma_0 = ne^2\tau/m^*$ signifies the Drude conductivity. $\omega_c = eB/m^*$ is the cyclotron frequency and describes how quickly electrons complete one looped path (cyclotron orbit) due to an external magnetic field.

Equation 2.22 can be represented in the matrix form as:

$$\begin{aligned} \boldsymbol{E} = \rho \boldsymbol{J} = \begin{pmatrix} \rho_{XX} & \rho_{XY} \\ \rho_{XY} & \rho_{YY} \end{pmatrix} \boldsymbol{J} \qquad &= \sigma_0^{-1} \begin{pmatrix} 1 & \omega_c\tau \\ -\omega_c\tau & 1 \end{pmatrix} \boldsymbol{J} \\ \boldsymbol{J} = \sigma \boldsymbol{E} = \begin{pmatrix} \sigma_{XX} & \sigma_{XY} \\ \sigma_{XY} & \sigma_{YY} \end{pmatrix} \boldsymbol{E} \qquad &= \frac{\sigma_0}{1 + \omega_c^2\tau^2} \begin{pmatrix} 1 & -\omega_c\tau \\ \omega_c\tau & 1 \end{pmatrix} \boldsymbol{E} \end{aligned} \tag{2.23}$$

Here, ρ_{XX} is the geometry independent sheet resistance or resistivity ρ, which measured along longitudinal axis is $\rho_{XX} = R_{XX}W/L$, where $R_{XX} = V_X/I_X$, W

and L are width and length of the material (refer Figure 2.4). In the transverse axis $\rho_{XX} = R_{XY} = V_Y/I_X$. The conductivity tensor σ is the inverse of the resistivity tensor ρ. However, in the most general case, the individual matrix elements are not reciprocals of one another, for example, σ_{XX} may not equal to ρ_{XX}, which is the case in the presence of magnetic field.

$$\begin{aligned}\sigma_{XX} &= \frac{\rho_{XX}}{\rho_{XX}^2 + \rho_{XY}^2} \\ \sigma_{XY} &= \frac{-\rho_{XY}}{\rho_{XX}^2 + \rho_{XY}^2}\end{aligned} \tag{2.24}$$

In Figure 2.4, due to the Lorentz force trajectories of the charge carriers are altered, resulting in an excess surface electrical charge on the side of the sample. This accumulation results in the formation of an internal electric field (E_Y), which, in turn, generates an opposing electric component of the Lorentz force. At equilibrium, this electric force precisely counterbalances the magnetic force, preventing further electron deflection. In equilibrium, the resulting voltage (V_Y) is referred to as the Hall voltage. Since the charge transport is either due to electrons or holes, this effect is known as the single-band Hall effect. To derive the expression for the Hall voltage, it is essential to note that there is no longer any current in the transverse (y-direction) in equilibrium, meaning $J_Y = 0$ in Equation 2.22:

$$\begin{aligned}\sigma_0 E_Y &= -\omega_c \tau J_X \\ E_Y = -\frac{\omega_c \tau}{\sigma} J_X &= -\frac{1}{ne} J_X B\end{aligned} \tag{2.25}$$

The ratio of the induced electric field to the product of the current density and the applied magnetic field is called Hall coefficient $R_H = E_Y/(J_X B)$, resulting in,

$$R_H = -\frac{1}{ne} \tag{2.26}$$

R_H is extremely useful in characterizing the material properties. The sign of R_H reveals if the charge transport is dominated by electron or hole carriers under the fixed direction of the magnetic field. Since, $\sigma = en\mu$, one can determine carrier mobility,

$$\mu = \frac{\sigma}{en} = \frac{R_H}{\rho} \tag{2.27}$$

Equation 2.26 is a good explanation when the conduction is dominated by a single type of charge carrier. However, in materials where conduction involves contributions from both electrons and holes, (two-band Hall effect) R_H becomes [23],

$$R_H = -\frac{1}{e}\frac{n_e\mu_e^2 - n_h\mu_h^2}{e(n_e\mu_e + n_h\mu_h)^2} \tag{2.28}$$

where n_e, μ_e and n_h, μ_h denotes contributions from electrons and holes respectively. Effective carrier density n_{eff} and longitudinal sheet resistance ρ_{XX} in this case is,

$$n_{eff} = \frac{e(n_e\mu_e + n_h\mu_h)^2}{n_e\mu_e^2 - n_h\mu_h^2} \tag{2.29}$$

$$\rho_{XX} = \frac{1}{e(n_e\mu_e + n_h\mu_h)} \tag{2.30}$$

2.2.1 Integer Quantum Hall effect

For high-mobility two-dimensional systems at low temperatures and strong magnetic fields, the measured values of R_{XX} and R_{XY} deviate from the classical Drude model. Under these measurement conditions, oscillations in R_{XX} called Shubnikov-De Haas oscillations and steps in R_{XY} called Quantum Hall Effect (QHE) are observed [24]. Both of these phenomena stem from the formation of Landau Levels (LLs) in the density of states, which results from the quantization of the electron's cyclotron motion (Figure 2.5). In a semi-classical picture, Landau quantization occurs when the cyclotron orbit of the electron fits an integer number times the electron wavelength. In order for these quantum effects to be detectable in experiments, it is necessary for an electron to complete several orbits before its momentum is relaxed due to scattering. In other words,

$$\omega_c^{-1} \ll \tau \tag{2.31}$$

since, $\omega_c = eB/m^*$ and from the expression for mobility $\mu = e\tau/m^*$, Equation 2.31 can be written as $B \gg \mu^{-1}$. Approximately, quantum effects could be observed in a field of 1 Tesla, if the mobility of the sample is around 10000 $\text{cm}^2\text{V}^{-1}\text{s}^{-1}$.

At high enough magnetic fields solutions to the Schrödinger equation for free electrons reduce to a Hamiltonian almost identical to the quantum harmonic oscillator, with the position of the energy minimum, shifted from the ideal quantum harmonic oscillator on the order of $y_0 = k_x l_B^2$, where l_B is magnetic length given by:

$$l_B = \sqrt{\frac{\hbar}{eB}} \tag{2.32}$$

which represents the characteristic length scale for quantum interactions in a magnetic field and is intimately tied to the smallest possible radius of cyclotron orbits,

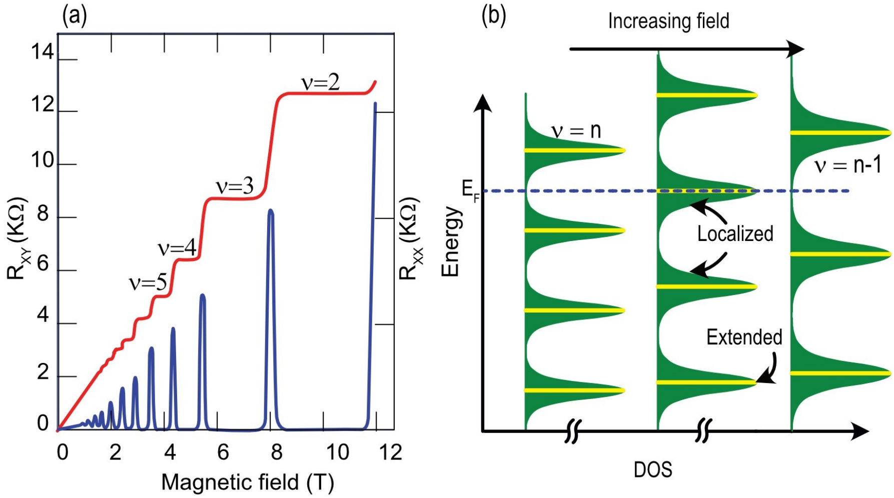

Figure 2.5: (a) Schematic representation of the transverse resistance, R_{XY}, and the longitudinal resistance, R_{XY}, evolving with varying magnetic field strength, B. At very low magnetic fields, classical Hall effects produce linear R_{XY} and constant R_{XX}. Quantization is imperfect at increasing yet lower B fields because there's still a significant energy overlap between Landau Levels (LLs). With increasing magnetic field, B, R_{XY} exhibits resistance plateaus while R_{XX} steadily decreases towards zero at each plateau. However, as B increases further, the system fully transitions into the realm of the Quantum Hall Effect (QHE), featuring precisely quantized plateaus in R_{XY} and zero resistance in R_{XX}. (b) Illustration of the Density of States (DOS) for LLs, with broadening caused by sample disorder. In this representation, the localized states are highlighted in green, while the yellow region represents the extended states. As the magnetic field strength, B, increases, the energy spacing between LLs and their degeneracy also grows. Assuming a constant Fermi energy, this leads to the progressive depopulation of more LLs as B increases. It can be envisioned that the Fermi energy effectively traverses through the LLs as B undergoes changes. The occurrence of a plateau in R_{XY} and zero resistance in R_{XX} arises when the Fermi energy resides within the localized states, positioned between two extended states. Conversely, the slope observed in R_{XY} and the peak in R_{XX} happens when the Fermi level crosses the extended states at the center of a LL.

constrained by the Heisenberg uncertainty principle. The eigenvalues are given by:

$$E_N = \hbar\omega_c \left(N + \frac{1}{2}\right), \; N \in \mathbb{N}^0 \tag{2.33}$$

they are called Landau Levels (LLs) and are being completely extended along the length of the Hall bar (x-direction), known as edge states as shown in Figure 2.6.

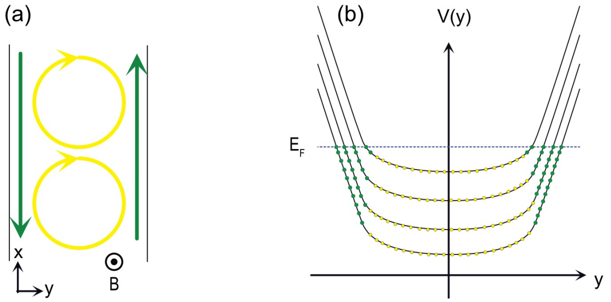

Figure 2.6: (a) Top-down view of a Hall bar with the directions of chiral edge currents (green), and localized bulk currents (yellow).(b) In the QHE regime, there is a spatial variation in the potential caused by LLs. In an ideal scenario without disorder, the potential remains uniform throughout the sample. However, it rises sharply near the edges of the sample, representing the confinement of electrons by the Hall bar. The positions of the two edge states (depicted in green) along the localized bulk states (in yellow) are determined by the drift velocity, which is related to the spatial gradient of the potential.

Since energy does not depend upon $\boldsymbol{k}$, there exists a huge degeneracy in the energy levels. If L_x and L_y are the sample length and width in x and y direction respectively (area $A = L_x \times L_y$.), in x direction there exist plain waves. This is equivalent to the particle in a box system in that direction. As a result, the x-momenta become quantised, $k_x = \frac{2\pi}{L_x}\mathbb{Z}$, the distance in x-momentum space between two eigenfunctions is therefore $\delta k_x = \frac{2\pi}{L_x}$. Because the center variable y_0 is directly linked to the x momentum $\hbar k_x$, imposes a constraint on the allowed momenta: $L_y/l_B^2 \leq k_x \leq 0$. The number of states per LL is:

$$N_L = \frac{L_x}{2\pi} \int_{-L_y/l_B^2}^{0} dk_x = \frac{eBA}{2\pi\hbar} \tag{2.34}$$

where A is the area. Number of states per unit area is $n_L = N_L/A$ is given by:

$$n_L = \frac{eB}{2\pi\hbar} = \frac{B}{\Phi_0} \tag{2.35}$$

where Φ_0 is single quantum of magnetic flux $= h/e$. For a given carrier density n, the number of filled LLs is given by the filling factor $\nu = n/n_L$. Recalling the Equation 2.23 from the Drude model for $\rho_{XY} = -\omega_c\tau/\sigma_0 = -B/ne$ and inserting $n = \nu n_L = \nu B/\Phi_0$ yields:

$$\rho_{XY} = \frac{h}{\nu e^2},\ \nu \in \mathbb{Z} \tag{2.36}$$

To experimentally observe the plateaus in R_{XY} one can either keep the magnetic field B constant and vary the charge carrier density n, or sweep the magnetic field for a fixed n. In the context of a constant carrier density, the increase in magnetic field strength leads to the expansion of energy gaps between LLs, resulting in the successive depopulation of higher LLs above Fermi level. The quantized value of resistance expressed in Equation 2.36 are in principle achieved only when exactly ν LLs are filled. However, experimental observations reveal the presence of resistance plateaus even when the Fermi energy lies between two LLs. These extended plateaus can be attributed to the broadening of LLs due to the pervasive disorder typically found in real samples. In a pristine sample, LLs are theoretically represented by delta functions, appearing as sharp spikes in the DOS, and no plateaus are evident. However, the presence of disorder broadens the LLs in terms of energy, resulting in the formation of both localized and extended states within each LL shown in Figure 2.5(b). The key distinction lies in the fact that localized states do not contribute to electrical conduction, whereas extended states do. Extended states predominantly reside near the center of the LLs, whereas localized states are positioned on either side. As the magnetic field is swept, and the Fermi energy transitions from one LL to another, the localized states are the first to be affected, either emptied or filled. However, since they do not significantly impact conduction, a constant resistance plateau is observed in magnetic field measurements.

Vanishing ρ_{XX} in QHE can be explained by the simple picture of the spatial distribution of localized and extended states. The presence of edge states becomes apparent when we consider a practical Hall bar sample, which possesses finite dimensions and boundary edges, as depicted in Figure 2.6(a). In the absence of disorder, the energy levels of LLs remain constant within the bulk region but exhibit steep rises at the edges, resembling the confining potential walls of a potential well as seen in 2.6(b). This confinement potential is responsible for the emergence of edge states. The introduction of a confinement potential modifies the eigenenergies, rendering them reliant on momentum and lifting the degeneracy of LLs. Furthermore, due to the definition of drift velocity $v_y = \frac{\partial E_N}{\partial k}$ a finite drift velocity emerges. Importantly, on opposite edges of the Hall bar, the drift velocities point in opposite y-directions. Consequently, localized edge states are established, exhibiting chiral edge currents aligned with the y-direction. These edge states are considered chiral because their flow direction is locked to the edge they propagate along, and this flow direction reverses on the opposite edge. The chirality is reversed when the magnetic field direction is reversed as well. Because the edge state travel direction is fixed, back-scattering is strongly suppressed, resulting in $\rho_{XX} = 0$ within the QHE regime.

Conversely, the bulk region, characterized by a constant potential, exhibits a drift velocity of zero and can be conceptualized as comprising localized states that effectively separate the two edge channels. It is worth noting that the overall concept of edge states remains valid even in scenarios where the bulk potential features spatial variations due to disorder, such as in real-world samples. However, this holds true only for minor variations that do not lead to the overlapping of LL energies. Additionally, the general concept remains applicable for a broad spectrum of edge confinement potentials, encompassing more realistic smooth potentials.

2.2.2 Half integer quantum Hall effect

In graphene, wave function at Dirac point K satisfying the Schrödinger equation with Hamiltonian $H_{\mathrm{K}} = \hbar v_F \sigma \cdot \boldsymbol{k}$ as in Equation 2.8 has the form:

$$\psi_{\pm,\mathrm{K}}(\boldsymbol{k}) = \frac{1}{\sqrt{2}} \begin{pmatrix} e^{-i\theta_{\boldsymbol{k}}/2} \\ \pm e^{i\theta_{\boldsymbol{k}}/2} \end{pmatrix} \tag{2.37}$$

where ± signs corresponds to the eigenenergies $E = \pm v_F k$. The wavefunction for the momentum around K$'$ with the Hamiltonian $H_{\mathrm{K}'} = \hbar v_F \sigma^* \cdot \boldsymbol{k}$ has the form:

$$\psi_{\pm,\mathrm{K}'}(\boldsymbol{k}) = \frac{1}{\sqrt{2}} \begin{pmatrix} e^{i\theta_{\boldsymbol{k}}/2} \\ \pm e^{-i\theta_{\boldsymbol{k}}/2} \end{pmatrix} \tag{2.38}$$

The wave functions are related by time-reversal symmetry at K and K$'$, which can also be seen in the Figure 2.1. i.e. if the origin of the coordinates is set at the M point of the BZ, time reversal becomes evident for the reflection along k_x axis. Also while traveling around the K and K$'$ points, Dirac fermions accumulate a phase known as Berry phase of π, which can be seen in the changes in the sign of the phase in wave functions from K → K$'$ [19].

The linear energy-momentum relation for graphene from Equation 2.9, implies zero rest mass near Dirac point. But away from the Dirac point, observed through the cyclotron motion experiments, the mass of carriers in graphene obeys [25]:

$$m_G^* = \frac{\sqrt{\pi}}{v_F}\sqrt{n} \tag{2.39}$$

with Fermi velocity $v_F \approx 10^6$ m/s. Also, the cyclotron orbit of the graphene is altered as:

$$\omega_c = \sqrt{2}\frac{v_F}{l_B} = v_F\frac{2eB}{h} \tag{2.40}$$

In a high enough magnetic field, m_G^* and Berry phase π, have a profound effect on the LL spectrum of ML graphene, which is found by solving the Dirac equation in the presence of electric and magnetic fields [19], [25], [26]:

$$E_N = \pm\hbar\omega_c\sqrt{N} = v_F\sqrt{2\hbar eBN},\ N = 0, 1, 2... \tag{2.41}$$

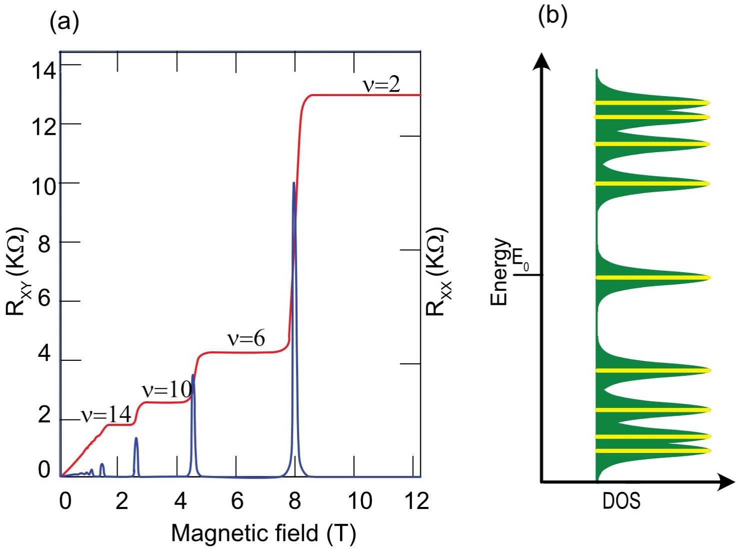

Figure 2.7: (a) Schematic representation of the transverse resistance R_{XY} and longitudinal resistance R_{XX} for graphene in QHE regime. Quantized resistance R_{XY} has filling factors $\nu = 2$, 6, 10, 14... compared to conventional 2D electron gas, where $\nu = 1$, 2, 3, 4... (b) Schematic representation of the LL energy spectrum for graphene, showing large energy spacing between 1st and 0th LL.

The energy spacing between LLs deviates from being equidistant and follows a scaling law $\delta E \propto \sqrt{B}$. Additionally, each LL in graphene experiences a twofold degeneracy due to valley degeneracy at K and K$'$. Moreover, a new LL emerges at zero energy, shared by both valleys, and thus possesses only spin degeneracy. Consequently, these variations in LL properties have an impact on the resistance plateaus observed in R_{XY} as seen in Figure 2.7(a). As per the Equation 2.35, in conventional 2D systems degeneracy per LL is given by B/Φ_0. But in graphene inclusion of spin and valley degeneracy, each LL will have $4B/\Phi_0$ fermions, with an exception at zero energy LL, which is $2B/\Phi_0$.

To determine the charge carrier density in graphene, one must sum the electrons from N fully filled LLs located above the zero energy level, resulting in:

$$n = N\frac{4eB}{\hbar} + \frac{2eB}{\hbar} = \frac{4eB}{\hbar},\ N = 0, 1, 2... \tag{2.42}$$

substituting above equation in the Equation 2.23 for the conventional Hall effect, results in:

$$\rho_{XY} = \frac{B}{eN} = \frac{h}{4e^2(N + 1/2)},\ N = 0, 1, 2... \tag{2.43}$$

Due to this graphene has the quantized values of ρ_{XY} at half-integer multiples of $h/4e^2$. Written in terms of quantized resistance of $h/\nu e^2$, graphene has filling factor of $\nu = 2,\ 6,\ 10,\ 14...$ This feature in magnetoresistance measurement will also work as a fingerprint in identifying ML graphene from multiple layers.

CHAPTER 3

Experimental techniques for electrical characterization

This chapter explains microfabrication procedures, passivation techniques, and approaches for modulating carrier density in devices utilizing epigraphene. Additionally, it will explore the electrical characterization of epigraphene-based devices to assess their functionality and transport characteristics. This evaluation involves employing various methodologies like van der Pauw (vdP) measurements, the transfer length method, Hall effect measurements, and quantum Hall measurements.

3.1 Devices

To perform electrical characterization, it is crucial that the epigraphene is appropriately shaped into the respective device under test. Within this thesis, the epigraphene is formed into Hall bars, Hall sensors, Hall arrays, and photodetectors. This segment will outline the microfabrication process and the methods utilized to regulate the charge carriers in the creation of these devices.

3.1.1 Microfabrication

In this fabrication, contact deposition and defining the device geometry is achieved by two Electron Beam Lithography (EBL) steps. A comprehensive account of the procedures can be found in Part II. Recipe C. The primary approach utilizes EBL to imprint device patterns onto epigraphene.

- **Step 1 - Contacts and markers:** The fabrication process begins by spin coating the surface of the epigraphene with three layers of resists (Figure. 3.1(a)). The first is a layer of Poly(methyl-methacrylate) (PMMA), followed by PMMA based copolymer, and lastly A-RP 6200.13. The key to ensuring scalable and reproducible contacts is to form a narrow-wide-narrow opening in the resist, which is achieved in a single e-beam exposure and single development step by using a resist with higher sensitivity (compared to the top and bottom layers) as the middle layer. Following the resist development, dry etching is employed to eliminate the 2D material, exposing its edges for a subsequent metallization procedure and metal liftoff.
- **Step 2 - Shaping the device:** The second EBL process is used to define the device geometry. Here, a layer of PMMA is spun over the sample, followed by the EBL exposure. Following the development dry etching in O_2 plasma is performed to shape the device as well as isolate multiple devices from one another as shown in Figure 3.1(b).

Utilizing the tri-layer resist method, as opposed to a single-layer approach, produces remarkably high yields in contact fabrication and ensures consistent achievement of low contact resistance. This is because the resist profile provides a clean liftoff when the metal deposition is performed by thermal evaporation and also by sputtering, thus giving additional flexibility when designing a microfabrication process.

3.1.2 Passivation and doping the devices

After the fabrication of the device using epigraphene, the absence of any encapsulation renders the device vulnerable to environmental impacts, leading to instability in measured sheet resistance, carrier density, mobility, etc. Consequently, it becomes important to shield the device from ambient influences. To achieve this, a layer of PMMA is applied to the sample via the spin coating process. This will result in n doped epigraphene with carrier density $\approx 7 \times 10^{12}$ /cm^2. Regulating the charge carrier density in epigraphene remains a prominent challenge within the research domain. We have fixed this problem by the utilization of a chemical doping approach employing a blend of 2, 3, 5, 6-Tetrafluoro-tetracyanoquinodimethan (F4TCNQ) molecules and the polymer PMMA [27].

The initial phase involves the preparation of the dopant blend, with specific instructions and mixing proportions provided in Part II. Recipe D. The F4TCNQ dry powder is dissolved anisole solvent, and the resulting solution is mixed with the PMMA resist. In this thesis, the standard dopant blend comprises 7 wt.% F4TCNQ

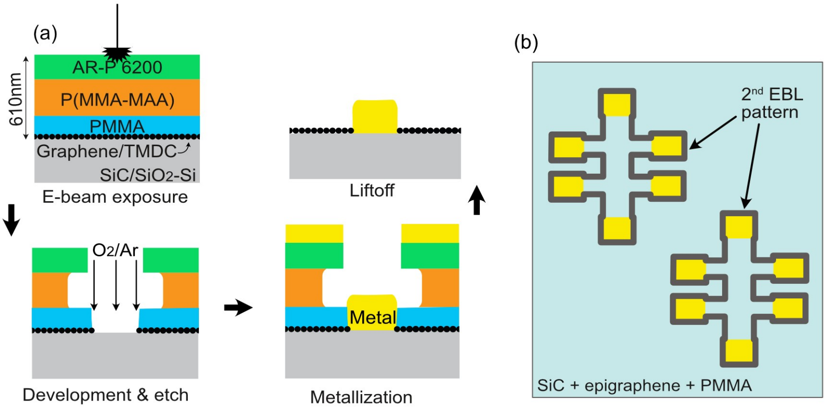

Figure 3.1: Formation of scalable edge contacts to 2D materials. (a) Schematic representation of the tri-layer resist method for fabrication of edge contacts to 2D materials. Three layers of resists are spun over epigraphene sample. After the Electron Beam Lithography (EBL) exposure and development, graphene is removed using O_2 plasma. Metallization is done either by physical vapor deposition or sputter deposition. Lastly, the remaining resist and metal layers are removed using a lift-off process. (b) A layer of Poly(methyl-methacrylate) (PMMA) is spun over the sample and a 2^{nd} EBL process to shape and isolate the devices from one another is performed.

molecules within the PMMA matrix. Before the dopant blend is applied onto the epigraphene, a layer of pure PMMA or copolymer PMMA is spin-coated, functioning as a spacer layer that regulates the diffusion of F4TCNQ dopants.

Following this, the dopant blend is spin-coated directly onto the spacer layer. Subsequently, the resist is subjected to annealing at temperatures exceeding the glass transition temperature of PMMA, typically at 160 °C. Although this step is typical for the EBL process to eliminate residual solvent from the resist, the primary aim here is to exploit the annealing process to fine-tune the final charge carrier density of doped epigraphene. Continuous thermal annealing at these temperatures leads to an irreversible reduction in the doping impact of F4TCNQ molecules, resulting in increased n-doping of epigraphene with prolonged annealing duration. Notably, employing the standard dopant blend, the samples can be either p-doped or n-doped, contingent on the annealing duration.

The optimal annealing duration for achieving charge-neutral graphene is approximately 5 minutes for samples coated with a spacer layer and a dopant layer on top. For enhanced doping stability, additional polymer layers can be incorporated, such as PMMA-dopant-PMMA-dopant-PMMA. Annealing for 5 minutes at 160 °C follows each addition of the polymer layer. To attain charge neutrality, an additional 10-15 minutes of annealing is necessary.

3.2 Electrical characterization

This section explores different direct current (DC) characterization techniques used to assess the quality of grown graphene, the characteristics of fabricated devices and examine the homogeneity of molecular doping. Through DC measurements, it is possible to characterize the device in terms of its charge carrier density, mobility, and sheet resistance. Additionally, these techniques enable the investigation of any deviations in the electrical behavior across different regions of the epigraphene samples, thereby providing insights into the uniformity and consistency of the material's properties. This helps in understanding the reliability and reproducibility of the fabricated devices, ensuring that the epigraphene-based technology meets the necessary standards for further development and potential commercialization.

In this thesis, epigraphene is shaped into Hall bars and van der Pauw geometry for characterization. To conduct Hall measurements at room temperature and higher, a custom setup was built, depicted in Figure 3.2. This setup utilizes a basic electromagnet to generate a magnetic field of up to 35 mT, which proves adequate for characterizing the device's properties. For elevated temperature measurements, the sample is fixed on a specially designed printed circuit board. This board features a copper sample holder equipped with a ceramic heater capable of reaching temperatures of up to 400° C.

To observe quantum transport phenomena like Quantum Hall Effect (QHE), it is necessary to cool the samples to low temperatures and subject them to a perpendicular magnetic field. The cooling process involves placing the sample inside a helium gas-flow cryostat, utilizing liquid helium (4He). By pumping on the helium in an enclosed sample volume, the temperature can be brought down to slightly below $T = 2$ K. Additionally, the cryostat is equipped with a superconducting magnet capable of generating high magnetic fields, reaching up to 9 T (Blue Oxford) or 14 T (Quantum Design PPMS).

3.2.1 Magnetotransport: Hall bars

Magnetotransport measurements play a crucial role in extracting key information, such as carrier density and carrier mobility. The standard procedure for conducting measurements involves applying a current bias to the sample and measuring the voltage in a four-probe configuration, utilizing equipment such as the Keithley 6221 DC and AC current source, as well as the Agilent 34420A nanovoltmeter. The

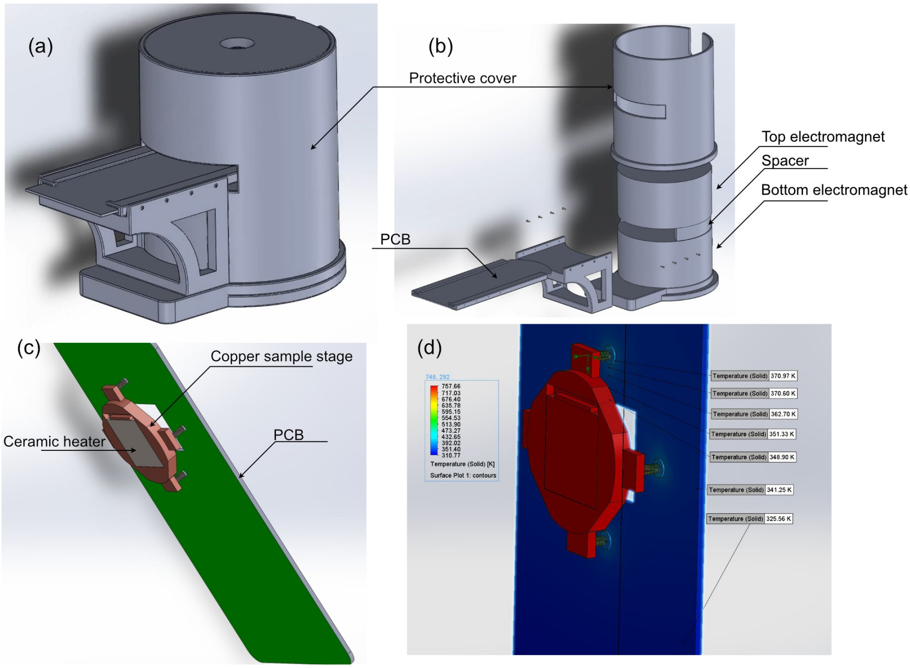

Figure 3.2: (a) 3D-model of room temperature Hall measurement setup. (b) Exploded view of the setup showing placement of electromagnets. (c) Design of the Printed Circuit Board (PCB) with attached copper sample stage. A ceramic heater is mounted on the backside of the stage to perform Hall measurements at elevated temperatures as high as 400° C. (d) Simulation of the temperature gradient between sample stage and PCB when the heater is set to 400° C

specific current level employed depends on the doping level of the epigraphene. For lightly doped samples, the current typically falls within the range of 100 nA. This helps prevent overheating. In contrast, for more heavily doped samples, the current may be one or two orders of magnitude higher. The crucial factor is that the current-voltage (IV) characteristics remain linear within the selected current range, both at room temperature and down to cryogenic temperatures. The Hall coefficient can then be extracted through a linear fit to the measured transverse Hall resistance R_{XY} for magnetic fields $|B| < 1$ T and subsequently, the carrier density and carrier mobility can be determined. However, it is practically feasible to observe the QHE only at cryogenic temperatures and $|B| > 1$ T. The maximum achievable temperature depends on the available magnetic fields and the doping level of the epigraphene. In

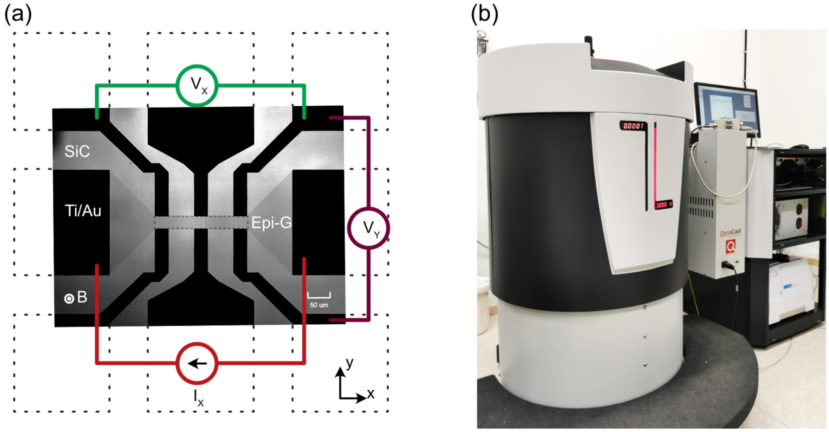

Figure 3.3: (a) Transmission mode optical microscope image of epigraphene Hall bar. Since epigraphene absorbs 1.3 % of light, it is seen as a darker shade of grey compared to SiC. The Ti/Au contacts completely block the light, hence seen in pitch black. This device is current biased in x direction (I_x) and subject to an out-of-plane perpendicular magnetic field B, and the longitudinal voltage V_X and transverse voltage V_Y are measured. (b) Quantum Design PPMS® DynaCool™ measurement system used for low-temperature measurements.

a high-quality optimally doped sample it is possible to observe QHE, i.e. $R_{XX} = V_X/I_X = 0$ and $R_{XY} = V_Y/I_X = h/\nu e^2$ at magnetic fields $|B| \approx 1$ T.

3.2.2 Magnetotransport: Van der Pauw

Over six decades ago, van der Pauw introduced a theorem for determining the electrical resistivity and sheet resistance of conducting materials, regardless of their shape, through a specific procedure [28]–[30]. The fundamental concept involves employing a combination of measurements conducted with four contact pads arranged in various configurations around the perimeter of the sample as shown in Figure 3.4. This method allows for the determination of the Hall coefficient and sheet resistance of a device, regardless of its specific geometry. Ideally, the sample should exhibit a flat, uniform thickness that is significantly thinner than its width and length. Additionally, the sample should be devoid of any perforations, displaying homogeneity and isotropy. The electrical contacts should be ohmic, attached to the edges of the chip, with their contact areas significantly smaller than the sample's total area. This technique is widely used as a 4-point measurement for determining the sheet resistance and the Hall coefficient of materials.

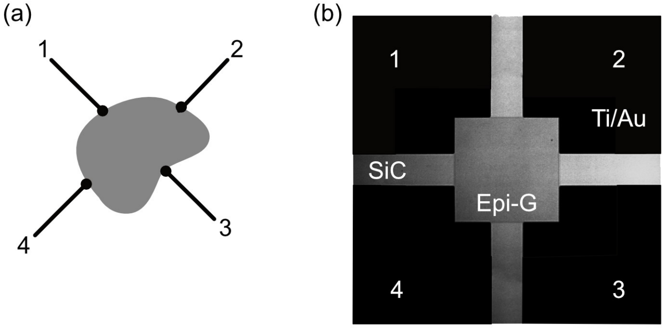

Figure 3.4: (a) Schematic representation of a generic van der Pauw (vdP) device with numbered contacts. (b) Transmission mode optical microscopy image of an epigraphene device in vdP geometry with numbered contacts corresponding to the numbers in (a)

In practice, real samples may exhibit deviations from this ideal scenario, resulting in certain inaccuracies in the vdP measurement method. Nevertheless, a meticulously designed epigraphene device with uniform doping levels tends to align closely with the ideal conditions. To assess this, one can perform a comparison between the sheet resistance and carrier density derived from vdP measurements and those obtained through QHE measurements. Figure 3.4(b) shows an example of an epigraphene device fabricated in vdP geometry. To determine resistivity (ρ), two resistances must be measured—one along the horizontal direction (R_A) and another along the vertical edge (R_B). For instance, if the current is initially directed through the horizontal edge using contacts 1-2, and voltage is measured between 4-3, the resistance is calculated as $R_{12,43} = \frac{V_{43}}{I_{12}}$. This procedure is repeated with reversed polarity to account for offsets like thermal voltages. Subsequently, in the reciprocal horizontal case, $R_{43,12}$ is measured, followed by switching to the vertical edge and repeating the process. In total, eight measurements are conducted, resulting in:

$$\begin{aligned} R_A &= \frac{R_{12,43} + R_{21,34} + R_{34,21} + R_{43,12}}{4} \\ R_B &= \frac{R_{14,23} + R_{41,32} + R_{32,41} + R_{23,14}}{4} \end{aligned} \tag{3.1}$$

The sheet resistance ρ is then determined by numerically solving the vdP equation:

$$e^{-\frac{\pi R_A}{\rho}} + e^{-\frac{\pi R_B}{\rho}} = 1 \tag{3.2}$$

For the Hall voltage, a perpendicular magnetic field $+B$ is applied with respect to the sample plane, and measurement can be done by sending current between contacts 1-3, and measuring the voltage between 2-4, denoted as V^{+}_{2-4}. By alternating between different configurations of contacts and switching the direction of the perpendicular magnetic field, a total of eight measurements yield Hall voltage (V_H):

$$V_H = \frac{V^{+}_{2-4} - V^{-}_{2-4} + V^{+}_{4-2} - V^{-}_{4-2} + V^{+}_{1-3} - V^{-}_{1-3} + V^{+}_{3-1} - V^{-}_{3-1}}{8} \tag{3.3}$$

One can calculate the Hall coefficient $R_H = V_H/IB$, determine the carrier density as $n = 1/eR_H$, and find the carrier mobility as $\mu = R_H/\rho$.

3.2.3 Contact resistance

The standard way of measuring contact resistance is by Transfer Length Method (TLM) [31]. Figure 3.5(a) shows a schematic of the TLM structure, fabricated over a graphene strip of width W and length L. The TLM contacts are separated by a varying length from $D1$ to $D5$. Measured two-terminal resistance R_{2T} is give by:

$$R_{2T} = 2R_m + 2R_C + R_{channel} \tag{3.4}$$

which involves considering the (known) contribution from the metallic leads (R_m), the metal-graphene interface (R_C), and the graphene channel resistance $R_{\text{channel}} = \frac{\rho L}{W}$, where ρ is graphene's resistivity. When plotting the measured R_{2T} against the contact spacing, ideally, the result is a linear relationship as shown in 3.4(b). The resistivity of the material can then be determined from the slope, expressed as $\frac{dR_{2T}}{dL} = \frac{\rho}{W}$, while the contact resistance can be derived from the intercept at $L = 0$, represented as $R_{2T}(L = 0) = 2R_m + 2R_C$.

Since graphene can be quantized, this phenomenon can also be used to accurately quantify the contact resistance. In the Hall bar geometry, using three-terminal measurement R_{3T} as shown in Figure 3.5(b). The current is sent between contacts 1-3. The voltage is then measured between 1-2, where 2 is an intermediate voltage probe. The total resistance measured is:

$$R_{3T} = 2R_m + R_C + R_{channel} \tag{3.5}$$

At low temperatures and in a quantizing magnetic field, the graphene channel resistance vanishes, $R_{channel} = 0$, the edge state which travels from 1 to 3, passing by 2, is an equipotential line, and thus all of the potential drops occurs due to contact resistance of contact 1 alone. This gives a direct measurement of the metal-graphene

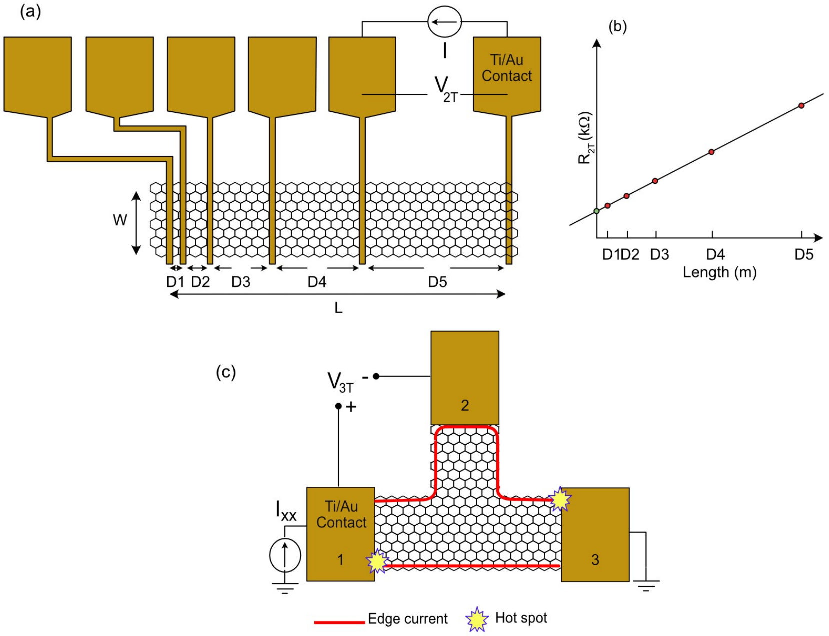

Figure 3.5: (a) Schematic of transfer length method of contact resistance measurement, in this case for graphene shown in a hexagonal pattern in black. (b) Illustration of Transfer Length Method (TLM) measurement, where 2 terminal resistances measured (y-axis) between contact pairs of reducing channel length $D5$ to $D1$ (x-axis) is depicted. (c) Illustrating three-terminal contact measurement on a Hall bar. Under the quantum Hall regime, the channel resistance diminishes owing to the development of edge states. The measured three-terminal resistance, $R_{3T} = V_{3T}/I_{xx}$, incorporates R_C and the recognized resistance of the leads $2R_m$.

interface resistance R_C at contact 1 [32], [33]. This configuration is repeated for all the other contacts of a Hall bar to individually measure its respective contact resistance.

CHAPTER 4

Optimization of epitaxial growth of graphene on SiC

This chapter outlines the process of growing epigraphene on SiC substrates. The initial section covers the material properties of SiC, followed by an explanation of the graphene epitaxial growth mechanism over SiC. The following sections elaborate on the optimization techniques used in this study to improve the quality of epigraphene.

4.1 Silicon carbide

Silicon carbide (SiC), is a group IV-IV compound in which each silicon atom in the crystal is mostly covalently bonded (89 % covalent and 11 % ionic) to four carbon atoms and vice versa in a tetrahedral arrangement as shown in Figure 4.1. The strong bonding strength (4.53 eV) and short bond length (1.89 Å) between Si-C atoms provide SiC with its hardness and strength. The basal plane consists of three silicon atoms and the next plane of silicon atoms is separated by 0.252 nm. The plane containing the carbon atom in the tetrahedral interstitial space is 0.063 nm from the basal plane. While there are over 200 known polytypes of SiC [34], only a few are commonly grown in a reproducible form acceptable for use as an electronic semiconductor. The close-packed structures of these hexagonal polytypes can simply be described by four Miller-Bravais indexes noted (h, k, i, l) which are referred to the four axes (a_1, a_2, a_3, c) shown in Figure 4.1(b). Hexagonal polytypes 4H-SiC and 6H-SiC are most commonly used for epitaxial growth of graphene.

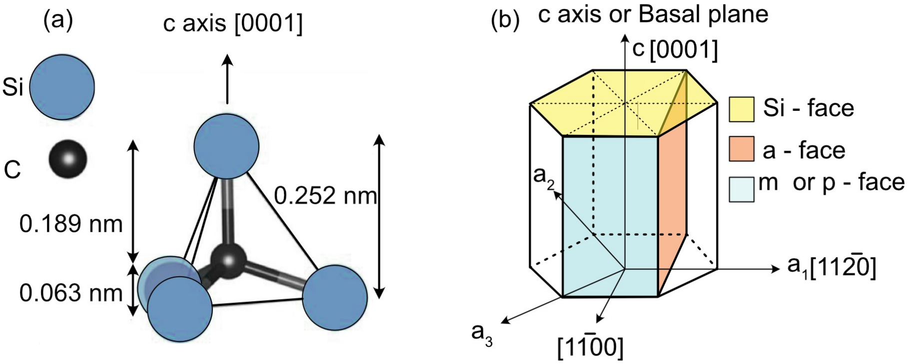

Figure 4.1: (a) Tetrahedral basic unit of SiC. (b) The hexagonal unit cell of SiC shows different crystal planes.

Each SiC polytype consists of 50 % C atoms and 50 % Si atoms, but they have distinct sets of physical and electrical properties based on the stacking order and rotation in the SiC crystal. There are two basic configuration arises from the stacking order of successive basic tetrahedral unit, which is either hexagonal (ABAB stacking) or cubic (ABC stacking) as shown in Figure 4.2. In Figure 4.2(a) and (b), the silicon atoms designated as "h" or "k" represent Si-C bilayers residing in quasi-hexagonal or quasi-cubic surroundings with respect to their immediately neighboring layers [35]. In both 4H-SiC and 6H-SiC, the first number represents the number of Si-C bilayers in the unit cell and the letter H indicates that the crystal symmetry is hexagonal. In 4H-SiC there is an even distribution of cubic and hexagonal bonds, forming a stacking sequence of ABCB. On the other hand, in 6H-SiC, approximately two-thirds of the bonds are cubic, and the remaining one-third are hexagonal, resulting in a stacking sequence of ABCACB. Despite the presence of cubic bonds in both polytypes, the overall crystal symmetry remains hexagonal.

4.2 Epitaxial graphene on silicon carbide

Epitaxial growth of monolayer (ML) graphite (graphene) on crystalline hexagonal SiC was first demonstrated in 1975 by Van Bommel et al [36]. At elevated temperatures under ultrahigh vacuum (UHV: $< 10^{-10}$ Torr), ML domains of carbon consistent with the structure of graphene were obtained, as determined by Low-Energy Electron Diffraction (LEED) and Auger electron spectroscopy. Subsequently, numerous individuals have made contributions towards refining the growth techniques,

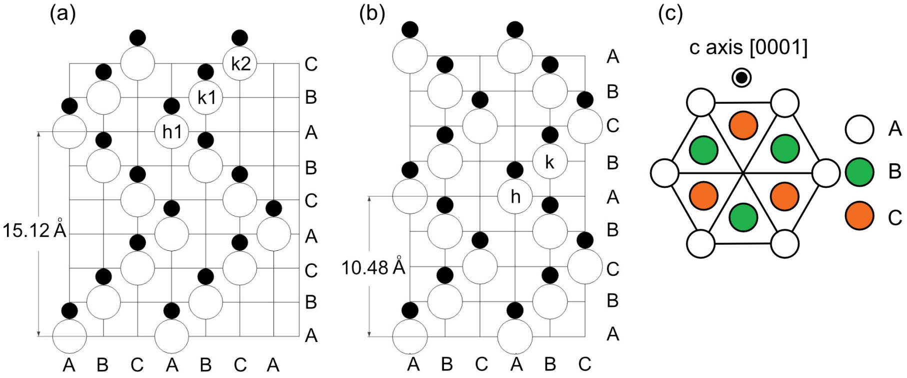

Figure 4.2: A 2D schematic representation of the crystal structure of (a) 6H-SiC and (b) 4H-SiC [35]. Si atoms are depicted as white circles, and C atoms are represented by black-filled circles. In the case of 6H-SiC, the designation "h1" is used for atom sites featuring hexagonal bonds, while "k1" and "k2" are sites with two distinct cubic bonds. Consequently, 6H-SiC comprises one-third of hexagonal bonds, with the remainder being cubic, all while maintaining an overall hexagonal crystal structure. In contrast, for 4H-SiC, the notation "h" denotes hexagonal bonds, and "k" signifies cubic bonds. In 4H-SiC, hexagonal and cubic bonds are present in equal proportions. (c) Shows ABC sites in the hexagonal crystal lattice in 4H-SiC.

focusing on enhancing the quality of SiC substrates and optimizing growth parameters [37]–[41]. SiC, characterized as a polar material, possesses two dissimilar terminations: the Si-terminated face, aligned with the (0001) polar surface, and the C-terminated face, corresponding to $(000\bar{1})$. In both the Si face and C face, the growth mechanism of graphene layers is governed by a common physical process: the sublimation of Si at elevated temperatures, occurring at a significantly faster rate than that of C due to its higher vapor pressure [42]. Due to this high quality single crystalline ML graphene is commonly grown on the Si-face because it offers a slower and more regulated growth process [37]. In contrast, growth on the C-face often yields multi-layered and irregularly distributed graphene patches [39]. Consequently, the Si-face is exclusively favored for applications requiring high-quality ML graphene.

During graphene growth, the initial carbon layer formed is insulating because approximately 30 % of the carbon atoms create covalent bonds with the SiC substrate, disrupting the π bonds. This layer is commonly referred to as the buffer layer. The second layer formation on top of the buffer is the actual conducting ML of graphene.

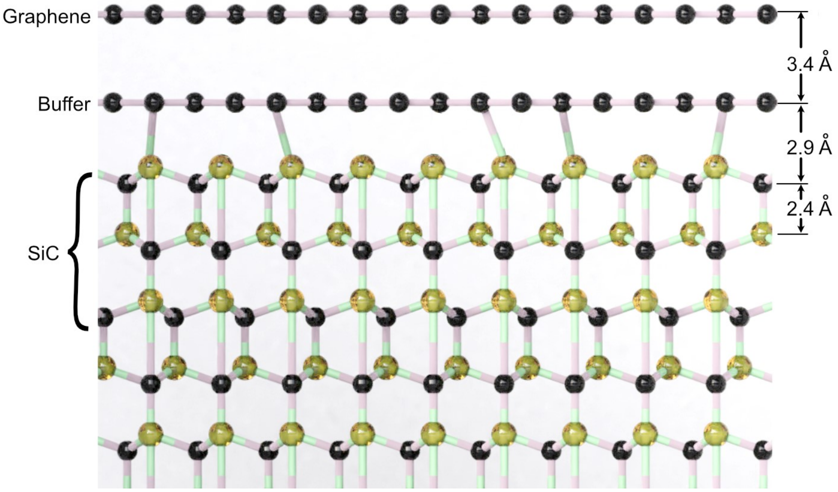

Figure 4.3: Schematic representation of the cross-section of ML epigraphene, buffer layer grown on SiC (not to scale). The buffer layer interacts with the SiC substrate through covalent bonds, hence is insulating.

Without the need for an external carbon source, the growth dynamics of the process can be influenced by adjusting temperature, pressure, and annealing duration. However, it is important to note that these parameters do not act independently of the different processes occurring. Lower temperatures might offer better control over the growth rate, but they can also lead to incomplete graphitization areas left as insulating domains of the buffer layer. Higher temperatures might help in faster sublimation resulting in covering the entire Si face with graphene, but a higher sublimation rate will lead to the formation of bilayer (BL) domains. This interplay of variables adds complexity to the process.

Experimental techniques like scanning tunneling microscopy (STM) and Low-Energy Electron Diffraction (LEED) have helped researchers to understand the orientation of the buffer in relation to SiC crystal. These analyses reveal the formation of buffer with 30° rotation with respect to SiC, and it makes a large superstructure $6\sqrt{3} \times 6\sqrt{3}$ reconstruction [43], [44]. Figure 4.4(a) shows the SiC crystal with Si face facing up. Buffer layer grows on top of SiC, such that the armchair edge of the buffer makes an angle of 30° concerning <1000> direction of SiC [45], [46] as shown in Figure 4.4(b). Buffer, graphene and subsequent epigraphene layers commonly obey Bernal stacking (AB) shown in Figure 4.4(c).

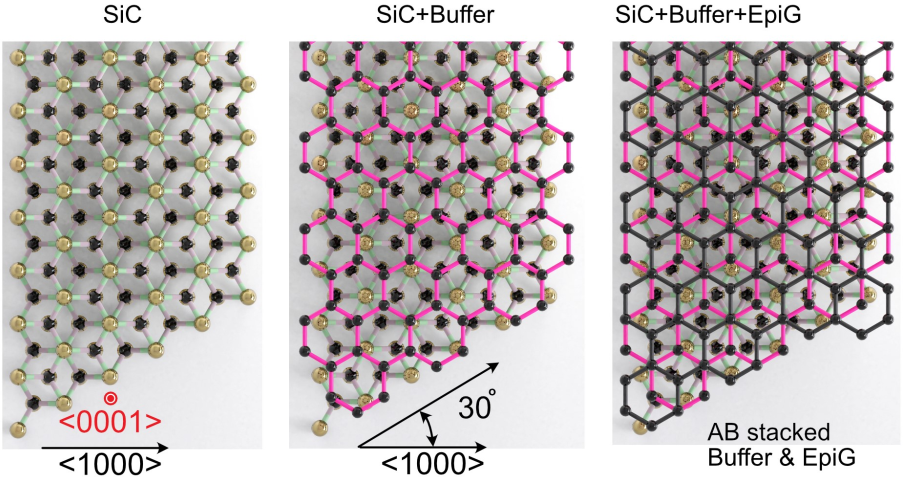

Figure 4.4: Schematic of crystal orientation of buffer and epitaxial graphene with respect to SiC crystal. (a) Top view of the Si face of SiC crystal, Si atoms are represented in gold color and carbon in black. (b) Orientation of buffer (with pink interatomic bonds) on top of SiC. The armchair edge of the buffer makes an angle of 30° concerning <1000> axis of SiC. (c) Bernal (AB) stacking between buffer and epitaxial graphene on top of buffer (with black interatomic bonds).

Due to their proximity (~ 3Å), the buffer layer influences the electrical properties of graphene. The high density of charges in the buffer layer acts as a donor, leading to significant intrinsic n-doping of epigraphene, typically in the range of $n \approx 10^{13}$ cm^{-2}. Additionally, the high density of states acts like charge traps and effectively pins the Fermi level of epigraphene, reducing the gate efficiency when attempting to modulate the charge carrier density [47]. This reduction can substantially decrease the gate capacitance by more than 90 %. Furthermore, the silicon carbide substrate contributes to these effects due to dangling bonds on its surface [48]. In practical applications of the Quantum Hall Effect (QHE), it is desirable to mitigate the influence of the buffer layer to bring epigraphene closer to charge neutrality, making QHE observable at low magnetic fields (< 5 T, 4 K) [49]. Although the charge transfer between graphene and the buffer layer complicates achieving charge neutrality in epigraphene, it has a beneficial side effect on the robustness of the quantum Hall plateau. This charge transfer process results in a magnetic field-dependent charge carrier density, significantly extending the $R_{XY} = h/2e^2$plateau. Experimental observations have demonstrated the plateau's persistence up to 50 T [50].

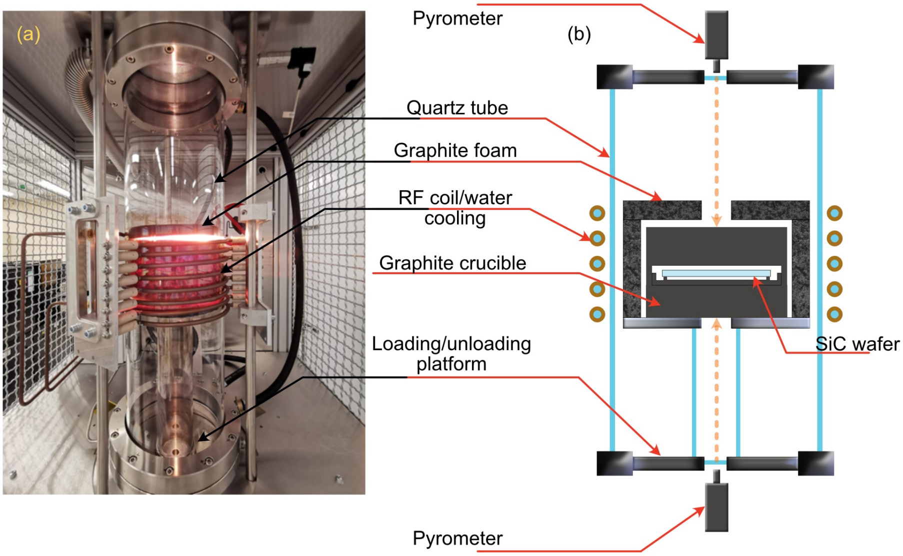

Figure 4.5: (a) Photograph of the furnace used for the epitaxial growth of graphene over SiC wafer. The red glow emanating out of the graphite foam is from the graphite crucible placed inside the foam, heated to ≈ 1800 °C in an argon atmosphere of around 850 mbar during the growth process. (b) Schematic of the cross-section of the furnace. It shows graphite foam housing a graphite crucible. Inside the crucible resides SiC wafer, with Si face facing down mounted over the sample stage specially designed to control the distance between Si face and the crucible's inner floor, which plays a crucial role in controlling Si sublimation.

4.3 Growth and optimization of epigraphene

The first step of growth starts with acquiring the high purity semi-insulating (HPSI) SiC wafer with surface orientation (0001) ± 0.25°. Graphene can be either grown on the entire wafer or wafers are diced into 7 mm × 7 mm square chips. Wafer/chips are then cleaned by using RCA cleaning procedure, as explained in Part II. Recipe A.

Figure 4.5(a) shows the photograph of the induction oven used to grow the epitaxial graphene. In the heart of the furnace, is a solid graphite crucible. The selection of the crucible size depends upon the dimensions of the SiC substrate utilized for the growth process. A 4-inch crucible is employed for the 4-inch wafer, while a 2-inch crucible is utilized for the 7 mm × 7 mm chip. The graphite crucible is heated

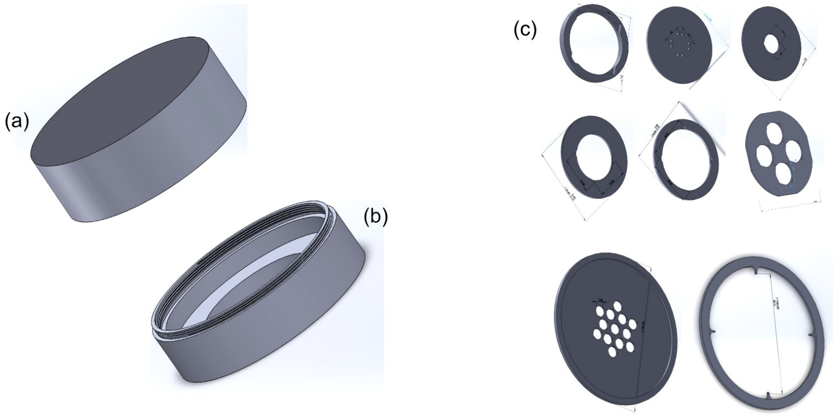

Figure 4.6: (a) 3D model of the 4-inch crucible designed using SolidWorks. (b) 3D model of different types of sample stages for chips of different sizes as well as for 4-inch wafer.

via induced eddy currents generated by the application of radio frequency power through the coil wound around the quartz tube. The entire quartz chamber is filled with an inert argon atmosphere maintained at approximately 850 mbar. The furnace undergoes a gradual heating process, taking roughly 1 hour to reach the desired temperature set-point, where it is held for a duration of 5 minutes (refer Part II. Recipe B for detailed growth procedure).

The crucible and sample stages on which the SiC substrate resides during the growth process influence the growth quality significantly. Several models of the crucible are designed and tested over a period of two years for growth optimization. Figure 4.6(a) and (b) shows one of the 3D models of the top and bottom parts of the crucible used during the optimization process. Figure 4.6(c) shows different types of sample stages used inside these crucibles for optimization purposes. After the epitaxial growth, the quality and surface coverage of the ML graphene can be swiftly assessed through the non-invasive methods detailed below.

Fast quality control by optical microscopy

SiC substrate and epigraphene appear completely transparent to the naked eye. However, utilizing optical microscopy techniques operating in the visible spectrum can still gain valuable insights into the sample's uniformity following growth [51]. One such technique involves transmission mode microscopy, combined with digital contrast enhancement, to distinguish between single and multi-layer graphene

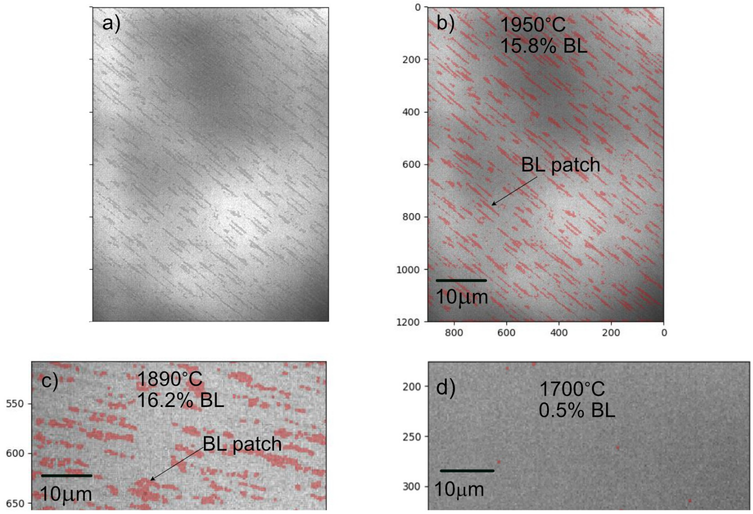

Figure 4.7: (a) Transmission mode optical microscopy image, used to quantify the graphene BL coverage percentage. Digital image processing such as image saturation and gamma corrections are adjusted to enhance the contrast between ML and BL graphene. In images (b) - (c) red areas are the BL graphene regions highlighted by the image processing Python script. It also shows the progress in the growth quality after the cyclic optimization procedure. Here temperature is used as one of the parameters to suppress BL growth.

patches. This is feasible because, with each additional layer of graphene, light absorption increases by approximately 1.3 %. It is worth noting that free-standing ML graphene exhibits an absorption of about 2.3 %, but the SiC substrate due to its refractive index ($n = 2.65$) reduces this contrast by a factor of 2. This method proves useful for a rapid assessment of epigraphene quality across a large area and in real time. Figure 4.7(a) provides an illustration of an image produced using this approach, where BL inclusions are clearly distinguishable due to their darker appearance. It is important to note that optical imaging alone cannot confirm the presence of ML epigraphene. Its primary utility lies in swiftly assessing whether a given sample exhibits sufficient homogeneity for further processing. In this thesis, Olympus MX50 is extensively used in its transmission mode for imaging epigraphene.

Figure 4.7(b)-(c) illustrates the cyclic growth optimization process. Here, the parameter that is used to optimize the growth is the temperature. Image from the transmission mode microscopy is passed through the image processing script, written in Python, which identifies the darker BL patches, highlights them in red, and calculates the % area covered by them. Once the BL coverage is identified, the subsequent growth process is tuned in terms of substrate preconditioning, process temperature, and pressure, crucible design, etc.

Atomic force microscopy

While optical microscopy offers a convenient and fast means to assess material homogeneity, it lacks the essential spatial resolution required to discern intricate nanoscale features. For achieving high resolution, a scanning probe technique like Atomic Force Microscopy (AFM) proves valuable. AFM can provide atomic-level resolution in height, enabling the imaging of sample topography (see Figure 4.8(a)). The lateral resolution is contingent upon the AFM tip size and typically falls within the range of 5 to 10 nm.

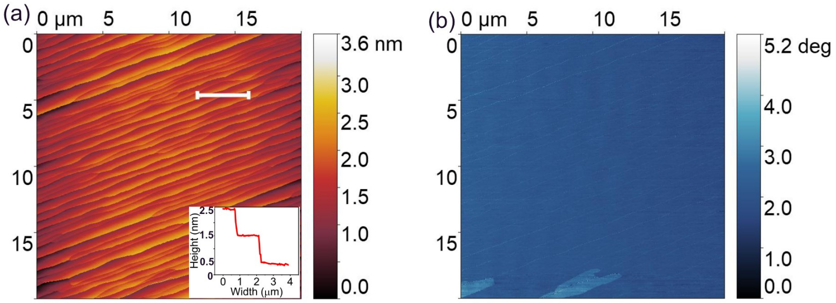

Figure 4.8: Tapping mode Atomic Force Microscopy (AFM) image of the epigraphene over a 20 µm × 20 µm region. (a) Height image showing the topography of epigraphene after linear background subtraction. The prominent feature observed here is the steps on the surface of SiC that manifest during the growth process. The inset presents a cross-sectional height profile along the white line, illustrating that these steps possess a height on the order of ≈ 1 nm, approximately equivalent to the unit cell height of 4H-SiC and step width of around 1-2 µm. Graphene, while not directly visible, envelops the SiC staircase like a carpet. (b) AFM phase image distinctly highlights the existence of a different material (lighter shade of blue), which is likely to be BL patches.

For our samples, topography and phase contrast images in AFM tapping mode, provide enough information about the quality of the growth. Tapping mode AFM stands out as the most commonly employed mode. In all AFM modes, a cantilever with a sharp tip oscillates near its resonance frequency. In tapping mode, the tip is periodically brought close to the sample, and the variations in oscillation amplitude caused by interactions with the surface are utilized to derive the topographical information. Additionally, the phase signal indicates the phase difference between the excitation signal applied to the cantilever and the measured output signal. This signal provides information about the mechanical properties and viscoelasticity of the surface. In other words, it reveals how the surface responds to the interaction with the AFM tip as it oscillates. It proves useful for distinguishing between different graphene domains, which can be challenging to differentiate based solely on topography. Nevertheless, it primarily reveals whether two regions possess varying graphene thicknesses (in Figure 4.8(b) shown in a lighter shade of blue) rather than providing an exact layer count. Image 4.8 is from Scanning Probe Microscope (SPM) - Bruker Dimension ICON and is used for all the AFM analysis.

Raman spectroscopy

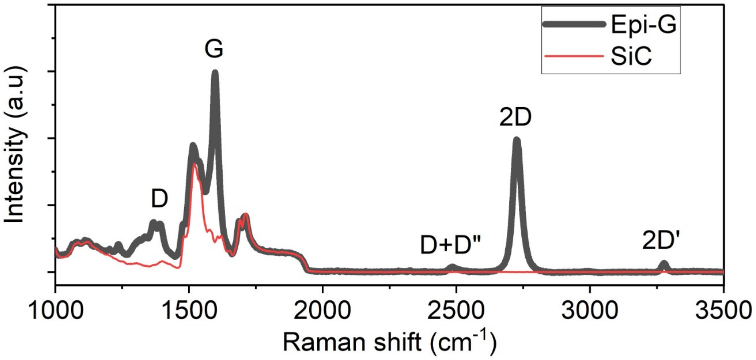

Figure 4.9: Raman spectrum of epitaxially grown graphene over SiC. In black Raman spectrum of graphene over 4H-SiC substrate, measured with 532 nm wavelength laser. In red is the Raman spectrum of the 4H-SiC substrate alone, which forms the background for the spectrum of graphene. Ignoring the background one can identify the Raman signatures of graphene alone as labeled in the plot.

Raman spectroscopy is widely employed for graphene characterization due to its ability to provide valuable insights into layer count, doping, and strain. This technique relies on the detection of inelastic scattering of monochromatic light and examines the relaxation of vibrational modes within a crystal. As a result, it unveils important details about the crystal structure lying beneath. Figure 4.9 shows the Raman spectrum of epitaxially grown graphene over SiC (black) and bare SiC substrate (red) taken in WITec alpha300 R-Raman microscope using a 532 nm laser.

The spectrum in the black shows the Raman bands of graphene with the SiC spectrum as the background. Since epitaxial graphene grows after the buffer formation, the presence of buffer also influences the Raman peaks of epigraphene. For graphene, D peak at 1360 cm^{-1} requires defect for its activation [52] The study by Fromm, F. et al showed, that the buffer layer has a Raman broad band at approximately 1355 cm^{-1}, which makes it hard to distinguish the D peak signature of epigraphene and buffer layer from one another [53]. But the absence of D′ at ≈ 1620 cm^{-1} and D+D′ at ≈ 2950 cm^{-1} (due to disorder) and presence of prominent 2D and 2D′ peaks indicates defect free growth of epitaxial graphene [54], [55]. D+D″ (also sometimes referred as G*) at ≈ 2500 cm^{-1} is identified purely for single layer graphene and disappears for increasing layer numers [55].

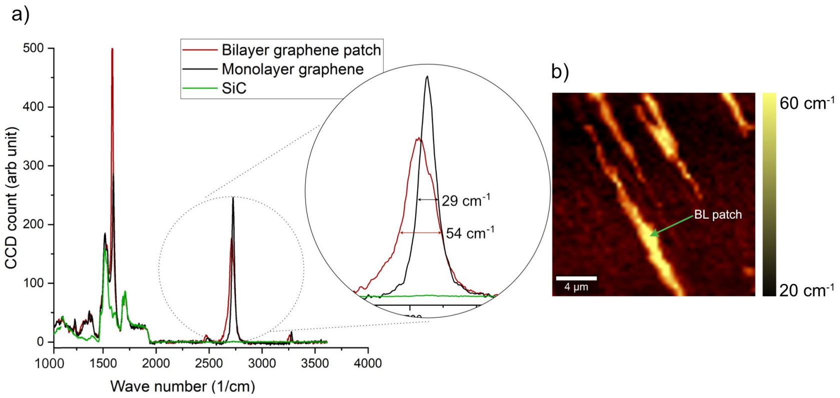

Figure 4.10: (a) Raman spectra for monolayer (ML) and bilayer (BL) graphene, and silicon carbide (SiC). The circular inset shows the Full Width at Half Maximum (Full-Width Half Maximum (FWHM)) of the 2D peak of ML (FWHM = 29 cm^{-1}) and BL graphene (FWHM = 54 cm^{-1}). (e) Raman mapping (15 µm x 15 µm) of the epigraphene sample grown at T = 1950° C.

The identification of BL patches becomes readily apparent when examining the Raman mapping of the 2D peak, as depicted in Figure 4.10(b). This phenomenon occurs because the stacking of multiple graphene layers leads to the broadening of the 2D peak, as demonstrated by Lee et al. [56]. By quantifying the FWHM of this peak, it becomes possible to differentiate between the broader and narrower peaks within the mapping. In our sample, ML graphene exhibits an FWHM of approximately 29 cm^{-1}, whereas for BL it measures 54 cm^{-1}.

CHAPTER 5

Quantum-limited electrical contacts to 2D materials

Two approaches exist for fabricating electrical contacts to two-dimensional (2D) materials: top contact and edge contact. Since the surface of the 2D material such as epigraphene is free of dangling bonds, it does not tend to form covalent bonds with metal. This results in van der Waals (vdW) gap between contact metal and 2D material leading to poor and irreproducible contacts [16]. Figure 5.1(a) shows the statistics for contact resistance values of top contact deposited over epigraphene. Even for the clean metal-graphene interface by utilizing shadow mask evaporation for metallization a large spread from a few Ohms to 100 KΩ is seen in the contact resistance values [32]. Building upon the edge contact technique [57], this thesis develops a scalable method for making contacts to epigraphene (refer to **Paper A**), resulting in median values of the one-dimensional specific contact resistances $\tilde{\rho_c} \approx 67$ Ωμm. These values adhere to the Landauer quantum limit $\rho_c \approx n^{-1/2}$ and consistently reach values of $\rho_c < 50$ Ωμm at high carrier density n (refer to Figure 5.1(b)).

5.1 Edge contact fabrication and development

Density function theory (DFT) has previously demonstrated that edge contacts exhibit shorter bonding distances and stronger hybridization (orbital overlap) compared to top contacts [58]. First proposed for carbon nanotubes, edge-contacts (a.k.a.

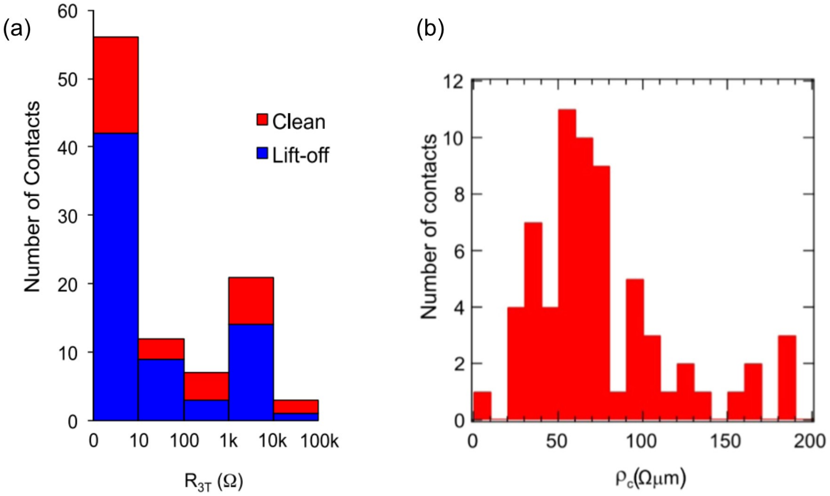

Figure 5.1: (a) Shows contact resistance statistics from [32], for 97 individual contacts measured by three-terminal resistance under quantum Hall conditions. A spread in contact resistance between 10 to 100 KΩ is observed, even for devices fabricated with clean metal-graphene interfaces. Here metal-graphene contact perimeter width varies as, $w = 4, 8, 24$, and 40 μm(b) Histogram of almost 70 edge contacts for nine devices placed on three different epigraphene chips. Contacts with higher $\rho_c > 110$ Ωμm are due to lowly doped graphene $n < 1 \times 10^{11}$ cm^{-2}. Histogram gives a median ρ_c value of 67 Ωμm, indicating a strict control over contact resistance.

end contacts) [59], [60] is currently one of the most successful and popular methods to achieve good electrical interfacing to 2D materials. The most common implementation of this method, as originally demonstrated by the Columbia group for graphene [57], the 2D layer is encapsulated by hexagonal boron nitride (hBN). The entire stack is then patterned and etched to expose only the edge of the graphene layer, which is subsequently metalized, to form a one-dimensional (1D) electrical contact along the edge of graphene with specific contact resistances as low as $\rho_c = 150$ Ωμm. Inspired by the method of forming edge contacts to graphene/hBN heterostructures, in this thesis, a fabrication strategy for the scalable microfabrication of electrical contacts without the need for hBN encapsulation based on the tri-layer resist system is developed. The edge contact fabrication process is described in the section 3.1. A detailed step-by-step procedure of the same is explained in Part II. Recipe C. This technique involves two EBL steps and fulfills the needs of most electronic devices. Figure 5.2 shows the line profile of the fabricated contacts. The protrusions on the

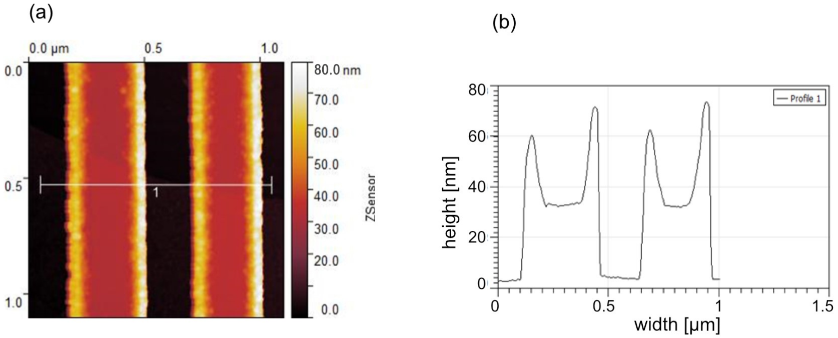

Figure 5.2: (a) AFM image of Ti-Au (5 nm-30 nm) contacts deposited using a single EBL exposure as explained in the section 3.1. The AFM line profile of the contacts in (a) shows protrusions at the edges of the metal contact.

surface of metal contacts are due to the deposition of metal on the walls of the bottom resist layer, which in some applications might prevent subsequent metallization steps. This can be eliminated by pre-exposing the bottom and middle resist layers with a slightly scaled version of the actual contact design and with 15 % of the base dose. On top of the pre-exposed resist layers, the third layer of resist is spun and another EBL exposure with the base dose is carried out. Schematic 5.3 shows the step-by-step procedure.

To shape and isolate the devices, step 2 of the microfabrication procedure explained in the 3.1 is carried out. So in total, there will be three lithography steps involved to form the final usable device. Figure 5.4 shows the AFM image of the metal contact deposited using this technique, as seen the metal surface is flat without any protrusions.

5.2 Transmission electron microscopy analysis

After establishing the contacts, it is crucial to examine the physical interface between the epigraphene and the metal to confirm the presence of edge contacts. Figure 5.5(a) presents an illustration depicting the formation of edge contacts between epigraphene and Ti/Au, as visualized using Transmission Electron Microscopy (TEM). In this material, our process results in contact to graphene that is directly in contact with the edge of the crystal and a small portion of its upper surface ($d < 20$ nm), making contact with the metal adhesion layer (Ti). Figure 5.5(b) provides an overview TEM image of the vicinity surrounding the graphene-metal contact, while Figure 5.5(c) offers a zoomed-in TEM image of an area located ap-

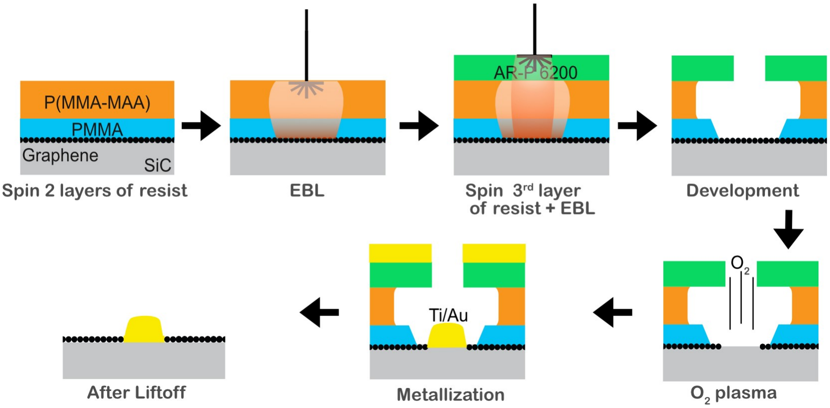

Figure 5.3: Schematic representation of the EBL lithography steps to eliminate the protrusions on the surface of the contact, In the first exposure step, the bottom two resist layers are exposed with 15 % of the base dose using a scaled-up version of the original contact design. After this third layer of resist (AR-P 6200) is applied and exposed with the base dose.

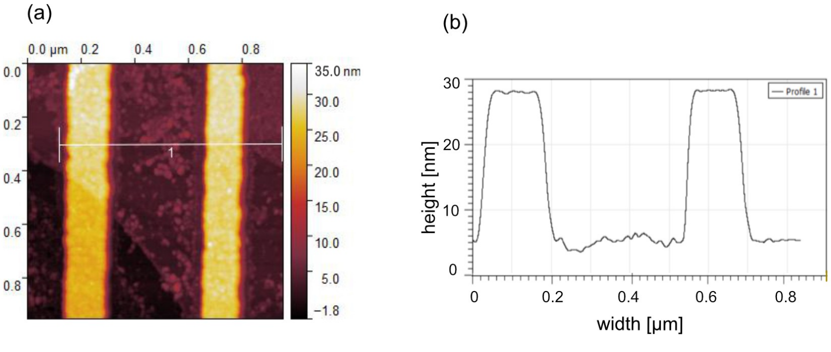

Figure 5.4: (a) AFM image of Ti-Au (5 nm-30 nm) contacts deposited using a double EBL exposure. (b) The line profile of the AFM image shows that double EBL exposure eliminates the edge protrusions on metal contact.

proximately 30 nm away from the metallization site (highlighted by the yellow square in Figure 5.5(b)). This close-up image reveals the presence of two carbon layers of epigraphene, with the buffer layer in contact with SiC and graphene forming the uppermost layer. These two carbon layers exhibit atomic flatness and continuously cover the entire SiC substrate, excluding the contact region. Concerning the specifics of the metal-graphene interface, we have harnessed Scanning Transmission Electron Microscopy (STEM) combined with Electron Energy Loss Spectroscopy (EELS) to pinpoint the boundary where graphene makes contact with the metal (Ti). Figure 5.5(d) represents a false-color map displaying the chemical mapping obtained from STEM-EELS at the contact's edge. This mapping distinctly shows that graphene (green) is indeed in contact at the edge while a portion of its upper surface interfaces with titanium (red), extending over an area of approximately 18 nm. This chemical analysis establishes that the metal-graphene contact region primarily occupies the area delineated by the dashed box in Figure 5.5(b).

5.3 Electrical characterization

To illustrate the effectiveness of this fabrication method in achieving low contact resistance, the standard Transfer Length Method (TLM) is employed in the initial characterization efforts. This method involved creating graphene test structures with channel widths denoted as W, along with electrical contacts placed at varying distances denoted as L, as shown in Figure 5.6. The resulting two-terminal resistance, known as R_{2T}, was then measured between these adjacent contacts (refer to Equation 3.4).

In total, TLM measurements on 12 distinct epigraphene structures that are patterned across five individual epigraphene chips are conducted (refer to Figure 5.7). Before initiating these measurements, it was essential to encapsulate the samples to exercise precise control and stabilization of epigraphene's doping levels, as described in a prior study [61]. The graphene channel width, denoted as W, ranged from 8 to 64 µm, while the distance, L, between contacts spanned from 1 to 128 µm. An illustration of a TLM plot depicting R_{2T} versus L for the two largest epigraphene devices, $W = 64$µm with a total length of 270 µm, is presented in Figure 5.6. In this graph, each resistance data point was determined through linear fits to current-voltage ($I - V$) curves under a voltage bias up to $V = 1$ mV.

A noteworthy observation is the similarity in the slopes of these two devices, both yielding a value of $dR_{2T}/dL = 119$ Ω/µm. This corresponds to a sheet resistance of 7616 Ω/□. As for the intercept, the linear fits indicate a R_C value that is effectively zero, with an uncertainty of ±20.5 Ω. In quantitative terms, this demonstrates that the contacts offer a remarkably low contact resistance across all the TLM structures fabricated, showcasing excellent reproducibility. The relatively low uncertainty in the

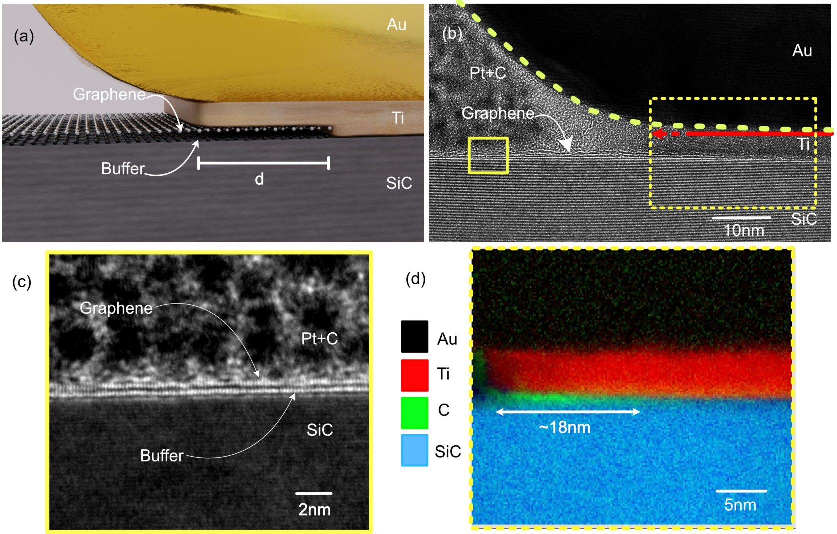

Figure 5.5: Transmission Electron Microscopy (TEM) examination of contacts to epigraphene. (a) Depiction of the graphene and buffer layer in connection with Ti/Au contact. (b) TEM image exhibiting the epigraphene-metal contact. The Pt + C layer serves as a protective layer deposited during TEM sample preparation. (c) TEM image of the region enclosed by the yellow rectangle in panel (b), illustrating the presence of epitaxial graphene and buffer over SiC. (d) STEM-EELS chemical mapping of the interface between graphene and metal contacts. The chemical analysis discloses that epigraphene is contacted at the edge, while Ti covers the graphene top surface over a distance $d \sim 18$ nm.

TLM measurements is common and may stem from factors such as local variations in material doping or the geometry of the fabricated devices.

To accurately quantify the contact resistance of the contacts, Hall bar geometry is used to exploit the possibility offered by epigraphene to characterize the transparency of the metal-graphene interface using a three-probe measurement R_{3T} under Quantum Hall Effect (QHE) as explained and shown in Figure 3.5(b). Figure 5.8(a) shows the typical phenomenology of the metal-graphene interface is that of edge contacts, i.e., the linear dependence of $R_C(\Omega)$ on the inverse contact perimeter $1/l$. Furthermore, this behavior in fact extends to graphene in QHE [62], [63]. In these measurements, five devices on the same chip were used, with a carrier density tuned to approximately $n \approx 10^{10} - 10^{11}\,\mathrm{cm}^{-2}$. To enable comparisons across devices on different chips a total of nine devices spanning three distinct epigraphene chips are

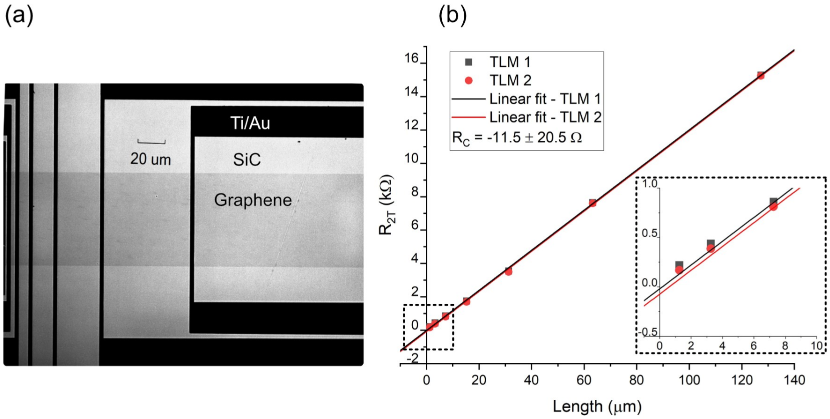

Figure 5.6: Analysis of contacts to epigraphene using the Transfer Length Method (TLM). (a) Optical microscopy image in transmission mode illustrating the fabricated edge-contacted TLM device. (b) Example of TLM data for two devices with 64 µm wide epigraphene channels measured at T = 300 K. It is important to note that the resulting fit yields a negative (unphysical) R_C, approaching zero, with an uncertainty of ±20.5 Ω. Inset: a closer examination of the TLM data for L < 10 µm.

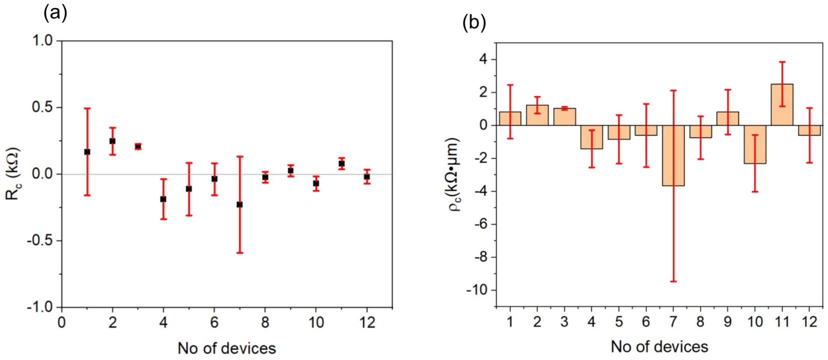

Figure 5.7: TLM assessments were performed on the 12 epigraphene device structures patterned across five epigraphene chips. (a) The R_C values (kΩ) correspond to the 12 devices, where 7 of them yield negative (non-physical) results. (b) The computed values of ρ_C indicate a substantial diversity in resistance, with a mean of -500.74 Ωµm and a standard deviation of ±1770.24 Ωµm, which are not physically viable.

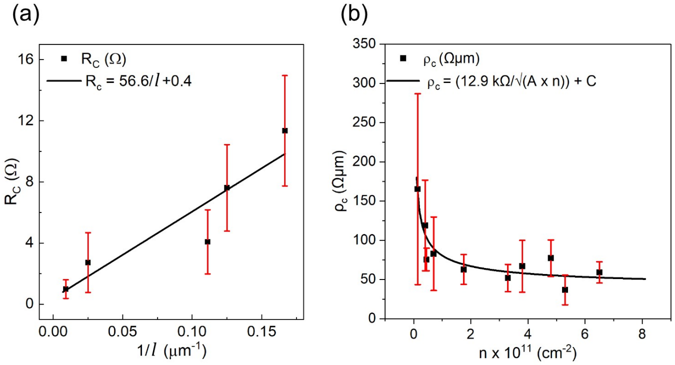

Figure 5.8: Characterization of the metal-graphene interface was conducted using the three-probe configuration in the quantum Hall regime (T = 4 K, B = 5 T). (a) R_C (Ω) was plotted against the inverse perimeter length for five devices situated on the same chip. The linear fit resulted in a resistance $R_C(l) = 56.6/l + 0.4\ \Omega$. (b) ρ_C was plotted against carrier concentration. The solid line represents a fit to $\rho_C = h/(2e^2\sqrt{n_{eff}}) + C$, where $n_{eff} = A \times n$. Here, n_{eff} signifies an effective carrier density at the carrier injection points (hot spots). The fits returned the values A =19.7 and C = 34.5 Ωµm. The error bars represent one standard deviation from the mean value.

measured. Here, one-dimensional (1D) specific contact resistance is $\rho_c = R_c \times l$, where l represents the perimeter length. Figure 5.1(b) presents a histogram of ρ_c values obtained from nearly 70 Ti/Au edge contacts, showing a mean value of $\overline{\rho_c} = 82$ Ωµm and a median value at $\tilde{\rho_c} = 67$ Ωµm. These statistics demonstrate the consistent ability of the tri-layer resist method to produce contacts with low contact resistance.

The variability in contact resistance values can be attributed to differences in doping levels in epigraphene across various chips, as shown in Figure 5.8(c). This figure displays specific contact resistance data in relation to carrier density, measured using low-field magnetoresistance, specifically $n = 1/eR_H$, where R_H represents the Hall coefficient $R_H = dR_{xy}/dB$, and e represents the elementary charge. The specific contact resistance follows the functional form for the Landauer quantum limit of resistance, characterized by an inverse square root dependence on carrier density, denoted as $\propto n^{-1/2}$. As the charge density decreases below $1 \times 10^{11}\,\mathrm{cm}^{-2}$, the larger error bars in the measurements can be attributed to the increased influence of (local) charge inhomogeneity at the graphene-metal interface, often referred to as charge puddles.

It is important to note that the R_C measurements in the three-probe geometry during QHE primarily originate from the hotspot region, where current injection occurs, and where all dissipation and voltage drop take place (see Figure 3.5(b)). From the $\propto l^{-1}$ and $\propto n^{-1/2}$ dependencies characterizing contact resistance, it appears that at the hotspot regions, electron transfer at the interface between metal and graphene in a high magnetic field (i.e., in the QHE regime) maintains similarities with electron injection into graphene at $B = 0$ T. One notable difference is an effective carrier density roughly an order of magnitude higher than that extracted from the low-field context.

5.4 Conclusions

The approach for creating edge contacts in epigraphene could be readily extended to a diverse range of materials, encompassing both bulk and low-dimensional substances. The demonstration using e-beam lithography highlights the potential for scalable fabrication of edge contacts to 2D materials by employing a narrow-wide-narrow opening in the resist. It is conceivable that similar outcomes might be achievable through optical lithography methods, albeit with some adjustments and careful selection of resist layers.

The process could be further refined to achieve a distinct contact profile by fine-tuning various lithography parameters, including the choice of resist, solvents, and irradiation dose. The ability to bypass the encapsulation of the 2D material channel, such as with hBN, to establish edge contacts could be particularly advantageous for applications like chemical or gas sensors, where the channel material must be exposed to chemical analytes to enable transduction. Moreover, robust electrical interfaces play a crucial role in achieving low noise performance in practical electronic devices.

The capability to achieve metal deposition through thermal evaporation and sputtering provides an additional advantage in designing effective electrical interfaces, which is essential for exploring the electrical properties of emerging materials.

CHAPTER 6

Hall sensor and noise performance

Hall sensors detect magnetic fields by measuring the Hall voltage V_H induced by an external field B. High device sensitivity is crucial as it results in a substantial magnitude of the V_H response to an external field. Three significant material-related metrics assess the performance of a Hall sensor. The first is the current-related sensitivity S_I, expressed as $|V_H|/I_B$, measured in units of V/(AT). This parameter is fundamentally determined by the Hall coefficient R_H, denoted in units of Ω/T. The second metric is the voltage-related sensitivity S_V, calculated as $|V_H|/V_B$, with units in V/(VT). The ultimate constraint for S_V is the carrier mobility μ, defined as R_H/ρ, measured in units of m^2/Vs. The third and final metric is the magnetic field detection limit B_{MIN} (units $\mathrm{T}/\sqrt{\mathrm{Hz}}$), represented as $V_N/(I_B R_H)$, where V_N is the voltage spectral density, in units of $\mathrm{V}/\sqrt{\mathrm{Hz}}$. Graphene is a promising material for Hall elements due to its high mobility and the ability to adjust the carrier density n towards charge neutrality (Dirac point). A low carrier density is desirable because it increases the Hall coefficient, $R_H = 1/(ne)$. Additionally, decreasing n towards neutrality would increase both S_I and S_V, as the mobility $\mu = R_H/\rho$ of graphene is inversely proportional to carrier density and follows the relation $\mu \propto 1/\sqrt{n}$. Although low n leads to an increase in ρ, following $\rho \propto 1/n$, in the limit where charged impurity scattering dominates. Yet decreasing n can actually result in a lower magnetic field detection limit, $B_{MIN} = V_N/(I_B R_H)$ $(\mathrm{T}/\sqrt{\mathrm{Hz}})$. If Johnson–Nyquist noise dominates, then $V_N = V_{TH} \propto \sqrt{4k_B T\rho}$, where k_B is the Boltzmann constant and

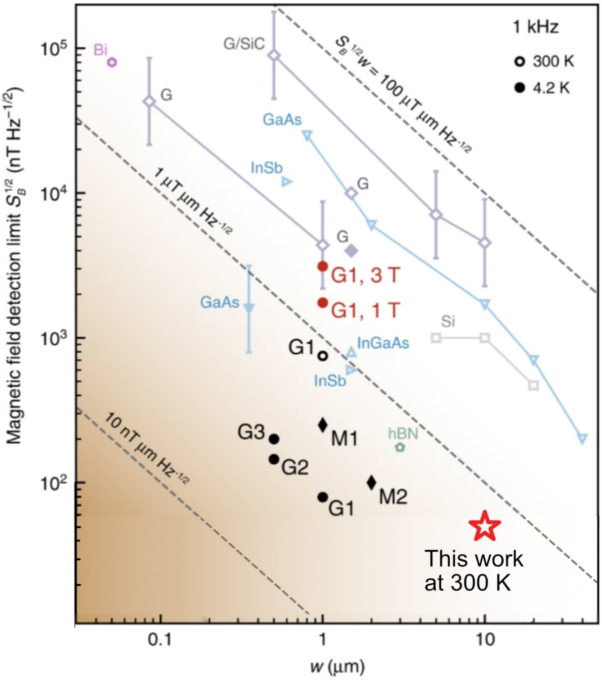

Figure 6.1: Comparison of magnetic field detection limit [64]. Epigraphene hall sensors fabricated in this work outperform the best-reported Hall sensors in the literature.

T is the temperature. The detection limit scales as $B_{MIN} \propto V_N/R_H \propto \sqrt{n}$ for a fixed I_B. Disorder in graphene samples prevents it from reaching true charge neutrality, high-quality graphene can approach low carrier densities of $n \sim 10^{10}$ cm^{-2} at cryogenic temperatures.

In this chapter, results from the **Paper B** and **Paper F** are discussed. The epitaxial growth parameters were meticulously optimized to achieve high-quality graphene on SiC, resulting in a significant reduction of bilayer (BL) graphene domains to less than 0.1 % coverage of the surface [40], [51]. Furthermore, our device fabrication process incorporates the edge contact approach consistently yielding contact resistance values below 50 Ωµm [65]. Depending on the carrier density, these molecular-doped epigraphene Hall sensors can achieve room temperature sensitivities of $S_V = 0.23\,\mathrm{V/(VT)}$, $S_I = 1440\,\mathrm{V/(AT)}$, and exhibit remarkable magnetic field detection limits as low as $B_{MIN} = 27\,\mathrm{nT}/\sqrt{\mathrm{Hz}}$ at 20 kHz. Figure 6.1 shows a com-

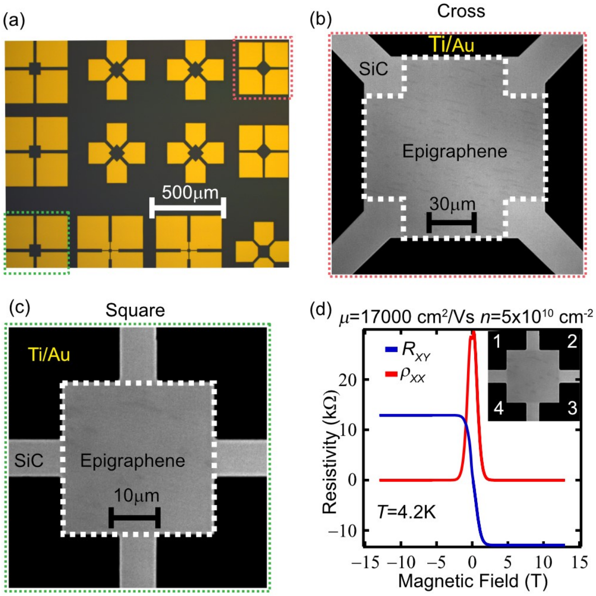

Figure 6.2: (a) Optical micrograph image illustrates a chip housing multiple Hall sensor devices based on epigraphene. (b) and (c) are the grayscale images taken in transmission mode optical microscopy, depicting the two distinct device geometries: square and cross. (d) To confirm the electronic quality of doped epigraphene Hall sensors, QHE measurements are employed. The inset displays four contact pads labeled for conducting van der Pauw (vdP) measurements. For quantum Hall measurements, R_{XY} is determined using current biasing between contacts 1-3 and voltage measurements between contacts 2-4, while ρ_{XX} employs current biasing between 2-3 and voltage measurements between 1-4.

parison of epigraphene Hall sensors in comparison to the Hall sensors reported in the literature. Thermally stabilized devices are capable of operation up to 150 °C while maintaining sensitivities of $S_V = 0.12\,\mathrm{V/(VT)}$, $S_I = 300\,\mathrm{V/(AT)}$, and achieving a minimum detectable magnetic field of approximately $100\,\mathrm{nT}/\sqrt{\mathrm{Hz}}$ at 20 kHz.

6.1 Hall sensor devices

Figure 6.2(a) shows an optical microscopy image of fabricated Hall sensors. These Hall sensors are configured with symmetric square or cross-shaped device geometries, selected for their capacity to maximize S_V [66], [67]. Two illustrations of epigraphene

Hall sensors are presented in Figure 6.2(b-c). The fabrication of the device employed the microfabrication technique described in the section 3.1. Metal contacts were applied via physical vapor deposition of a 5 nm Ti layer followed by an 80 nm Au layer. Each Hall sensor is equipped with four electrical contacts, and the extraction of carrier density (n) and sheet resistance (ρ) is typically performed using van der Pauw (vdP) measurements. Quantum Hall Effect (QHE) measurements are conducted at cryogenic temperatures to verify the high electronic quality and uniform doping of the doped Hall sensors.

6.2 Carrier density modulation

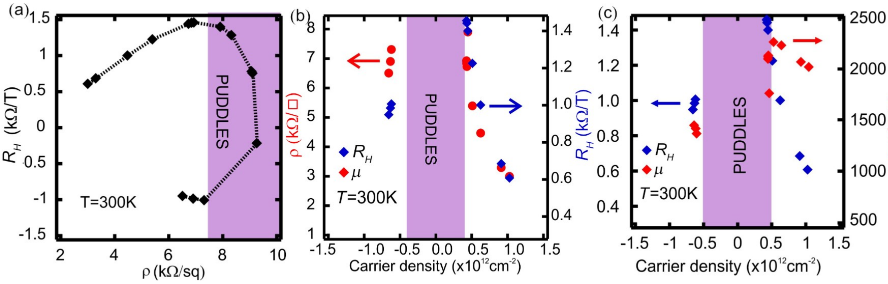

Figure 6.3: Carrier density tuning of epigraphene Hall sensors at room temperature. (a) The R_H variation w.r.t. ρ as the epigraphene carrier density crosses the Dirac point. The purple region marks the disordered puddle regime. (b) R_H and ρ as functions of carrier density, demonstrating that both exhibit analogous carrier density dependencies $\propto 1/n$. (c) R_H and μ relative to carrier density. The carrier mobility displays a decline proportional to $1/n$. Data points within the puddle region have been excluded due to carrier indeterminacy.

The samples are doped using five polymer layers for maximal stability as explained in Part II. Recipe D, and their final carrier densities are tuned to a wide range of values in order to cover performance over a broad spectrum. Figure 6.3 shows the range of attained carrier density, along with the respective values for R_H and ρ. The performance of doped epigraphene Hall sensors is evaluated for doping levels ranging from $n = 5 \times 10^{11}$ to 2×10^{12} cm^{-2}. The lowest doping level corresponds to the charge puddle regime $|n| < 5 \times 10^{11}$ cm^{-2} and is limited by room temperature disorder. This is attributed to the fact that, at 300 K, the epigraphene sample displays an uneven distribution of charge carriers, forming electron-hole puddles. Inside the puddle regime, the single-band carrier density is poorly defined (refer Figure 6.3). This results in potential fluctuations P(D), particularly around the

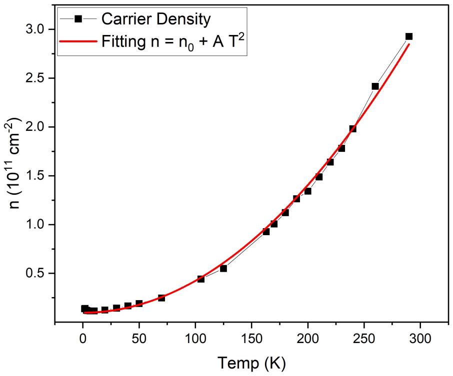

Figure 6.4: The temperature dependence of the effective carrier density n_e, obtained from [17], is shown in black. The red data points represent the fit using the model for disorder-induced temperature-dependent transport from [22], enabling the extraction of the disorder strength s.

charge neutrality point [68].

$$P(D) = \frac{1}{\sqrt{2\pi s^2}} exp\left(-\frac{D^2}{2s^2}\right) d\varepsilon \tag{6.1}$$

where, $D = (\varepsilon - E_F)$ is the disorder potential, s is the standard deviation of disorder potential. At a given temperature the amount of charge carriers in graphene is determined by s. The value of s is calculated by fitting it to the temperature dependence of charge carrier density $n_e(T)$ [22].

$$n_e(T) = n_0 \left[1 + \frac{\pi^2}{3}\left(\frac{k_B T}{s}\right)^2\right] \tag{6.2}$$

Figure 6.4 shows one such fitting for $n_e(T)$ obtained for epigraphene at charge neutrality point from our previous work [17]. We find that the root mean square (RMS) value of the disorder potential s in our samples is about 16 meV.

6.3 Cross-correlated spectrum analysis

Figure 6.5 provides a comparison between the noise floor of the measuring instruments in the cross-correlation spectrum (CC) and single amplifier spectrum (SA) configurations. The Appendix B explains the instrumentation setup and the underlying theory behind the cross-correlated power spectrum analysis. All measurements

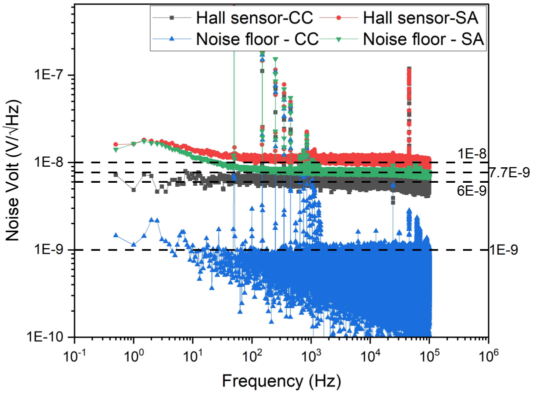

Figure 6.5: Comparing the spectrum of the single amplifier (SA) to the cross-correlated (CC) spectrum reveals that the SA configuration exhibits a noise floor 7 times higher than the CC configuration. The measured noise in the SA configuration, with an input resistance of 2.3 KΩ, surpasses the expected thermal noise $\sqrt{(4k_BTR)}$, primarily due to the inclusion of instrumentation noise.

were conducted at room temperature. The noise floor of the instrument refers to the spectrum obtained when the input is shorted. In the CC configuration, the noise floor is nearly one order of magnitude lower than that of the SA configuration, reaching $S_V = 1$ nV/$\sqrt{\text{Hz}}$. The epigraphene device exhibits a noise floor of 6 nV/$\sqrt{\text{Hz}}$ in the CC configuration, matching its thermal noise $\sqrt{(4k_BTR)}$ for $R_{2T} = 2.3$ KΩ and 300 K. On the other hand, the noise floor of the SA configuration itself is 7.7 nV/$\sqrt{\text{Hz}}$. This finding suggests that our epigraphene devices showcase lower noise levels compared to the measuring system in the SA configuration, and can only be accurately measured in the CC configuration. Epigraphene devices measured in the SA configuration consistently exhibit higher noise values than anticipated, stemming from the addition of instrumentation noise atop the signal of interest.

6.4 Noise characterization

The noise performance of a sensor has a significant impact on the detection limit. For Hall sensors, the minimum detectable magnetic field is given by $B_{MIN} = V_N/(I_BR_H)$, where V_N represents the noise voltage spectral density. Figure 6.6 illustrates the noise characteristics of epigraphene Hall sensors measured using the setup as shown in Appendix B: Figure B.1(b). Table 6.1 presents a comparison of epigraphene Hall sensor with the values reported in the existing literature.

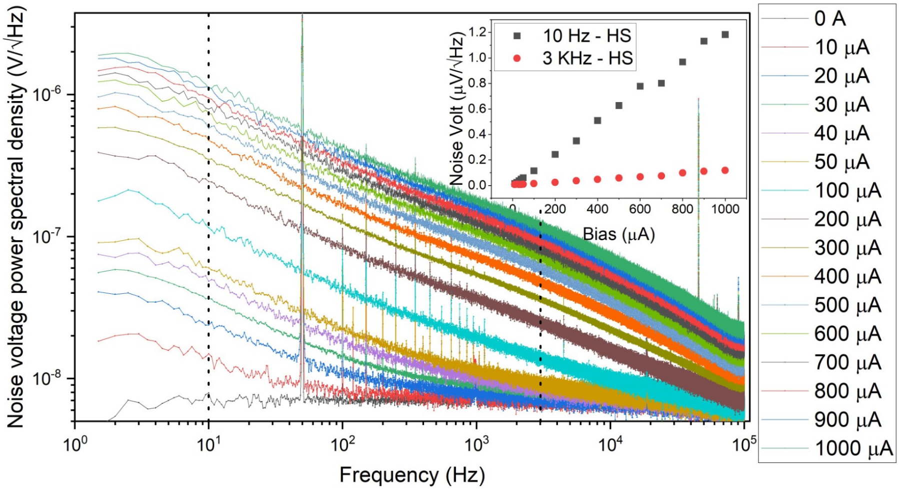

Figure 6.6: The $1/f$ noise spectrum is influenced by bias in the following manner: (a) illustrates an increase in $1/f$ noise with the application of bias to the sample, while (b) portrays the noise amplitude against the bias current at 10 Hz and 3 KHz, demonstrating a linear trend that points towards a resistive noise contribution.

The initial test assessed noise for 2, 3, 5, 6-Tetrafluoro-tetracyanoquinodimethan (F4TCNQ) encapsulated devices by applying current bias as low as 10 µA. The $1/f$-noise exhibits a corner frequency below 100 Hz, with noise saturation at higher frequencies. Noise measurements are limited to 100 kHz because of the amplifier's higher cut-off frequency. The calculated thermal noise, obtained from measurements of the input resistance of the Hall sensor, aligns with the direct noise measurements, indicating thermal noise from the Hall sensor is the primary noise source.

In practice, flicker noise is characterized by the Hooge parameter α_H, which is commonly used as a figure of merit to benchmark materials, and is based on empirical formula [76].

$$\frac{S_V}{V^2} = \frac{S_I}{I^2} = \frac{S_R}{R^2} = \frac{\alpha_H}{Nf} \tag{6.3}$$

where S_V, S_I, S_R are the PSD of the fluctuations in the values of voltage V, current I and resistance R. N is the charge carrier number and f is the frequency. N is related to the device size by the relation $N = l^2/(q\mu R)$, where l is the length of the sample, q is the elementary charge, μ is the mobility and R is the sample resistance. From this, we can see the dependence of noise PSD over device geometry $S_V \propto 1/l^2$.

Inset in Figure 6.6 illustrates the relationship between noise amplitude and bias

Type	S_I (V/AT)	S_V (V/VT)	B_{MIN} (nT/$\sqrt{\text{Hz}}$)	Freq (kHz)
Si [23], [69]	100	0.1	50-500	0.1-100
InSb [23], [70]	140-700	1-7.2	1-60	0-50
GaAs [23], [70]	30-3200	0.6-1	10-6000	0-50
hBN-G [71]	4100	2.6	50	3
CVD [72]	2093	0.35	100	3
CVD [73]	1200	N/A	300000	3
CVD [74]	97	0.03	400000	1
Epi-G [75]	1021	0.3	2000	3
Doped Epi	1080	0.23	60,40	3,20
Doped Epi	1442	0.21	47,27	3,20

Table 6.1: A comparative table displaying the figures of merit for Hall sensor performance at room temperature. The final two rows represent performance examples of doped epigraphene Hall sensors from this study.

current. It reveals that noise amplitude scales linearly with bias current. The Hooge parameter α_H, characterizing the noisiness of the system, can be estimated by fitting a linear curve to V_N versus I_B, using the corresponding input resistances (3500-7000 Ω), carrier densities ($4.4 \times 10^{11} - 1.38 \times 10^{12}$ cm^{-2}), device area (100×100 µm^2), and frequency (3 kHz). The resulting Hooge parameter falls within a range of $\alpha_H \approx 10^{-5} - 10^{-4}$, depending on the doping level. In comparison, this value is lower than reported values of suspended graphene samples [77] and is comparable to GaAs [78], suggesting that the noise level for doped epigraphene Hall devices is excellent.

6.5 Comparison of noise for different encapsulations

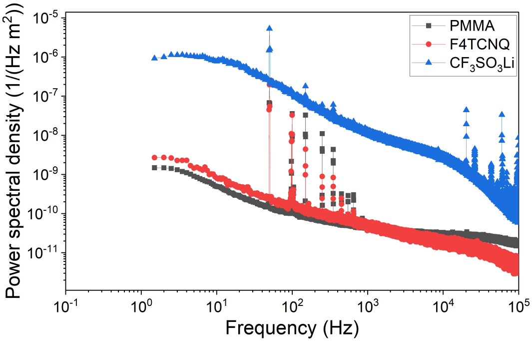

Figure 6.7: Comparison of noise PSD of Poly(methyl-methacrylate) (PMMA) ($n = 7 \times 10^{12}$ cm^{-2}), 2, 3, 5, 6-Tetrafluoro-tetracyanoquinodimethan (F4TCNQ) ($n = 4.2 \times 10^{11}$ cm^{-2}), and solid electrolyte lithium triflate CF_3SO_3Li ($n = 4 \times 10^{11}$ cm^{-2}). PSD is normalized with respect to device geometry.

Figure 6.7 depicts a comparison of the correlated noise PSD for epigraphene encapsulated in PMMA, F4TCNQ, and solid electrolyte lithium triflate CF_3SO_3Li. All the spectra are normalized with respect to the device area. The solid electrolyte exhibits the highest noise level in comparison to the other encapsulation methods. In contrast, the PMMA encapsulated device showcases the lowest noise level. This disparity can be attributed to PMMA's ability to shield graphene from environmental influences while minimally affecting its electrical properties. The molecular dopant F4TCNQ produces a similar effect as PMMA since the molecules are infused in the PMMA polymer matrix. A slight increase in the noise level is observed with F4TCNQ, as the charge carrier density in graphene is adjusted near to the Dirac point.

Each encapsulation method exerts an influence on the properties of graphene, which is characterized in direct current (DC) measurements in terms of sheet resistance R_S ($\Omega/\square$), Hall coefficient R_H (Ω/T), carrier concentration n (/cm^2), and carrier mobility μ (cm^2/Vs) as outlined in table 6.2. Owing to the high susceptibility of bare graphene to ambient conditions, significant variations in the electronic properties of the sample are observed, which are subsequently stabilized following the encapsulation process. The values reported for CF_3SO_3Li correspond to the gate voltage being fixed at $n = 5 \times 10^{11}$ cm^{-2}.

Properties	Bare	PMMA	F4TCNQ	CF_3SO_3Li
n (10^{12}/cm^2)	0.4-2.2	7	0.42	0.4
R_{sheet} ($\Omega/\square$)	4700-1700	1336	7716	6900
μ (cm^2/Vs)	3200-1668	744	1531	1560
R_H (Ω/T)	4733-283	99	1181	1024

Table 6.2: Epitaxial graphene electrical properties in different encapsulations

Properties	1 µm	10 µm	100 µm	1000 µm	Mean ± SD
n (10^{12}/cm^2)	7.1	7.2	4.9	6.6	6.45 ± 0.78
R_{sheet} ($\Omega/\square$)	1261	1365	1366	1144	1336.4 ± 40.24
µ (cm^2/Vs)	698	632	931	829	744.8 ± 91.31
R_H (Ω/T)	88	86	127	95	99.15 ± 14

Table 6.3: Electrical characterization of PMMA encapsulated sample for different sizes

6.6 Comparison of noise for different device sizes

Figure 6.8 validates the expected geometric scaling of noise outlined by Hooge's law across devices of various sizes, spanning an area range from $A = 1$ to 10^6 µm^2. In conjunction with Hooge's law, the noise PSD dependence over device geometry is depicted as $S_V \propto 1/l^2$. In Figure 6.8(a), noise PSD measurements are presented for diverse PMMA-passivated epigraphene devices, with $l = w$ varying from 1 to 1000 µm. All devices are characterized in terms of sheet resistance, carrier density, and carrier mobility, as indicated in Table 6.3 with mean ± standard deviation values. As illustrated in Figure 6.8(b), the noise PSD variation is $\propto a \times l^{-2}$ (where l is in units of µm), with the fitting coefficient a ranging from 3 to $5{\times}10^{-10}$ (µm^2/Hz). Moreover, Figure 6.8(c) offers a comparison of the PSD observed in large epigraphene devices with the noise reported for other types of graphene, including exfoliated graphene,

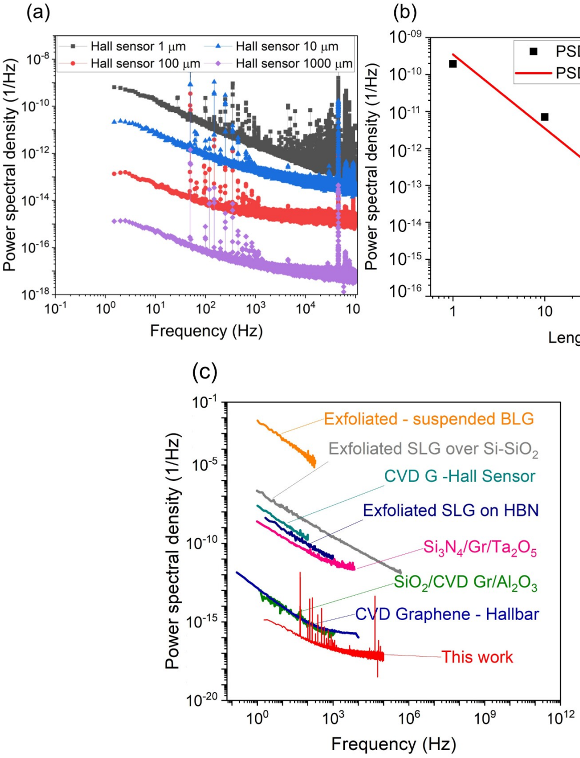

Figure 6.8: The Power Spectral Density (PSD) of noise was examined at 10 Hz across device widths ranging from 1 to 1000 μm. Panel (a) illustrates the noise PSD within a bandwidth of 2 to 100 KHz for different device widths. Panel (b) demonstrates the noise PSD measured at 10 Hz, showcasing the noise PSD's reliance on the device's area. Panel (c) presents a comparison of the noise PSD of epitaxial graphene with historical data from various graphene devices, indicating that the observed noise in epitaxial graphene is significantly lower, by an order, than previously reported values [79]–[85].

CVD-grown graphene, as well as graphene encapsulated by materials such as hBN, Ta_2O_5, and Al_2O_3. Notably, the noise PSD observed in our epigraphene devices is considerably lower when contrasted with previously reported values in various graphene-based devices obtained from different sources.

6.7 Conclusions

In summary, PMMA,F4TCNQ and CF_3SO_3Li encapsulations are employed to explore the potential of epigraphene Hall sensors. This method facilitated the consistent fabrication of high-quality, low-noise sensors with a wide range of carrier densities. Results indicate that doped epigraphene Hall sensors with low carrier densities exhibited impressive performance at room temperature, with sensitivities of $S_I = 1442$ V/AT and $S_V = 0.23$ V/VT, along with a record-breaking low detection limit of $B_{MIN} = 27$ nT/$\sqrt{\text{Hz}}$ at 20 KHz. Thermal testing of the doped Hall sensors revealed their thermal stability, with a temperature coefficient of $\Delta_T = 0.03$ %/°C up to 150 °C. Even at 150 °C, the sensors maintained commendable performance, displaying $S_I \approx 300$ V/AT, $S_V \approx 0.12$ V/VT, and a detection limit of $B_{MIN} \approx 100$ nT/$\sqrt{\text{Hz}}$.

Although conventional III-IV type sensors currently outperform epigraphene Hall sensors at room temperature in terms of detection limit, their efficacy diminishes rapidly at high temperatures. In contrast, the thermally cured epigraphene chips displayed promising performance even at 150 °C (refer **Paper B**), surpassing many commercially available sensors. However, the current doping method presents a significant limitation, particularly its unsuitability for high temperatures. Future advancements hinge on the development of a new doping scheme, an innovative encapsulation approach, or possibly both. The ultimate objective is to maintain low and stable carrier density in doped epigraphene Hall sensors, even under elevated temperature conditions.

These doped epigraphene Hall sensors exhibited the lowest detection limits among various graphene-based sensors documented in the literature and demonstrated minimal device noise levels. The fabrication techniques proved to be reliable, ensuring excellent contact resistances and uniform doping. Moreover, this study indicates that employing large-area devices can substantially reduce the noise parameter by orders of magnitude. Furthermore, it is demonstrated that the assembly of these Hall sensors can potentially decrease the effective detection limit by approximately $1/\sqrt{k}$, where k represents the quantity of interconnected Hall sensors. This development presents a positive prospect for utilizing epigraphene-based Hall sensors to encompass magnetic field sensitivities ranging from 10^{-12} T to 10^{-15} T. Currently, achieving such sensitivities demands intricate and costly technologies, such as flux gate magnetometers and Superconducting Quantum Interference Device (SQUID) magnetometers.

CHAPTER 7

Quantum Hall Array Resistance Standard

Quantum Hall resistance metrology deals with the definition and precise measurement of the unit of resistance Ohm (Ω), down to part-per-billion accuracy. The redefinition of SI system in 2019 derives every base unit from the seven fundamental constants, such as Planck's constant h and elementary charge e. The Quantum Hall Effect (QHE) observed in epigraphene establishes a precise relationship between resistance and fundamental constants $R = R_K/(4(N+1/2))$, where $R_K = h/e^2 \approx 25.8$ kΩ (von Klitzing constant) and an integer $N \geq 0$.

Graphene has a large spacing between its 0^{th} and 1^{st} Landau Level (LL). As a consequence, the QHE can be observed at relaxed experimental conditions with higher temperatures T, lower magnetic flux densities B, and higher bias currents I compared to traditional systems where dissipation occurs easier[86]. The $N = 0$ plateau is not only the most robust but also the most well-quantized and is therefore preferred for precision metrology.

The QHE in epigraphene can also serve beyond resistance calibration, for the realization of kilogram via the Kibble balance, which is an instrument that measures the weight of an object by balancing the gravitational force with a compensating electromagnetic force, defined using h via the QHE and the ac Josephson effect. To include QHE in the Kibble balance requires a device with 100 Ω resistance and I_C on the order of 10 mA. Due to this QHAs is the ideal and practical solution since a single graphene Hall bar (HB) can in practice only achieve $R = R_K/2$ and $I_C \sim 100$ µA at typical operating conditions.

This chapter explains the method to fabricate Quantum Hall Array (QHA) (refer **Paper D**), presents experimental findings on the quantization accuracy of a 236-element QHA, demonstrating $R_K/236 \approx 109\ \Omega$ with 0.2 part-per-billion (nΩ/Ω) accuracy with $I_C \geq 5$ mA ($\sim$ nΩ/Ω accuracy for $I_C = 8.5$ mA), utilizing epitaxial graphene on silicon carbide (epigraphene). The accuracy of the array, akin to the most precise universality tests of QHE, combined with the scalability and dependability of this approach, lays the foundation for broader applications of graphene in the new SI and beyond. The study made in **Paper E** examines the extended stability of epigraphene Quantum Hall Resistance Standard (QHRS) and Quantum Hall Array Resistance standard (QHARS), emphasizing the use of chemical doping via molecular dopants to achieve uniform doping and control over carrier density. The research focuses on identifying uncomplicated storage methods that ensure extended stability without requiring complex laboratory facilities. The results suggest that an oxygen absorber/desiccant mixture could enable straightforward and robust long-term storage of polymer-encapsulated molecular-doped epigraphene quantum Hall standards, thereby addressing a crucial barrier to their widespread adoption in practical metrology.

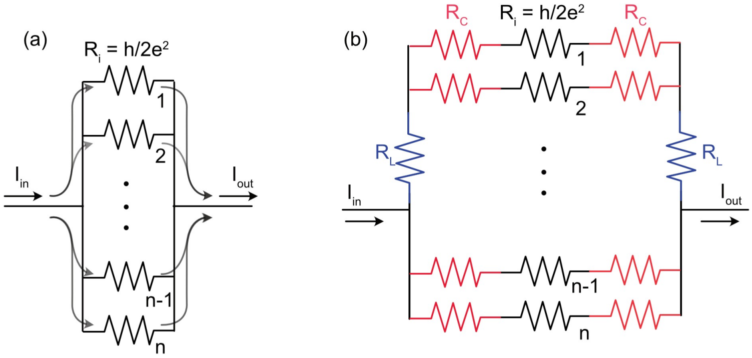

Figure 7.1: (a) Parallel combination of quantum Hall arrays. Current I_{in} is split between n elements to reduce the current received by individual Hall bars. (b) Simple resistive model for quantum Hall array.

7.1 The array concept

The demand for large current by Kibble balance is fulfilled by splitting the current between the parallel branches. In an array consisting of n Hall elements, supplied current I_{in} is divided between individual elements by I_{in}/n, thereby preventing them from breaking their quantized state. This will also achieve the goal of reducing the total resistance from $R_K/2$ to $R_K/2n$. It is also possible to construct decadic values of QHARS by a complex combination of series and parallel resistive network [87]. By controlling the number of elements in a resistive network one can tune the total resistance to the required value in the Kibble balance. The drawback of such a system is the additional resistance added on top of $R_K/2n$ by the contact resistances of each element $2 \times R_C$ and the line resistance R_L from the metal used for the fabrication of the array. This will compromise the accuracy of the QHARS.

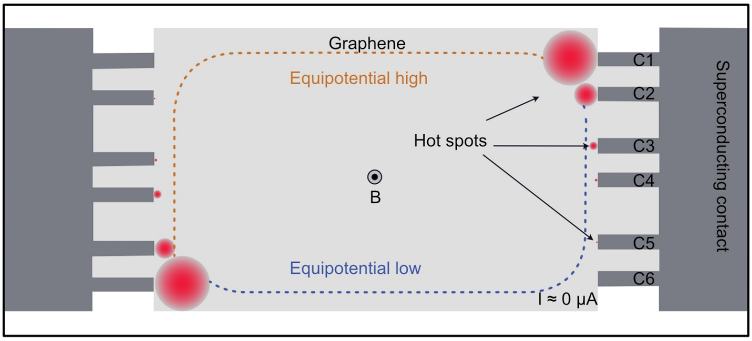

Figure 7.2: Schematic of a Hall element in two probe configurations under quantum Hall regime. The red spots are charge carrier injection points (also known as hot spots) from the contacts to the edge channels [88]. The size of the hot spot reduces significantly from contact finger $C1$ to $C6$, indicating a dramatic reduction of current injection at $C6 \approx 0$ μA.

Line resistance R_L can be eliminated by utilizing superconducting metals with $T_C > 5$T. Since graphene can be quantized well below this magnetic field, it will prevent the superconductor from transitioning back to normal metal. To reduce the contact resistance of each Hall element, contacts are designed with multiple fingers named $C1, C2.., C6$ as shown in the figure 7.2. From the Delahaye's triple series connection [89] for quantum Hall devices in the quantum Hall state, current in each finger progressively reduces by the factor $\epsilon/2 = (R_C/R_H)/2$. Even if the contact resistance is of the order of $\approx 100\ \Omega$, a three-finger geometry will effectively reduce the contact resistance to 100 μΩ or less [90]. The vanishing resistance is because the majority of the current flows through the first finger, with diminishing current in subsequent fingers, each decreasing less than the one before it. Consequently, as one approaches the last finger, the voltage drop has already nearly reached zero. This process leads the superconductor to attain the potential of the quantized 2D electron gas. In order for each finger to serve as an individual charge reservoir in the quantum Hall regime, a minimum separation greater than the inelastic scattering length of charge carriers must be maintained between them [91].

7.2 Array fabrication

Figure 7.3(a) illustrates the utilization of epigraphene in the fabrication of QHAs (Chip A). The contact deposition employs the edge contact fabrication technique, which is further detailed in section 3.1. Here, 120 nm thick NbN is sputter deposited in a magnetron system, with the sample stage kept at room temperature. The sample is then immediately transferred to an electron beam evaporator to deposit a 20 nm protective layer of Pt to prevent degradation of the NbN-film. Doping regulation is achieved through the use of molecular dopants [61]. This ensures a stable, homogenous, and controllable doping over the whole chip, with an expected charge inhomogeneity of doped graphene below 10^{10} cm^{-2}. Using thermal annealing at 160 °C to tune the carrier density, we aimed to achieve a carrier density on the order of 10^{11} cm^{-2} which is suitable for quantum Hall measurements around 2 K and 5 T [49]. In (b), the schematic representation of the array organization reveals the presence of two subarrays, each containing 118 Hall elements operating in parallel, resulting in a total of 236 Hall bars. These two subarrays are interlinked in a series. According to QHE principles, individual Hall bars are quantized to the value $R_i = h/2e^2$. Consequently, the total resistance of one subarray becomes $h/(2 \times 118e^2) \approx 109\ \Omega$ at $N = 0$ plateau. The number 118 for each subarray, and the unusual resistance value of $h/(236e^2)$ was chosen because its ratio to 100 Ω is very close to 70/64, which is compatible with the winding ratios in the Cryogenic Current Comparator (CCC) [92] (refer Appendix A). The magnified transmission mode optical microscopy image of the array is shown in (c). Hall bars are circular in order to achieve a symmetrical design with high packing density. To maximize I_C, the diameter was chosen to be 150 μm so that the minimum distance the QHE edge state needs to travel between the two source-drain contacts is approximately a quarter of the circumference, exceeds the equilibration length of the edge state, which is on the order of 100 μm at 5 T and 2 K [93]. By implementing multiterminal connections, the impact of contact resistance is minimized. Additionally, the choice of superconducting NbN as the contact metal effectively eliminates any influence from lead resistance, owing to its high critical magnetic field and critical temperature [94]. The film is sputter deposited and is dimensioned to be at least 120 nm thick and 50 μm wide to support currents on the order of 10 mA at 5 T and 2 K [95]. A 200 μm wide Hall bar with NbN contacts is fabricated on the same chip as the QHARS. This Hall bar is used for characterizing the array which is further explained in this chapter.

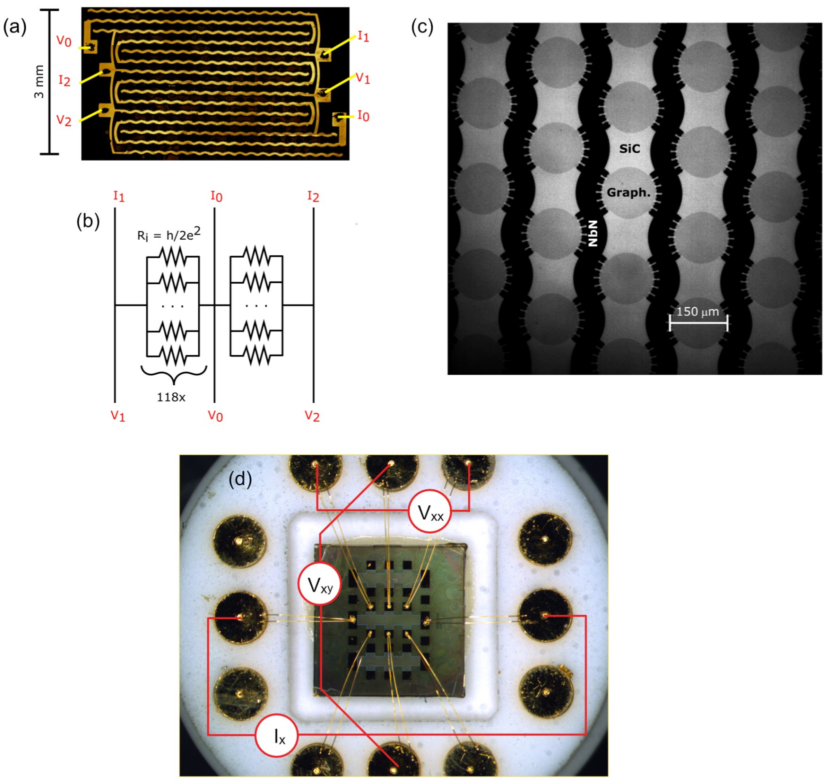

Figure 7.3: (a) The image represents a composite micrograph in false colors of the entire array, comprising two subarrays connected in series, with each subarray hosting 118 Hall bars in parallel, resulting in a total of 236 Hall bars. (b) The array is schematically represented, wherein each subarray in the quantum Hall regime can be illustrated by 118 parallel resistors, each possessing a resistance of $R_i = h/(2e^2)$. Here, h represents Planck's constant, and e stands for elementary charge. The complete array consists of two subarrays connected in series. (c) A magnified transmission mode micrograph of the individual circular epigraphene Hall bars is shown. These bars are connected in a simple two-probe configuration using NbN split contacts with six prongs. The substrate (SiC) is also visible. Each element in the array is topologically equivalent to a standard rectangular Hall bar wired in the multiple-connection configuration. (d) Optical image of an epigraphene QHRS chip (7 mm × 7 mm), with three Hall bar devices. The chip is glued to a TO-8 holder, and the center Hall bar is wire bonded to the holder using Al/Si wires.

Figure 7.3(d) shows simple Hall bars fabricated on a different chip (Chip B). These epigraphene-based Hall bars with molecular dopants for carrier control serve as an excellent candidate for primary resistance standards (QHRS). Stability tests are made on QHARS (Figure 7.3(a)) and a total of eight QHRSs, with four produced on graphene grown on high-purity semi-insulating SiC (HPSI, Cree now Wolfspeed®) and four on semi-insulating compensated SiC (Atecom tech. Ltd) (Chip B to I). Despite this variation, all chips were crafted into identical devices, employing the same Hall bar configurations, and doped using the identical molecular doping technique. The fabrication procedure largely adhered to the guidelines outlined in previous works [17], [96]. For the contacts Ti/Au metals are used, ensuring minimal contact resistance to the graphene material, as detailed in section 3.1. Following the chemical doping process, we employed additional thermal annealing at 160 °C to adjust all carrier densities to approximately $1-2\times10^{11}$ cm^{-2} (n-type). This carrier density level was deemed optimal for precision measurements conducted within our typical parameters of $T = 2$ K, $B = 5$ T, $I = 23$ µA [49]. The supplementary annealing procedure lasted approximately 30 minutes for Cree substrates and over 60 minutes for Atecom. The variance in annealing duration was attributed to differing substrate-induced doping effects.

7.3 Direct and indirect comparison measurements

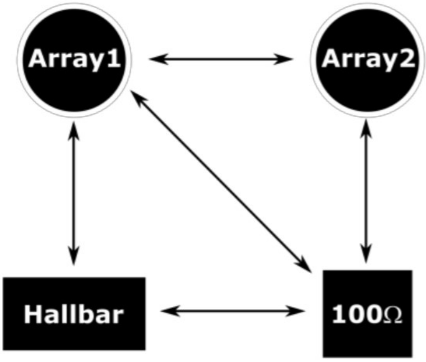

Figure 7.4: Overview of comparative measurements. The arrows within the diagram illustrate direct comparisons among various resistance standards.

Figure 7.4 shows the systematic way to investigate the accuracy of fabricated QHAs. Before the comparison measurements, devices on Chip A are characterized independently to validate their respective magnetotransport behaviors. Once the devices satisfy their expected quantized resistance (R_{XY}) values, as shown in the Figure 7.5, possible ways of direct comparisons between devices are performed using a Cryogenic Current Comparator (CCC) system. A measurement between Array 1 and Array 2 will be considered a direct comparison and to validate the direct subarray comparison measurements, indirect comparisons between the arrays are performed. These direct and indirect assessments are pivotal not only to affirm the accuracy of subarray quantization but also to establish a connection between our measurements and traditional quantum Hall experiments [97]. For instance, both Array 1 and Array 2 are compared against another standard, such as a 100 Ω resistor, as illustrated in Figure 7.4. The indirect comparison is calculated as $\Delta_{Array1-Array2} = \Delta_{Array1-100} - \Delta_{Array2-100}$. If the direct and indirect comparisons align, it solidifies that the subarrays are perfectly quantized, exhibiting no noticeable deviation from their designated resistance values.

7.4 Comparison between subarrays

Comparisons made between the array and the Hall bar are situated on the same chip A, enabling measurements to be conducted within the same cryostat and using identical setups. This close proximity of the devices significantly diminishes external influences arising from excessive wiring. Furthermore, the direct one-to-one comparison between the subarrays serves to further diminish any uncertainties and errors in the precision measurements. To simultaneously test the subarrays, a direct comparison of their quantized resistances was executed utilizing a CCC system. The CCC system is a widely recognized method for measuring resistance ratios with the utmost precision, as explained in Appendix A.

Figure 7.6 presents the primary outcomes of the subarray comparison, depicting the average relative deviation of the direct subarray comparison, revealing that the resistance of each subarray coincides within 0.2 nΩ/Ω. Demonstrated in Figure 7.6(a) is an illustration of a precision comparison measurement between the two subarrays. Each complete set of measurements comprises multiple readings via the CCC, with each reading requiring 20 minutes and incorporating multiple shifts in current polarity to compensate for thermal voltages and short-term drift. The data points shown in Figure 7.6(b) are the weighted averages of these measurement sets taken at various magnetic flux densities, with the standard deviation of each reading used as a weight in the final mean calculation. The error bars depicted in Figure 7.6(b) denote the standard deviation of the mean for each set of measurements, constrained by Allan deviation at 10^4 s. It is important to note that all uncertainties in this study are presented with a unity coverage factor ($k = 1$) unless stated otherwise. Allan deviation analysis is utilized to characterize the nature of the noise present in the

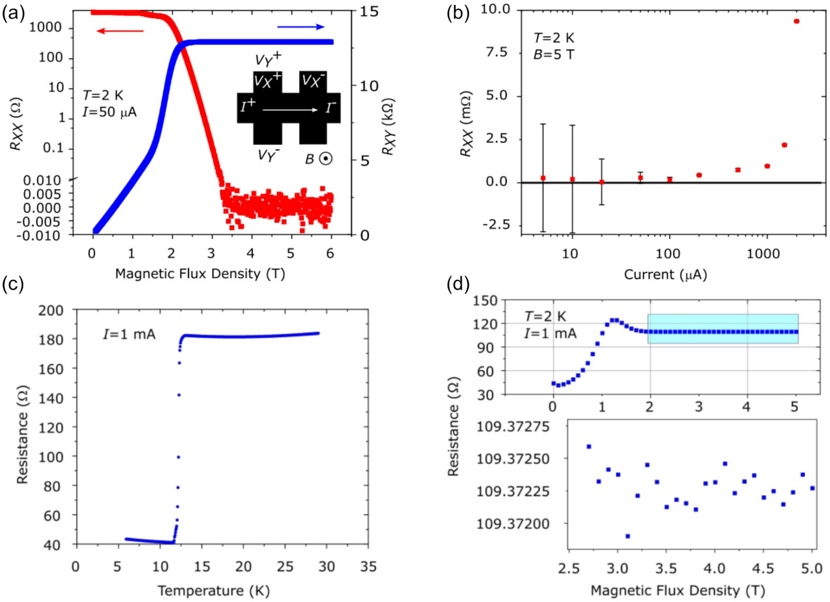

Figure 7.5: (a) Longitudinal resistance R_{XX} (red) and transverse resistance R_{XY} (blue) are measured using a distinct Hall bar (Chip A) with a standard rectangular geometry. The inset illustrates the Hall bar configuration for measurements. (b) Breakdown current, assessed on the Hall bar, exhibits no notable increase in R_{XX} up to a 100 μA bias. Error bars represent one standard deviation. (c) Depicts the superconducting transition of the NbN-contacts (critical temperature $T_C = 12$ K) measured for a single subarray. The increase in resistance post the superconducting phase transition is attributed to quantum effects in epigraphene. (d) Illustrates the magnetotransport characterization of the same subarray, displaying complete quantization after reaching 3 T. This indicates comparable carrier density and mobility between the Hall bar and the array. The 4 mΩ (4 μV) offset from the quantized resistance $h/(236e^2)$, where h is Planck's constant and e elementary charge, arises due to voltmeter error.

measurements [98]. A noticeable trend observed is a gradual decrease with elapsed measurement time τ, following an approximate $\sim 1/\tau^{1/2}$ relation (Figure 7.6(c)), indicating that white noise prevails as the dominant type. However, this trend is interrupted at longer time scales as other sources of noise, such as slow temperature drift and $1/f$ type noise, begin to take precedence, suggesting that additional

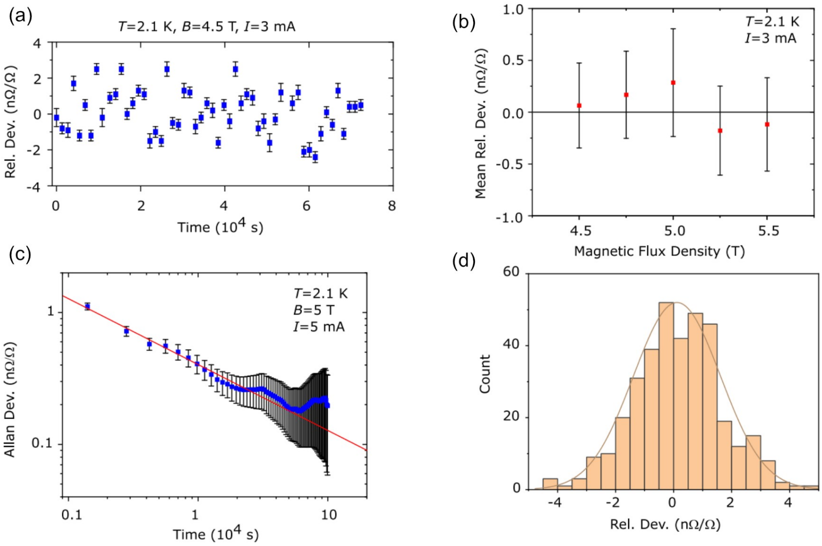

Figure 7.6: (a) Precise Cryogenic Current Comparator (CCC) measurements were made to compare the subarrays, demonstrating their relative deviation at a specific magnetic flux density. This assessment encompassed 53 CCC readings, each lasting approximately 20 minutes. The error bars, serving as weights in the final weighted mean, were indicative of a deviation of 0.06 nΩ/Ω. (b) Precise evaluations carried out at varying magnetic flux densities highlighted the mean relative deviation between the two subarrays. Each data point represented the weighted mean of more than 45 CCC-readings akin to those in (a), with the accompanying error bars representing one standard deviation derived from Allan deviation at 10^4 s (refer to (c)). These measurements underscored the minimal deviation observed across the range of measured flux densities. (c) The Allan deviation followed a $1/\tau^{1/2}$ trend (red line), where τ represented the elapsed measurement time, signifying the dominance of white noise and the consequent limitation of the measurement uncertainty to 0.2 nΩ/Ω. (d) A histogram of the data that contributed to the means in (b) was presented, illustrating the normal distribution. The solid line represented a Gaussian fit, confirming that the unweighted mean rested around 0.1 nΩ/Ω.

Material	Hall bars	Nominal Res. ($R_K = h/e^2$)	Nominal Res. (kΩ)	Relative Deviation (nΩ/Ω)	Meas. Uncer. k=1 (nΩ/Ω)	Current (mA)	Temp. (K)	Magnetic Flux Dens. (T)
GaAs [102]	100	1/200	∼0.129	0.1	2	2	1.3	8.4-9
GaAs [105]	88	5075/131	∼1000	20	8.5	0.001	1.5	9-10
GaAs [106]	10	5	∼129	2.5	12.7	0.005	0.3-1	8-9
Graphene [103]	100	1/200	∼0.129	10^7	10^5	0.1	2	7-9
Graphene [100]	6	2/6	∼8.60	1.9	0.75	0.15	1.7	9
Graphene [107]	10	5	∼129	10	20	0.5	4	6
Graphene [104]	13	1/26	∼0.993	0.45	3	0.3	1.6	7.5-9
Graphene (This work)	236	1/236	∼0.109	0.03	0.2	5	2.1	5
Graphene (This work)	236	1/236	∼0.109	0.5	0.5	8.5	2.1	4.25

Table 7.1: The provided table encompasses earlier findings on Quantum Hall Arrays (QHAs), incorporating conventional GaAs techniques alongside contemporary graphene methods. The table columns detail the material, the count of individual Hall bars, the assumed array resistance, the deviation from the anticipated value, the uncertainty in measurement, the applied measurement current, the temperature, and the range of magnetic flux density. The outcomes of this study are depicted in the final two rows, featuring two subarrays, each comprising 118 individual Hall bars, leading to a total of 236 elements for the entire array.

time averaging may not necessarily enhance the final measurement uncertainty. The practical minimum measured uncertainty for the standard deviation of the mean in our experiments, in the limit of white noise, is 0.2 nΩ/Ω. Furthermore, a histogram (Figure 7.6(d)) demonstrates that the data utilized in the aforementioned analysis are distributed normally, further affirming the dominance of white noise.

The computed weighted mean of the mean relative deviations $\Delta_{Array1-Array2}$ at various flux densities in Figure 7.6(b) offers insights into the extent of quantization [99]–[101]. Utilizing the respective standard deviation of the mean as weights, the resultant weighted mean relative deviation and the standard deviation of the weighted mean amount to $\Delta_{Array1-Array2} = (0.033 \pm 0.082)$ nΩ/Ω. This level of reproducibility in the quantization of such a large QHA is unparalleled for both GaAs [102] and graphene [103], [104], significantly undershooting the 1 nΩ/Ω precision metrology requirement [97]. The exceptional agreement between the resistances of our subarrays can be reasonably attributed solely to precise resistance quantization, particularly as the subarrays, although ostensibly identical, are expected to exhibit marginally distinct non-quantized resistance due to finite doping discrepancies. Table 7.1 shows a comparison between the results obtained in this thesis and other reports on arrays in literature.

The summary of direct and indirect comparisons made for Hall bar and Hall arrays (Chip A) is shown in Figure 7.7. An indirect comparison between subarrays

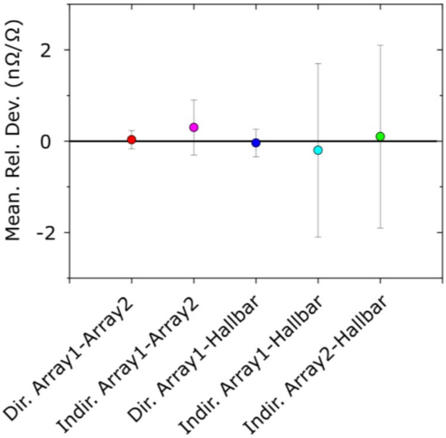

Figure 7.7: Both direct and indirect comparisons for the subarrays show no significant deviation. The error bars are one standard deviation of the mean, limited by Allan deviation measurements.

of $\Delta_{Array1-100} - \Delta_{Array2-100} = \Delta_{Array1-Array2} = (0.3 \pm 0.6\ \mathrm{n}\Omega/\Omega)$, which aligned well with the direct array comparison. The weighted mean of all such comparisons is $\Delta_{Total} = (0.03 \pm 0.04)\ \mathrm{n}\Omega/\Omega$, which is zero within the uncertainty. The consistency of the comparison measurements can be checked by looking at the three closed comparison loops (Figure 7.4(a)). Inside each loop, the relative deviations should sum to zero. For instance, $\Delta_{Array1-Array} + \Delta_{Array2-100} + \Delta_{100-Array1} = \Delta_{Array1-Array2} + \Delta_{Array2-100} - \Delta_{Array1-100} = (0.033 \pm 0.62)\ \mathrm{n}\Omega/\Omega$, which is zero within the expanded measurement uncertainty.

7.5 High bias current measurements

Lastly, performance boundaries of the arrays with regard to bias current, aiming to determine the threshold at which the QHE deteriorates were investigated. With an increase in the bias current, it is observed that deviations around 1 nΩ/Ω were feasible at currents up to 10 mA and magnetic flux densities of 5 T (Figure 7.8). The quantization at elevated bias currents was assessed through precision measurements at different flux densities (Figure 7.8(b)). The apparent magnetic flux density dependency indicates that the critical current (I_C) has reached its limit for epigraphene (imperfect quantization), NbN contacts (resistive state), or a combination of both, as I_C can potentially improve at lower flux densities for either case [49], [95]. The

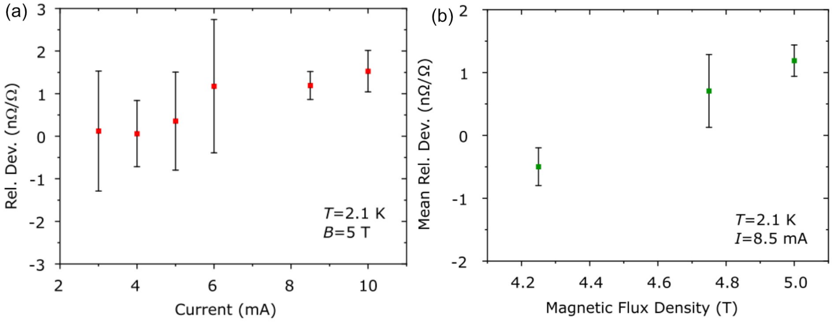

Figure 7.8: High bias current measurements on arrays. (a) Precision CCC measurements using direct comparisons between subarrays demonstrate no significant deviation until 8.5 mA. The data comprises the mean of 5-10 measurements, each lasting 20 minutes, with error bars representing one standard deviation. (b) Mean relative deviation between subarrays for different magnetic fields. The error bars signify one standard deviation of the mean, as derived from the Allan deviation at 10^4 s. Notably, a significant deviation is observed at 5 T, which converges into the measurement uncertainty (k = 2) at lower flux densities.

deviation at 8.5 mA remains within 1 nΩ/Ω at lower magnetic flux densities < 5 T, which is satisfactory for most practical metrological applications [96], [97], including the Kibble balance [108]. It is important to note that the fabrication techniques employed in this study permit further enhancements in performance. The observed I_C is still significantly distant from any fundamental material limit and is primarily constrained by the current device design. As the NbN leads can be easily expanded (e.g., thicker film), the breakdown current of the QHA is ultimately restricted by the single graphene Hall bar I_C, which can be substantially higher than the approximately 85 µA of current flowing through each individual array element at 10 mA. By adjusting the carrier density to a higher value [27], it should be feasible to achieve an array with $I_C > 10$ mA and reliable quantization at 2 K and 5 T [96], with the potential for even higher I_C under alternative operating conditions [99].

7.6 Stability of Quantum Hall Resistance Standard

As shown in Figure 7.9 four different storage methods were tested for each substrate type for QHRSs spread across the chips B to I, resulting in eight devices distributed across eight containers. The relative change of carrier density n over time t serves as the primary stability indicator denoted as $(n(t) - n_0)/n_0$, where n_0 is the initial carrier density and $n(t)$ is the carrier density at a specific time. Determining the

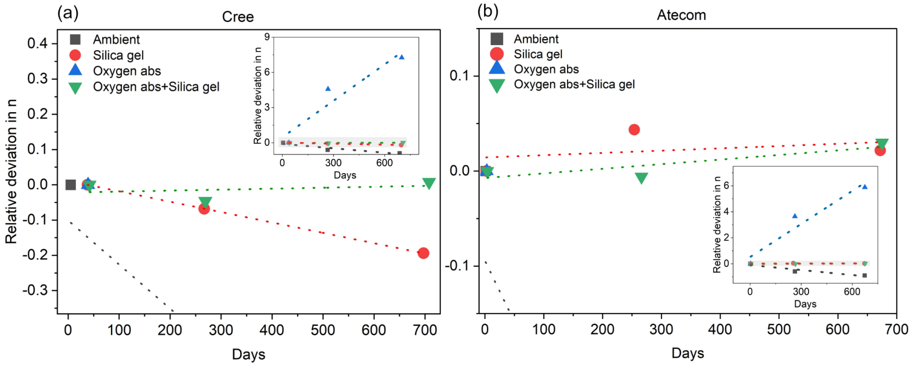

Figure 7.9: Measurement of the relative deviation in carrier concentration n of chemically doped epitaxial graphene samples stored in various environments over a two-year period is depicted. (a) represents a close-up (shaded) view of the inset in the top right corner for the Cree sample. The sample stored in an environment combining an oxygen absorber and silica gel displays notably high stability over the 700-day duration, surpassing other storage methods. (b) exhibits an enlarged (shaded) portion of the inset in the bottom right corner for the Atecom sample. This sample exhibits robust stability not only within the environment of the oxygen absorber and silica gel mixture but also in the silica gel environment alone. Error bars are omitted in the plot, as the data marker size accounts for approximately one standard deviation.

carrier density involved measuring the Hall voltage V_{XY} while sweeping the magnetic flux density B using 0.1 T steps. A linear regression fit was employed in the low-field linear regime to compute the Hall coefficient R_H (in units of Ω/T). The carrier density was then obtained as $n = 1/(eR_H)$, with e representing the elementary charge. Hall measurements were conducted at a temperature of $T = 2$ K with a bias current of $I = 23$ µA in a dry cryostat (Teslatron).

Figure 7.9 provides an overview of the carrier density measurements performed across all samples, spanning a duration of approximately 700 days. Extended storage led to significant changes in carrier densities for samples stored in ambient conditions or with the oxygen absorber. These carrier densities were either too low (around 10^{10} cm^{-2}) or too high (approximately 10^{12} cm^{-2}) for accurate quantization under typical operating conditions of 2 K, 5 T, and 23 µA bias. Consequently, these storage techniques are deemed unsuitable for long-term storage. Samples stored in silica gel exhibited signs of drift, particularly noticeable in the case of the Cree sample. While the drift was significant, the samples could still be utilized for precision measurements within our usual operating conditions for an extended period. For the

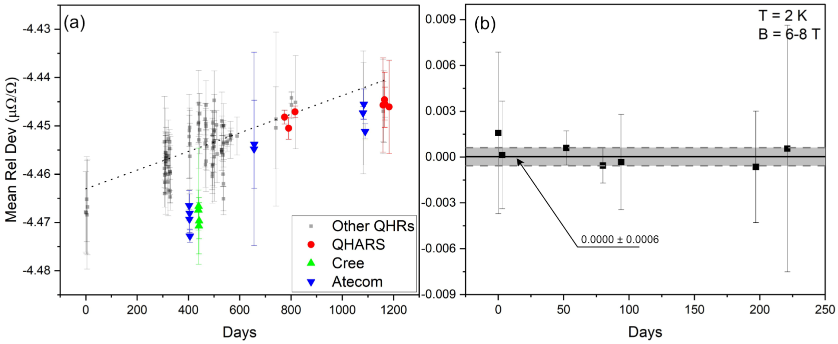

Figure 7.10: (a) Precision Cryogenic Current Comparator (CCC) measurements of a 100 Ω resistance standard compared against various Quantum Hall Resistance Standard (QHRS). These comparison measurements were conducted against different graphene QHRSs (‘Other QHR’), Quantum Hall Array Resistance standards (QHARSs), as well as the Cree and Atecom samples discussed in this study. The slope of the mean relative deviation between the 100 Ω standard and the various QHRSs over a three-year period suggests that the drift in the 100 Ω resistor amounts to approximately 2 nΩ/Ω per 100 days. The error bars represent one standard deviation. (b) Shows the precision measurements directly comparing graphene quantum Hall arrays stored in a desiccant/oxygen absorber environment. The grey-shaded area represents one standard deviation from the weighted mean (black line) of all data points. The mean relative deviation among the QHARSs is within 0.03 nΩ/Ω with an uncertainty of 0.6 nΩ/Ω.

Atecom sample, the overall drift seemed low, but there was considerable variation between the measurements, suggesting some degree of instability. Despite the relatively steady trend in the Cree case, the silica gel storage method was functional but not ideal.

The most stable storage solution involved a combination of oxygen absorber and desiccant. In both instances, the drift appeared minimal, with a gradual increase in n-doping over time. The relative change in carrier density per day was approximately $(0.0027 \pm 0.0082)\%$ for Cree and $(0.0048 \pm 0.0029)\%$ for Atecom. All errors in this study are reported with a coverage factor of one (k = 1), unless stated otherwise. This level of stability compares favorably with the current best storage method in a nitrogen environment, exhibiting a relative drift of 0.02 % per day [96].

7.7 Precise stability analysis

As a final evaluation, QHARSs, shown in Figure 7.3(a), with an array resistance close to 109 Ω, consisting of 236 interconnected Hall bars is employed. These arrays were stored in a similar desiccant/oxygen absorber environment, allowing for more precise comparison measurements with the 100 Ω standard (depicted as red data in Figure 7.10(a)), thereby providing additional evidence of the long-term stability of the quantization accuracy of the sample stored in the mixed desiccant/oxygen absorber environment. Furthermore, the arrays are used to directly compare between quantum standards. The group of data labeled as 'Other QHRSs' represents comparison measurements of the 100 Ω standard against various QHRSs not explicitly discussed in this work, and they were not all stored in a controlled environment. This data set enabled the observation of the long-term drift of the 100 Ω standard. Figure 7.10(b) demonstrates a direct comparison measurement between two QHARSs (on the same chip) following long-term storage in a mixed environment. Due to the direct comparison between arrays with a 1:1 ratio, the noise in this type of measurement was minimal, and the uncertainty could reach 0.1 nΩ/Ω with sufficient averaging [109]. The resistance value of the QHARSs exhibited no inherent drift, therefore any discrepancy in quantization could be attributed to sample degradation. The data revealed that the relative deviation between the QHARSs remained within the noise level of 0.6 nΩ/Ω for over 225 days and ongoing. Thus, there is no discernible degradation of the quantization accuracy at the sub-part-per-billion level for samples stored in a mixture of oxygen absorber and desiccant.

7.8 Conclusion

In this chapter, the precision quantization of a graphene QHA composed of 236 Hall bars was demonstrated to be 0.2 nΩ/Ω, validated through traditional comparisons to a single Hall bar device. Robust fabrication of such an accurate array hinges on crucial enabling technologies, including uniform molecular doping and the establishment of low-contact resistance superconducting leads across all array elements. The research highlights the potential for large bias current operations, up to 5 mA and beyond, while affirming the necessity for novel array-specific quantization tests to complement existing single-hall bar examinations.

The proposed method of direct comparison between subarrays is suggested for inclusion in future practical metrological guidelines, particularly as the quantum metrology landscape continues to embrace epigraphene-based devices. To further enhance the understanding of array behavior and performance, the implementation of non-unity ratio comparisons and redundancy-based connections in array designs is recommended. These measures can effectively uncover potential errors and strengthen the reliability of the array quantization process.

Embracing the use of array devices can significantly contribute to advancing the realizations of crucial units such as the ohm, ampere, and kilogram, further integrating the QHE into the fabric of modern metrology. The findings of this study are expected to encourage continued exploration in this field, fostering future developments and promoting inter-laboratory comparisons, ultimately solidifying graphene arrays as a fundamental resistance standard.

This chapter also examined four different cost-effective storage solutions and their impact on the transport properties of polymer-encapsulated molecular-doped graphene over a period of 700 days. From the findings, one could conclude that a combination of oxygen absorber and desiccant presents a dependable and highly stable storage solution for epitaxial graphene QHRS and QHARS, offering an easily implementable option for situations requiring low maintenance and long-term sample stability. The stability observed is on par with the current nitrogen atmosphere-based storage techniques. The proposed storage method, utilizing a desiccant/oxygen absorber mixture in a sealed glass bottle, provides a straightforward and practical alternative that is widely accessible.

Further research is necessary to comprehensively grasp the interactions between the storage chemicals, molecular dopants, and substrate types, which would contribute to a deeper understanding of the principles underlying the stability of the electronic properties of graphene devices. Such investigations could facilitate the optimization of simple storage techniques, enabling graphene Quantum Hall Resistance Standards to achieve long-term stability comparable to GaAs-based systems.

CHAPTER 8

Summary and outlook

8.1 Summary

This thesis describes advancement in graphene growth and its use for several practical devices. Optimization of the epitaxial growth to obtain large-scale, high-quality monolayer (ML) graphene, served as a platform to further progress in developing technologies that helped gain access to the tremendous properties of this 2D material. The persistent challenge of controlling epigraphene's carrier density has hindered systematic investigations into the performance of epigraphene-based Hall sensors. This challenge was addressed using a molecular doping technique and put to test in these devices. The devised tri-layer technique circumvents the necessity for graphene/hBN heterostructures for creating edge contacts, leading to high success rates and consistent attainment of low contact resistance and it plays a crucial role in achieving low noise performance in practical electronic devices. All of these developments helped to overcome a critical obstacle that previously hindered the comprehensive exploration of the distinctive characteristics of graphene, marking a significant step forward toward its integration. The implementation of scalable solutions has facilitated in-depth investigations into magnetotransport, and low-frequency noise performance in epigraphene, consequently shedding light on the functionalities of Hall sensors, and quantum Hall arrays.

The emphasis on Hall sensors utilizing epigraphene highlights the exceptional performance and sensitivities achieved at room temperature, showcasing the potential of epigraphene-based sensors. Compared to state-of-the-art graphite-gated and metal-gated graphene Hall sensors, the developed epigraphene Hall sensors demonstrate superior performance even at room temperature measurements. The implementation of a cross-correlated noise spectrum analyzer, as outlined in this thesis, facilitated precise noise performance analysis of these Hall sensors across various encapsulations and sizes. Leveraging the availability of large-scale ML epigraphene, we successfully produced millimeter-sized Hall sensors, demonstrating adherence to Hooge's law and resulting in the lowest recorded noise levels in graphene-based devices within the existing literature.

The scalable growth of graphene, the edge contact fabrication technique, and previously established molecular doping methods in this thesis collectively benefit the application of Quantum Hall Array (QHA). Quantum Hall Effect (QHE) serves as the fundamental element for achieving Quantum Hall Array Resistance standard (QHARS), which holds the potential for realizing three crucial units in the International System of Units (SI): the ohm, the ampere, and the kilogram. Within this thesis, QHARS achieves a resistance value of approximately 109 Ω with an accuracy of 0.2 nΩ/Ω. The dependable fabrication of such a precise array relies on critical enabling technologies, including uniform molecular doping and the creation of superconducting leads with low contact resistance across all array elements, thereby estimating the impact of contact resistance to be less than 20 nΩ. The QHA developed in this context also satisfies the stringent requirement for high current in instruments like the Kibble balance, which is utilized in the realization of the kilogram using QHARS.

In metrology QHRS and QHARS are expected to have a long shelf life with minor deviation in their electrical properties. Hence stability of these devices is analyzed over a period of 2 years. The storage solution proposed in this thesis is a mixture of oxygen absorber and desiccant. The samples stored in this mixture exhibited a relative change in carrier density below 0.01 % per day and no discernable degradation of quantization accuracy at the part-per-billion level over a period of 700 days. We foresee that this technique can allow for simple and stable long-term storage of polymer-encapsulated molecular doped epigraphene quantum Hall standards, removing another barrier for their widespread use in practical metrology.

8.2 Outlook

The edge contact fabrication process employed in this thesis highlights the potential for scalable fabrication of edge contacts to graphene could be readily extended to a diverse range of two-dimensional (2D) materials by employing a narrow-wide-narrow opening in the resist. It is also conceivable that similar outcomes might be achievable through optical lithography methods, albeit with some adjustments and careful selection of resist layers, effectively reducing the cost of the entire process.

Although conventional III-IV type sensors currently outperform epigraphene Hall sensors at room temperature in terms of detection limit, their efficacy diminishes rapidly at high temperatures. The investigation of epigraphene Hall sensor performance at high temperatures emphasizes the stability and robustness of these sensors even under extreme temperature conditions, solidifying their potential for widespread adoption in various industries and applications. The development of an alternative doping method capable of further enhancing the high-temperature performance is anticipated to be the key to the future success of epigraphene Hall sensors.

Through the parallel interconnection of these Hall sensors in arrays as seen in Figure 8.1(a), it is possible to increase the overall magnetic field sensitivity. In this configuration, the voltage noise (V_N) spectral density measured at $I_B = 400$ μA is lower compared to the single device as seen in Figure 8.1(b). Additionally, room temperature Hall measurement is performed for the parallel configuration (Figure 8.1(c)), which resulted in Hall coefficient $R_H = 791$ Ω/T. At 20 KHz, the noise voltage measured in the parallel configuration of Hall sensors is half that of the single device, resulting in a remarkable sensitivity of $B_{MIN} = 9.5$ nT/$\sqrt{\text{Hz}}$, setting a new record for low sensitivity for epitaxial graphene-based devices. Both the devices are doped with molecular dopant F4TCNQ, to tune the Fermi level near the Dirac point.

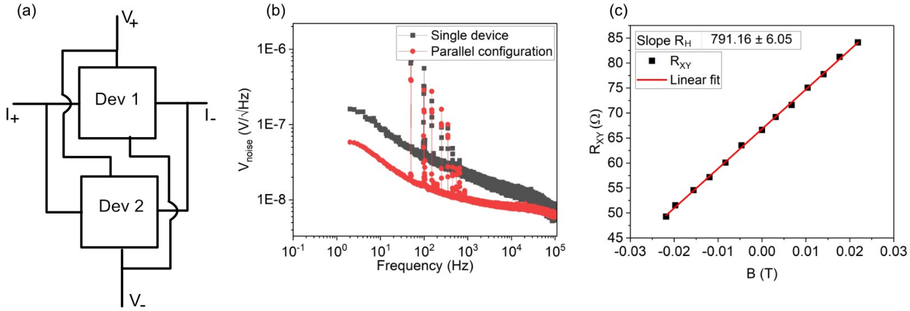

Figure 8.1: (a) The Hall sensors are arranged in a parallel configuration. (b) A comparison of the spectral density of noise voltage between a single 1 mm Hall sensor and the parallel configuration of two 1 mm Hall sensor devices is depicted in (a). (c) The Hall measurement of the parallel setup. The slope observed signifies the Hall coefficient $R_H \approx 791$ Ω/T.

It can be seen that the fabrication of arrays is a feasible route to push down the limits of B_{MIN}, scaling down as $\sim 1/\sqrt{k}$, with k the number of interconnected Hall sensors. This finding is instrumental in guiding the design of sensors utilizing scalable material growth and fabrication techniques, with the aim of minimizing the impact of noise and enhancing the sensitivity of the devices. This advancement presents an encouraging opportunity for the use of epigraphene-based Hall sensors, enabling the coverage of magnetic field sensitivities below nT. Currently, achieving such sensitivities necessitates complex and expensive technologies like flux gate magnetometers and SQUID

This work showed the possibility of fabricating QHARS with a resistance value of 109 Ω with the precision of 0.2 nΩ/Ω. By designing series and parallel combinations of Hall elements, it is possible to obtain decadic values of QHARS such as 10, 100, 1000, and 1 MΩ, which is usually preferred in metrology of SI systems [87]. In addition to the established metrological guidelines, we propose additional methods to improve the accuracy of the comparison measurements. For example, a 100 Ω array could be divided into 50 + 30 + 20 Ω for non-unity ratio comparisons to reveal potential errors like parallel leakages across the quantum Hall channel. Moreover, it is possible to design two arrays with equivalent resistances by employing different quantities of individual Hall bars for each array. This can be accomplished through redundant parallel and series connections. Specifically, the single Hall bar elements in one array can be substituted with four elements, employing two sets of two serially connected Hall bars in parallel, all while maintaining the total array resistance unchanged. Consequently, the current passing through a single Hall bar element in each array would differ. In the event of any deviation from perfect quantization in the Hall bar elements of either array, the distinct currents could result in varying resistance responses. We anticipate that these array-specific quantization tests will complement the existing tests conducted on single Hall bars in the future.

So far in this thesis applications of epigraphene based on classical Hall effect and quantum Hall effect, such as Hall sensors, QHRS and QHARS are discussed. But the SiC due to its large bandgap ($E_G \geq 3.2$ eV), is an excellent candidate for optoelectronics. Epitaxial growth of graphene on SiC is usually performed at temperatures > 1850 °C. At this high temperature, epitaxial growth results in single crystalline high-quality graphene but also reduces the crystal imperfections and buried traps in SiC, thereby increasing the recombination time of minority photo-generated carriers. This leads to epigraphene MSM detectors achieving close to 100 % internal quantum efficiency and due to extremely low dark current, it was possible to achieve record high specific detectivities in these detectors. Epigraphene is particularly suitable to implement the fully planar device architecture of the MSM structure with a low processing effort and makes it technologically attractive for the development of high-performance multi-pixel UV sensor arrays.

A typical challenge of metal semiconductor-metal detectors made with traditional semiconductors and metal films has been (and continues to be) to control the metal-

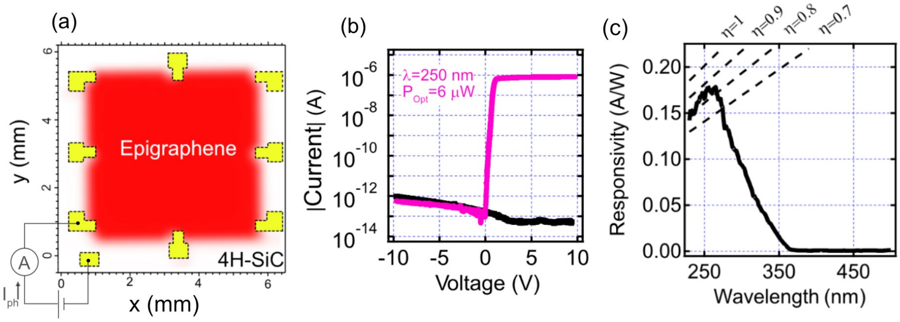

Figure 8.2: (a) Scanning photocurrent at $V_B = 10$ V indicates that the effective area for photocurrent generation is directly beneath the epigraphene sheet.(b) I-V characteristics for device A under both illumination (pink) and dark conditions (black). (c) Spectral responsivity for device A at $V_B = 10$ V, solely illuminated on the epigraphene sheet (light spot 1×1.5 mm^2). The peak responsivity of R =175 mA/W is achieved at $\lambda = 254$ nm. Dashed lines represent various quantum efficiencies η.

semiconductor interface reliably. For epigraphene, the graphene layer act as the metal, and it is produced at high temperature in quasi-thermodynamic conditions, making it highly reproducible. This allows us to demonstrate unprecedently high responsivity to UV light using SiC substrates from two different suppliers - this is important for future commercial applications of 2D materials. By deposition/growth of 2D materials with energy gaps smaller than SiC directly over epitaxial graphene like in a tandem architecture, there is a possibility to produce solar cells that could absorb solar energy from a wider spectrum. This opens up a branch of physics that demands its attention for sustainability and energy production.

This thesis showcases three potential applications of epigraphene, all aimed at demonstrating its capability to outperform traditional technologies in its specific domains. The fabrication of these proof-of-concept devices prioritized scalability and future industrial integration. The exceptional attributes of graphene are yet to be fully harnessed, but the results of this research are anticipated to provide a roadmap for future progress and enhancements in epigraphene-based technology, ultimately helping it to transition from academic laboratory to widespread industrial implementation.

References

[1] A. S. Mayorov, R. V. Gorbachev, S. V. Morozov, *et al.*, "Micrometer-scale ballistic transport in encapsulated graphene at room temperature," *Nano Letters*, vol. 11, no. 6, pp. 2396–2399, 2011, ISSN: 15306984.

[2] N. D. Arora, J. R. Hauser, and D. J. Roulston, "Electron and Hole Mobilities in Silicon as a Function of Concentration and Temperature," *IEEE Transactions on Electron Devices*, vol. 29, no. 2, pp. 292–295, 1982, ISSN: 15579646.

[3] R. R. Nair, P. Blake, A. N. Grigorenko, *et al.*, "Fine structure constant defines visual transparency of graphene," *Science*, vol. 320, no. 5881, p. 1308, 2008, ISSN: 00368075.

[4] S. Chen, A. L. Moore, W. Cai, *et al.*, "Raman measurements of thermal transport in suspended monolayer graphene of variable sizes in vacuum and gaseous environments," *ACS Nano*, vol. 5, no. 1, pp. 321–328, 2011, ISSN: 19360851.

[5] A. A. Balandin, S. Ghosh, W. Bao, *et al.*, "Superior thermal conductivity of single-layer graphene," *Nano Letters*, vol. 8, no. 3, pp. 902–907, 2008, ISSN: 15306984.

[6] M. Lisker, M. Lukosius, R. Lukose, C. Wenger, and A. Mai, "(Invited) Challenges of Graphene Process Integration in CMOS Technology," *ECS Meeting Abstracts*, vol. MA2019-02, no. 25, pp. 1193–1193, 2019.

[7] D. Akinwande, C. Huyghebaert, C. H. Wang, *et al.*, “Graphene and two-dimensional materials for silicon technology,” *Nature*, vol. 573, no. 7775, pp. 507–518, 2019, ISSN: 14764687.

[8] J. R. Prekodravac, D. P. Kepić, J. C. Colmenares, D. A. Giannakoudakis, and S. P. Jovanović, “A comprehensive review on selected graphene synthesis methods: From electrochemical exfoliation through rapid thermal annealing towards biomass pyrolysis,” *Journal of Materials Chemistry C*, vol. 9, no. 21, pp. 6722–6748, 2021, ISSN: 20507526.

[9] A. R. Urade, I. Lahiri, and K. S. Suresh, “Graphene Properties, Synthesis and Applications: A Review,” *Jom*, vol. 75, no. 3, pp. 614–630, 2023, ISSN: 15431851.

[10] T. Kobayashi, M. Bando, N. Kimura, *et al.*, “Production of a 100-m-long high-quality graphene transparent conductive film by roll-to-roll chemical vapor deposition and transfer process,” *Applied Physics Letters*, vol. 102, no. 2, 2013, ISSN: 00036951.

[11] X. Wu, G. Zhong, L. D’Arsié, *et al.*, “Growth of Continuous Monolayer Graphene with Millimeter-sized Domains Using Industrially Safe Conditions,” *Scientific Reports*, vol. 6, no. February, pp. 2–8, 2016, ISSN: 20452322.

[12] F. Liu, P. Li, H. An, P. Peng, B. McLean, and F. Ding, “Achievements and Challenges of Graphene Chemical Vapor Deposition Growth,” *Advanced Functional Materials*, vol. 32, no. 42, 2022, ISSN: 16163028.

[13] C. Berger, Z. Song, T. Li, *et al.*, “Ultrathin epitaxial graphite: 2D electron gas properties and a route toward graphene-based nanoelectronics,” *Journal of Physical Chemistry B*, vol. 108, no. 52, pp. 19 912–19 916, 2004, ISSN: 15206106.

[14] H. Huang, W. Chen, S. Chen, A. Thye, and S. Wee, “Bottom-up Growth of Epitaxial,” *ACS nano*, vol. 2, no. 12, pp. 2513–2518, 2008.

[15] K. V. Emtsev, A. Bostwick, K. Horn, *et al.*, “Towards wafer-size graphene layers by atmospheric pressure graphitization of silicon carbide.,” *Nature materials*, vol. 8, no. 3, pp. 203–207, 2009, ISSN: 1476-1122.

[16] A. Allain, J. Kang, K. Banerjee, and A. Kis, “Electrical contacts to two-dimensional semiconductors,” *Nature Materials*, vol. 14, no. 12, pp. 1195–1205, 2015, ISSN: 14764660.

[17] H. He, K. H. Kim, A. Danilov, *et al.*, “Uniform doping of graphene close to the Dirac point by polymer-assisted assembly of molecular dopants,” *Nature Communications*, vol. 9, no. 1, 2018, ISSN: 20411723.

[18] P. R. Wallace, “The Band Theory of Graphite,” *Physical Review*, vol. 71, no. 9, pp. 622–634, May 1947, ISSN: 0031-899X.

[19] A. H. Castro Neto, N. M. R. Peres, K. S. Novoselov, *et al.*, “The electronic properties of graphene,” *Reviews of Modern Physics*, vol. 81, no. 1, pp. 109–162, Sep. 2009, ISSN: 0034-6861.

[20] J. Martin, N. Akerman, G. Ulbricht, *et al.*, “Observation of electron-hole puddles in graphene using a scanning single-electron transistor,” *Nature Physics*, vol. 4, no. 2, pp. 144–148, 2008, ISSN: 17452481.

[21] S. Cho and M. S. Fuhrer, “Charge transport and inhomogeneity near the minimum conductivity point in graphene,” *Physical Review B - Condensed Matter and Materials Physics*, vol. 77, no. 8, pp. 8–11, 2008, ISSN: 10980121.

[22] Q. Li, E. H. Hwang, and S. Das Sarma, “Disorder-induced temperature-dependent transport in graphene: Puddles, impurities, activation, and diffusion,” *Physical Review B - Condensed Matter and Materials Physics*, vol. 84, no. 11, 2011, ISSN: 10980121.

[23] R. S. Popovic, *Hall Effect Devices*, second. CRC Press, 2003, p. 420, ISBN: 9781420034226.

[24] K. V. Klitzing, G. Dorda, and M. Pepper, “New method for high-accuracy determination of the fine-structure constant based on quantized hall resistance,” *Physical Review Letters*, vol. 45, no. 6, pp. 494–497, 1980, ISSN: 00319007.

[25] K. S. Novoselov, A. K. Geim, S. V. Morozov, *et al.*, “Two-dimensional gas of massless Dirac fermions in graphene,” vol. 438, no. November, pp. 197–200, 2005.

[26] V. P. Gusynin and S. G. Sharapov, “Unconventional integer quantum hall effect in graphene,” *Physical Review Letters*, vol. 95, no. 14, pp. 2–5, 2005, ISSN: 00319007.

[27] H. He, K. H. Kim, A. Danilov, *et al.*, “Uniform doping of graphene close to the Dirac point by polymer-assisted assembly of molecular dopants,” *Nature Communications*, vol. 9, no. 1, p. 3956, 2018, ISSN: 20411723.

[28] L.J. va der PAUW, “A method of measuring specific resistivity and Hall effect of discs of arbitrary shape,” *Philips Research Reports*, vol. 13.1, pp. 1–9, 1958.

[29] L. v. d. PAUW, “A method of measuring the resistivity and Hall coefficient of Lamellae of arbitrary shape,” *Philips technical review*, vol. 20, pp. 220–224, 1958.

[30] F. S. Oliveira, R. B. Cipriano, F. T. da Silva, E. C. Romão, and C. A. dos Santos, “Simple analytical method for determining electrical resistivity and sheet resistance using the van der Pauw procedure,” *Scientific Reports*, vol. 10, no. 1, pp. 1–8, 2020, ISSN: 20452322.

[31] K. N. Parrish and D. Akinwande, “Impact of contact resistance on the transconductance and linearity of graphene transistors,” *Applied Physics Letters*, vol. 98, no. 18, pp. 96–99, 2011, ISSN: 00036951.

[32] T. Yager, A. Lartsev, K. Cedergren, *et al.*, “Low contact resistance in epitaxial graphene devices for quantum metrology,” *AIP Advances*, vol. 5, no. 8, p. 087 134, Aug. 2015, ISSN: 2158-3226.

[33] F. Delahaye, “Technical guidelines for reliable measurements of the quantized hall resistance,” *Metrologia*, vol. 26, no. 1, pp. 63–68, 1989, ISSN: 00261394.

[34] G. R. Fisher and P. Barnes, “Towards a unified view of polytypism in silicon carbide,” *Philosophical Magazine B: Physics of Condensed Matter; Statistical Mechanics, Electronic, Optical and Magnetic Properties*, vol. 61, no. 2, pp. 217–236, 1990, ISSN: 13642812.

[35] H. Morkoç, S. Strite, G. B. Gao, M. E. Lin, B. Sverdlov, and M. Burns, “Large-band-gap SiC, III-V nitride, and II-VI ZnSe-based semiconductor device technologies,” *Journal of Applied Physics*, vol. 76, no. 3, pp. 1363–1398, Aug. 1994, ISSN: 0021-8979.

[36] a. Van Bommel, J. Crombeen, and A. Van Tooren, “LEED and Auger electron observations of the SiC(0001) surface,” *Surface Science*, vol. 48, no. 2, pp. 463–472, Mar. 1975, ISSN: 00396028.

[37] C. Virojanadara, M. Syväjarvi, R. Yakimova, L. Johansson, A. Zakharov, and T. Balasubramanian, “Homogeneous large-area graphene layer growth on 6H-SiC(0001),” *Physical Review B*, vol. 78, no. 24, p. 245 403, Dec. 2008, ISSN: 1098-0121.

[38] J. Robinson, X. Weng, K. Trumbull, *et al.*, "Nucleation of epitaxial graphene on SiC(0001)," *ACS Nano*, vol. 4, no. 1, pp. 153–158, 2010, ISSN: 19360851.

[39] W. A. D. Heer, C. Berger, M. Ruan, *et al.*, "Large area and structured epitaxial graphene produced by confinement controlled sublimation of silicon carbide," *PNAS*, 2011.

[40] G. R. Yazdi, T. Iakimov, and R. Yakimova, "Epitaxial graphene on SiC: A review of growth and characterization," *Crystals*, vol. 6, no. 5, 2016, ISSN: 20734352.

[41] M. Kruskopf, D. M. Pakdehi, K. Pierz, *et al.*, "Comeback of epitaxial graphene for electronics: Large-area growth of bilayer-free graphene on SiC," *2D Materials*, vol. 3, no. 4, 2016, ISSN: 20531583.

[42] S. K. Lilov, "Study of the equilibrium processes in the gas phase during silicon carbide sublimation," *Materials Science and Engineering B*, vol. 21, no. 1, pp. 65–69, 1993, ISSN: 09215107.

[43] T. W. Hu, F. Ma, D. Y. Ma, *et al.*, "Evidence of atomically resolved 6 × 6 buffer layer with long-range order and short-range disorder during formation of graphene on 6H-SiC by thermal decomposition," *Applied Physics Letters*, vol. 102, no. 17, pp. 4–7, 2013, ISSN: 00036951.

[44] S. Fiori, Y. Murata, S. Veronesi, A. Rossi, C. Coletti, and S. Heun, "Li-intercalated graphene on SiC(0001): An STM study," *Physical Review B*, vol. 96, no. 12, pp. 1–8, 2017, ISSN: 24699969.

[45] T. Cavallucci and V. Tozzini, "Intrinsic structural and electronic properties of the Buffer Layer on Silicon Carbide unraveled by Density Functional Theory," *Scientific Reports*, vol. 8, no. 1, pp. 1–10, 2018, ISSN: 20452322.

[46] C. P. Huelmo, F. Iribarne, and P. A. Denis, "Elucidating the electronic and magnetic properties of epitaxial graphene grown on SiC with a defective buffer layer," *Journal of Materials Science*, vol. 56, no. 19, pp. 11 386–11 401, 2021, ISSN: 15734803.

[47] S. V. Kopylov, A. Tzalenchuk, S. Kubatkin, and V. I. Fal'Ko, "Charge transfer between epitaxial graphene and silicon carbide," *Applied Physics Letters*, vol. 97, no. 11, pp. 2008–2011, 2010, ISSN: 00036951.

[48] C. Riedl, C. Coletti, T. Iwasaki, A. A. Zakharov, and U. Starke, “Quasi-free-standing epitaxial graphene on SiC obtained by hydrogen intercalation,” *Physical Review Letters*, vol. 103, no. 24, pp. 1–4, 2009, ISSN: 00319007.

[49] T. J. Janssen, S. Rozhko, I. Antonov, *et al.*, “Operation of graphene quantum Hall resistance standard in a cryogen-free table-top system,” *2D Materials*, vol. 2, no. 3, p. 035 015, Aug. 2015, ISSN: 20531583.

[50] J. A. Alexander-Webber, J. Huang, D. K. Maude, *et al.*, “Giant quantum Hall plateaus generated by charge transfer in epitaxial graphene,” *Scientific Reports*, vol. 6, no. May, p. 30 296, 2016, ISSN: 2045-2322.

[51] T. Yager, A. Lartsev, S. Mahashabde, *et al.*, “Express Optical Analysis of Epitaxial Graphene on SiC: Impact of Morphology on Quantum Transport,” *Nano Letters*, vol. 13, no. 9, pp. 4217–4223, Sep. 2013, ISSN: 1530-6984.

[52] TUINSTRA F and KOENIG JL, “Raman Spectrum of Graphite,” *Journal of Chemical Physics*, vol. 53, no. 3, pp. 1126–1130, 1970, ISSN: 00219606.

[53] F. Fromm, M. H. Oliveira, A. Molina-Sánchez, *et al.*, “Contribution of the buffer layer to the Raman spectrum of epitaxial graphene on SiC(0001),” *New Journal of Physics*, vol. 15, no. 100, 2013, ISSN: 13672630.

[54] A. C. Ferrari and D. M. Basko, “Raman spectroscopy as a versatile tool for studying the properties of graphene,” *Nature Nanotechnology*, vol. 8, no. 4, pp. 235–246, 2013.

[55] A. Ben Gouider Trabelsi, F. V. Kusmartsev, A. Kusmartseva, F. H. Alkallas, S. Alfaify, and M. Shkir, “Raman spectroscopy imaging of exceptional electronic properties in epitaxial graphene grown on SiC,” *Nanomaterials*, vol. 10, no. 11, pp. 1–37, 2020, ISSN: 20794991.

[56] D. S. Lee, C. Riedl, B. Krauss, K. V. Klitzing, U. Starke, and J. H. Smet, “Raman spectra of epitaxial graphene on SiC and of epitaxial graphene transferred to SiO2,” *Nano Letters*, vol. 8, no. 12, pp. 4320–4325, 2008, ISSN: 15306984.

[57] L. Wang, “One-Dimensional Electrical Contact to,” *Science (New York, N.Y.)432*, vol. 342, no. November, pp. 614–617, 2013.

[58] Y. Matsuda, W.-q. Deng, and W. a. G. Iii, “Contact Resistance of “ End- contacted ” Metal – Graphene and Metal – Nanotube Interfaces,” pp. 1–6, 2010.

[59] J. Tersoff, “Contact resistance of carbon nanotubes,” *Applied Physics Letters*, vol. 74, no. 15, pp. 2122–2124, 1999, ISSN: 00036951.

[60] Y. Matsuda, W. Q. Deng, and W. A. Goddard, “Contact resistance properties between nanotubes and various metals from quantum mechanics,” *Journal of Physical Chemistry C*, vol. 111, no. 29, pp. 11 113–11 116, 2007, ISSN: 19327447.

[61] H. He, K. H. Kim, A. Danilov, *et al.*, “Uniform doping of graphene close to the Dirac point by polymer-assisted assembly of molecular dopants,” *Nature Communications*, vol. 9, no. 1, pp. 3–9, 2018, ISSN: 20411723.

[62] L. Wang, I. Meric, P. Y. Huang, *et al.*, “One-Dimensional Electrical Contact to a Two-Dimensional Material,” *Science*, vol. 342, no. 6158, pp. 614–617, Nov. 2013, ISSN: 0036-8075.

[63] K. Nagashio, T. Nishimura, K. Kita, and A. Toriumi, “Contact resistivity and current flow path at metal/graphene contact,” *Applied Physics Letters*, vol. 97, no. 14, pp. 8–11, 2010, ISSN: 00036951.

[64] B. T. Schaefer, L. Wang, A. Jarjour, *et al.*, “Magnetic field detection limits for ultraclean graphene Hall sensors,” *Nature Communications*, vol. 11, no. 1, pp. 1–8, 2020, ISSN: 20411723.

[65] N. Shetty, H. He, R. Mitra, *et al.*, “Scalable fabrication of edge contacts to 2D materials,” 2022.

[66] M. Cornils and O. Paul, “The magnetic calibration and optimization of symmetric hall plates may be accomplished even in the absence of a magnetic field,” *Proceedings of the IEEE International Conference on Micro Electro Mechanical Systems (MEMS)*, pp. 940–943, 2008, ISSN: 10846999.

[67] M. Cornils, *Sheet Resistance and Hall Mobility Determination Beyond Van Der Pauw.* Der Andere Verlag, 2009, p. 196, ISBN: 9783899599329.

[68] Y. Zhang, V. W. Brar, C. Girit, A. Zettl, and M. F. Crommie, “Origin of spatial charge inhomogeneity in graphene,” *Nature Physics*, vol. 5, no. 10, pp. 722–726, Oct. 2009, ISSN: 1745-2473.

[69] K. Vervaeke, E. Simoen, G. Borghs, and V. V. Moshchalkov, "Size dependence of microscopic Hall sensor detection limits," *Review of Scientific Instruments*, vol. 80, no. 7, 2009, ISSN: 00346748.

[70] AKM, *AKM Hall Sensor Catalog. Akahi Kasei Microdevices*, 2020.

[71] J. Dauber, A. A. Sagade, M. Oellers, *et al.*, "Ultra-sensitive Hall sensors based on graphene encapsulated in hexagonal boron nitride," *Applied Physics Letters*, vol. 106, no. 19, 2015, ISSN: 00036951.

[72] L. Huang, Z. Zhang, B. Chen, X. Ma, H. Zhong, and L. M. Peng, "Ultrasensitive graphene Hall elements," *Applied Physics Letters*, vol. 104, no. 18, 2014, ISSN: 00036951.

[73] C. C. Tang, M. Y. Li, L. J. Li, C. C. Chi, and J. C. Chen, "Characteristics of a sensitive micro-Hall probe fabricated on chemical vapor deposited graphene over the temperature range from liquid-helium to room temperature," *Applied Physics Letters*, vol. 99, no. 11, 2011, ISSN: 00036951.

[74] A. Dankert, B. Karpiak, and S. P. Dash, "Hall sensors batch-fabricated on all-CVD h-BN/graphene/h-BN heterostructures," *Scientific Reports*, vol. 7, no. 1, pp. 1–7, 2017, ISSN: 20452322.

[75] V. Panchal, K. Cedergren, R. Yakimova, A. Tzalenchuk, S. Kubatkin, and O. Kazakova, "Small epitaxial graphene devices for magnetosensing applications," *Journal of Applied Physics*, vol. 111, no. 7, pp. 8–11, 2012, ISSN: 00218979.

[76] F. N. Hooge and A. M. Hoppenbrouwers, "Amplitude distribution of 1/f noise," *Physica*, vol. 42, no. 3, pp. 331–339, 1969, ISSN: 00318914.

[77] Y. Zhang, E. E. Mendez, and X. Du, "Mobility-Dependent Low-Frequency Noise in Graphene Field-Effect Transistors," no. 10, pp. 8124–8130, 2011.

[78] M. Tacano, H. Tanoue, and Y. Sugiyama, "Dependence of Hooge Parameter of Compound Semiconductors on Temperature," *Japanese Journal of Applied Physics*, vol. 31, no. 3B, pp. L316–L139, 1992, ISSN: 13474065.

[79] S. Peng, Z. Jin, D. Zhang, *et al.*, “Carrier-Number-Fluctuation Induced Ultralow 1/f Noise Level in Top-Gated Graphene Field Effect Transistor,” *ACS Applied Materials and Interfaces*, vol. 9, no. 8, pp. 6661–6665, 2017, ISSN: 19448252.

[80] Y. Wang, V. X. Ho, Z. N. Henschel, M. P. Cooney, and N. Q. Vinh, “Effect of High-κ Dielectric Layer on 1/ f Noise Behavior in Graphene Field-Effect Transistors,” *ACS Applied Nano Materials*, vol. 4, no. 4, pp. 3647–3653, 2021, ISSN: 25740970.

[81] M. Marzano, A. Cultrera, M. Ortolano, and L. Callegaro, “A correlation noise spectrometer for flicker noise measurement in graphene samples,” *Measurement Science and Technology*, vol. 30, no. 3, 2019, ISSN: 13616501.

[82] A. A. Balandin, “Low-frequency 1/f noise in graphene devices,” *Nature Nanotechnology*, vol. 8, no. 8, pp. 549–555, 2013, ISSN: 17483395.

[83] M. Kayyalha and Y. P. Chen, “Observation of reduced 1/f noise in graphene field effect transistors on boron nitride substrates,” *Applied Physics Letters*, vol. 107, no. 11, 2015, ISSN: 00036951.

[84] A. Porciatti, Z. Wang, P. Marconcini, *et al.*, “Flicker noise in graphene-based Hall sensors,” *2017 International Conference on Noise and Fluctuations, ICNF 2017*, pp. 16–19, 2017.

[85] M. Kumar, A. Laitinen, D. Cox, and P. J. Hakonen, “Ultra low 1/f noise in suspended bilayer graphene,” *Applied Physics Letters*, vol. 106, no. 26, 2015, ISSN: 00036951.

[86] R. Ribeiro-Palau, F. Lafont, J. Brun-Picard, *et al.*, “Quantum Hall resistance standard in graphene devices under relaxed experimental conditions,” *Nature Nanotechnology*, vol. 10, no. 11, pp. 965–971, 2015, ISSN: 17483395.

[87] M. Ortolano, M. Abrate, and L. Callegaro, “On the synthesis of quantum Hall array resistance standards,” *Metrologia*, vol. 52, no. 1, pp. 31–39, 2015, ISSN: 16817575.

[88] S. Komiyama, H. Sakuma, K. Ikushima, and K. Hirakawa, “Electron temperature of hot spots in quantum Hall conductors,” *Physical Review B - Condensed Matter and Materials Physics*, vol. 73, no. 4, pp. 1–5, 2006, ISSN: 10980121.

[89] F. Delahaye, “Series and parallel connection of multiterminal quantum Hall-effect devices,” *Journal of Applied Physics*, vol. 73, no. 11, pp. 7914–7920, 1993, ISSN: 00218979.

[90] M. Kruskopf, A. F. Rigosi, A. R. Panna, *et al.*, “Next-generation crossover-free quantum Hall arrays with superconducting interconnections,” *Metrologia*, vol. 56, no. 6, 2019, ISSN: 16817575.

[91] M. Büttiker, “Absence of backscattering in the quantum Hall effect in multiprobe conductors,” *Physical Review B*, vol. 38, no. 14, pp. 9375–9389, 1988, ISSN: 01631829.

[92] J. M. Williams, T. J. Janssen, G. Rietveld, and E. Houtzager, “An automated cryogenic current comparator resistance ratio bridge for routine resistance measurements,” *Metrologia*, vol. 47, no. 3, pp. 167–174, 2010, ISSN: 00261394.

[93] S. Slizovskiy and V. Fal’Ko, “Cooling of chiral heat transport in the quantum Hall effect regime of graphene,” *Physical Review B*, vol. 96, no. 7, pp. 1–6, 2017, ISSN: 24699969.

[94] M. Suzuki, M. Baba, and T. Anayama, “Critical Magnetic Fields of Superconducting NbN Films Prepared by Reactive Sputtering,” *Japanese Journal of Applied Physics*, vol. 26, no. S3-2, pp. 947–948, 1987, ISSN: 13474065.

[95] D. P. Hampshire, K. E. Gray, and R. T. Kampwirth, “Scaling Laws for the Critical Current Density of nbn Films in High Magnetic Fields,” *IEEE Transactions on Applied Superconductivity*, vol. 3, no. 1, pp. 1246–1252, 1993, ISSN: 15582515.

[96] H. He, S. Lara-Avila, K. H. Kim, *et al.*, “Polymer-encapsulated molecular doped epigraphene for quantum resistance metrology,” *Metrologia*, vol. 56, no. 4, 2019, ISSN: 16817575.

[97] F. Delahaye and B. Jeckelmann, “Revised technical guidelines for reliable dc measurements of the quantized Hall resistance,” *Metrologia*, vol. 40, no. 5, pp. 217–223, 2003, ISSN: 00261394.

[98] D. W. Allan, “Should the Classical Variance Be Used As a Basic Measure in Standards Metrology?” *IEEE Transactions on Instrumentation and Measurement*, vol. IM-36, no. 2, pp. 646–654, 1987, ISSN: 15579662.

[99] R. Ribeiro-Palau, F. Lafont, J. Brun-Picard, *et al.*, “Quantum Hall resistance standard in graphene devices under relaxed experimental conditions,” *Nature Nanotechnology*, vol. 10, no. 11, pp. 965–971, 2015, ISSN: 17483395.

[100] M. Kruskopf, A. F. Rigosi, A. R. Panna, *et al.*, “Two-Terminal and Multi-Terminal Designs for Next-Generation Quantized Hall Resistance Standards: Contact Material and Geometry,” *IEEE Transactions on Electron Devices*, vol. 66, no. 9, pp. 3973–3977, 2019, ISSN: 15579646.

[101] T. J. Janssen, N. E. Fletcher, R. Goebel, *et al.*, “Graphene, universality of the quantum Hall effect and redefinition of the SI system,” *New Journal of Physics*, vol. 13, pp. 0–6, 2011, ISSN: 13672630.

[102] W. Poirier, A. Bounouh, K. Hayashi, *et al.*, “R K/100 and R K/200 quantum Hall array resistance standards,” *Journal of Applied Physics*, vol. 92, no. 5, pp. 2844–2854, 2002, ISSN: 00218979.

[103] A. Lartsev, *Quantum Hall devices on epitaxial graphene : towards large-scale integration.* 2015, ISBN: 9789175972626.

[104] A. R. Panna, I. F. Hu, M. Kruskopf, *et al.*, “Graphene quantum Hall effect parallel resistance arrays,” *Physical Review B*, vol. 103, no. 7, pp. 1–8, 2021, ISSN: 24699969.

[105] D. H. Chae, W. S. Kim, T. Oe, and N. H. Kaneko, “Direct comparison of 1 MΩ quantized Hall array resistance and quantum Hall resistance standard,” *Metrologia*, vol. 55, no. 5, pp. 645–653, 2018, ISSN: 16817575.

[106] F. P. Piquemal, J. Blanchet, G. Genevès, and J. P. André, “A first attempt to realize (multiple-QHE devices)-series array resistance standards,” *IEEE Transactions on Instrumentation and Measurement*, vol. 48, no. 2, pp. 296–300, 1999, ISSN: 00189456.

[107] J. Park, W. S. Kim, and D. H. Chae, “Realization of 5 h e 2 with graphene quantum Hall resistance array,” *Applied Physics Letters*, vol. 116, no. 9, 2020, ISSN: 00036951.

[108] I. A. Robinson and S. Schlamminger, “The watt or Kibble balance: A technique for implementing the new SI definition of the unit of mass,” *Metrologia*, vol. 53, no. 5, A46–A74, 2016, ISSN: 16817575.

[109] H. He, N. Shetty, S. Kubatkin, *et al.*, “Highly efficient UV detection in a metal-semiconductor-metal detector with epigraphene,” *Applied Physics Letters*, vol. 120, no. 19, 2022, ISSN: 00036951.

II Recipe

RECIPE A

RCA cleaning

The SiC wafer/diced chips must undergo RCA cleaning procedure before the growth. RCA stands for "Radio Corporation of America", a process developed by Werner Kern in 1965 while working for RCA [1].

- Mix 200 mL deionized water, 40 mL ammonia water (NH_3 30 wt. %) and 40 mL aqueous hydrogen peroxide (H_2O_2 30 wt. %). This mixture is referred to as SC1 (Standard Cleaning 1).
- Heat to 80 °C on a hotplate.
- Submerge SiC chips in the heated solution for 10 min.
- Rinse in a deionized water bath.
- Submerge the wafer/chips for 30 s in a 1:50 aqueous solution of hydrofluoric acid (HF) kept at 25 °C.
- Mix 200 mL deionized water, 40 mL hydrochloric acid (HCL_3 37 wt. %) and 40 mL aqueous hydrogen peroxide (H_2O_2 30 wt. %). This mixture is referred to as SC2 (Standard Cleaning 2).
- Heat to 80 °C on a hotplate.
- Submerge SiC chips in the heated solution for 10 min.

- Rinse in a deionized water bath.
- Dry using nitrogen gas.

RECIPE B

Epitaxial graphene growth

- Load the RCA cleaned SiC chip/wafer into the 4-inch graphite crucible with the Si-face facing downward toward the crucible bottom. Ensure the chip/wafer rests on the graphite stage.
- Close the chamber and employ a roughing pump to lower the pressure to below 2 mbar.
- Use a turbo pump to further reduce the pressure to below 5×10^{-7} mbar.
- Optionally, perform an additional annealing step by manually heating the sample for 10 minutes until the temperature exceeds 355 °C, while maintaining the pumping process.
- Utilize the RF (12 KHz) heater to gradually increase the temperature to 1150 °C at a rate of 40 °C per minute.
- Begin ramping up the temperature to 1700 °C at a rate of 20 °C per minute.
- While heating, cease pumping and introduce argon gas into the chamber, stopping when the pressure reaches 800 mbar.
- Once the temperature reaches 1700 °C, maintain this temperature for 5 minutes.

- Turn off the heater and allow for natural cooling, which typically takes around 4 hours.

RECIPE C

Electron Beam Lithography

The scalable edge contact fabrication process is a two-step lithography process. Step 1:

- Spin coat PMMA 950k, 4 wt. % solid content in anisole (PMMA A4) at 6,000 rpm for 1 minute, resulting in a film thickness of approximately 150 nm.
- Perform baking on a hot plate at 160 °C for 5 minutes.
- Spin coat P(MMA-MAA), 6 wt. % in ethyl lactate solvent. (COPEL6). At 6,000 rpm for 1 min, the resulting thickness is $\approx$ 280 nm.
- Perform baking on a hot plate at 160 °C for 5 minutes.
- Spin coat A-RP 6200.13 dissolved in anisole at a 2:1 ratio, spinning at 6,000 rpm for 1 minute, resulting in a film thickness of around 175 nm.
- Perform baking on a hot plate at 160 °C for 5 minutes.
- Expose the sample to an electron beam. For larger features (>1 µm), use a beam current of 35 nA and a dose of 600 $\mu C/cm^2$. For smaller features (<1 µm), opt for a beam current of 2 nA and a dose of 700 $\mu C/cm^2$.
- Develop the top resist layer (A-RP) using o-xylene developer for 30 seconds, rinse in isopropanol IPA and blow dry using N_2 gun.

- Develop the bottom resist layers (COPEL10 and PMMA A4) using IPA 7% (7% H_2O by volume in IPA) for 40 seconds.
- Dry etching of 2D material for a minute, either by using O_2 plasma (50 W, 250 mT chamber pressure, and a 10 sccm flow of oxygen) for epigraphene or by using Ar plasma for Transition metal dichalcogenides (TMDs).
- Deposit metal layers either by physical vapor deposition (PVD) using e-beam evaporation of Ti (5 nm) followed by Au (80 nm) or by using sputter deposition (100 nm NbN).
- Execute a lift-off process using acetone.
- Rinse the sample with isopropanol.
- Dry the sample using nitrogen gas.

Step 2: Isolating the devices.

- Apply a spin-coating process using PMMA A6 (6 wt. % PMMA in anisole) at 6,000 rpm for 1 minute, resulting in a film thickness of approximately 375 nm.
- Perform a baking step for 5 minutes at 170 °C.
- Expose the sample to an electron beam. For larger features (>1 μm), utilize a beam current of 35 nA and a dose of 600 $\mu C/cm^2$. For smaller features (<1 μm), employ a beam current of 2 nA and a dose of 700 $\mu C/cm^2$.
- Develop the resist layer (PMMA A6) using IPA 7% (7% H_2O by volume in IPA) for 1.5 minutes.
- Remove the exposed graphene by subjecting it to 1.5 minutes of oxygen plasma ashing with parameters set to 50 W, 250 mT chamber pressure, and a 10 sccm flow of oxygen. (Ar plasma for TMDs)
- Remove any remaining resist by using acetone.
- Rinse the sample thoroughly with isopropanol.
- Dry the sample using a flow of nitrogen gas.

RECIPE D

Molecular doping

Step 1: Preparing dopant blend The standard blend of dopants, comprising F4TCNQ molecules mixed with PMMA, is prepared according to the following recipe:

- 25 mg of dry F4TCNQ powder is mixed with 3 mL of anisole. This solution is referred to as ‘X’.
- 0.5 mL of X is mixed with 1 mL of PMMA A6 (PMMA, 6 wt. % in anisole), yielding the final dopant blend.

Step 2: Spin coating

- Apply a spin coat of P(MMA-MAA 8.5%) at 6 wt. % in ethyl lactate solvent (COPEL6) at 6,000 rpm for 1 minute to achieve a spacer layer thickness of approximately 100 nm.
- Bake for 5 min at 160 °C.
- Apply a spin coat of the dopant blend at 6,000 rpm for 1 minute to achieve a resulting thickness of approximately 150 nm.
- Bake for 5 min at 160 °C.
- Reapply COPEL6, at 6,000 rpm for 1 minute and bake for 5 min at 160 °C.

- Reapply dopant blend at 6,000 rpm for 1 minute and bake for 5 min at 160 °C.
- Finally again spin coat COPEL6, at 6,000 rpm for 1 minute and bake for 5 min at 160 °C.

III Appendices

APPENDIX A

Cryogenic Current Comparator

Cryogenic Current Comparator (CCC) is employed in electrical metrology to achieve the utmost precision when comparing the ratios of two electrical currents. This technology is crucial for conducting highly accurate measurements of resistances or for amplifying minute currents [2], [3]. The epitaxial graphene Quantum Hall Resistance Standards (QHRSs) have demonstrated the highest level of precision in quantum resistance metrology, enabling measurements of the resistance quantum $h/2e^2$ with accuracy as fine as 0.086 $\mathrm{n}\Omega/\Omega$ (equivalent to 86 parts-per-trillion) [4].

Figure A.1 shows a schematic of one variant of CCC. It consists of two current sources, primary I_P and secondary I_S which feed two resistors R_P being the resistance standard $h/2e^2$ and R_S which is the resistance that is compared against the standard. In the primary circuit, current I_P is also passed through a toroidal core with winding N_P and secondary current I_S through N_S as well using a standard current divider, in phase fraction $\epsilon = R_l/(R_l + R_h)$ of I_S through N_t. All the windings are placed inside a superconducting torus, shown as a grey region in the figure. Now N_P is adjusted such that the ratio N_P/N_S of the windings is set as close as possible to the nominal ratio of the two resistors R_P/R_S to be measured. The magnetic flux created by the shielding current on the torus is $I_{CCC} = N_P I_P - (N_S + \epsilon N_t) I_S$. This flux is sensed by a Superconducting Quantum Interference Device (SQUID) through a pick-up coil placed in the flux. The output voltage of the SQUID system regu-

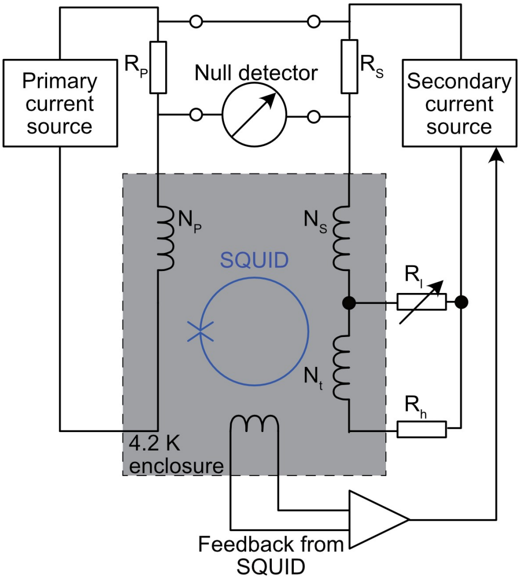

Figure A.1: Schematic circuit diagram of a Cryogenic Current Comparator (CCC) bridge. R_P is usually a Quantum Hall Resistance Standard (QHRS). In the case of graphene, stable plateau $\nu = 2$ for $h/2e^2$ is used to calibrate another resistor R_S.

lates the secondary current source in a closed feedback loop such that the screening current I_{CCC} is nulled. This results in flux equilibrium:

$$N_P I_P - (N_S + \epsilon N_t) I_S = 0 \tag{A.1}$$

with a CCC current ratios $I_S/I_P = N_P/(N_S + \epsilon N_t)$ a relative accuracy of 10^{-12} can be realized [5], [6]. From the fraction ϵ_{eq} setting the equal voltage drops in R_P and R_S (voltage equilibrium), i.e. $R_S I_S = R_P I_P$, one obtains;

$$\frac{I_S}{I_P} = \frac{R_P}{R_S} = \frac{N_P}{(N_S + \epsilon_{eq} N_t)} \tag{A.2}$$

Any deviation from the equilibrium condition is detected by the null detector as a voltage V_d, resulting in the resistance ratio deviation from ideal scenario as:

$$\frac{R_P}{R_S} = \frac{N_P}{(N_S + \epsilon_{eq} N_t)} \frac{V}{V + V_d} \tag{A.3}$$

where V is the voltage across the resistors R_P and R_S under voltage equilibrium condition. The deviation from the equilibrium is detected by the SQUID and corrected to a null value through the feedback signal. The correction signal is proportional to the current ratio deviation, which in turn measures resistance ratio deviation to the level of $n\Omega/\Omega$. If $Q = R_S/R_P$, then the relative deviation of R_S from its nominal value ($R_{S,nominal}$), referred to primary (reference) resistor R_P is expressed as $\Delta_{(R_P - R_S)} = (QR_P - R_{S,nominal})/R_{S,nominal}$. Here the R_P is the reference value and is usually chosen to be a primary standard with quantized resistance value like $h/2e^2$.

APPENDIX B

Noise characterization: Cross correlated power spectrum analyzer

In the simple noise spectrum analysis setup as shown in Figure B.1(a), instrumentation noise is added on top of the device noise of interest. The cross-correlation spectrum analyzer exploits the cross-correlation method to reject the amplifier noise, thereby reducing the overall noise floor of the analyser [7]. If $v(t)$ represents the device noise signal, which is the quantity of interest and $e_1(t)$ and $e_2(t)$ are the noise components from the output of the amplifiers $v_1(t)$ and $v_2(t)$ are written as:

$$\begin{aligned} v_1(t) &= v(t) + e_1(t) \\ v_2(t) &= v(t) + e_2(t) \end{aligned} \tag{B.1}$$

Since, $v(t)$, $e_1(t)$, and $e_2(t)$ are noise signals, they are assumed to be uncorrelated, for all time lags τ. Such that their expectation values are given as:

$$\begin{aligned} E\{e_1(t)e_2(t+\tau)\} &= 0, \\ E\{v(t)e_i(t+\tau)\} &= 0, \quad i = 1, 2, \end{aligned} \tag{B.2}$$

Cross-correlation of the noise signals $v_1(t)$ and $v_2(t)$ is given as:

$$\begin{aligned} R_{12}(\tau) &= E\{v_1(t)v_2(t+\tau)\}, \\ &= E\{[v(t)+e_1(t)]\,[v(t+\tau)+e_2(t+\tau)]\}, \\ &= E\{v(t)v(t+\tau)\}+0, \\ &= R_{vv}(\tau), \end{aligned} \tag{B.3}$$

which is the auto-correlation function $R_{vv}(\tau)$ of the device noise. Noise terms from the amplifiers are uncorrelated with each other, hence they are eliminated. Only correlated noise from the device at the amplifier input is passed through. In the frequency domain, the Fourier transform of the cross-correlated signal $R_{12}(\tau)$, corresponds to the spectrum $S_v(f)$ as:

$$\begin{aligned} S_{12}(f) &= \int_{-\infty}^{\infty} R_{12}(\tau)e^{-j2\pi f\tau}d\tau, \\ &= \int_{-\infty}^{\infty} R_(vv)\tau e^{-j2\pi f\tau}d\tau = S_v(f), \end{aligned} \tag{B.4}$$

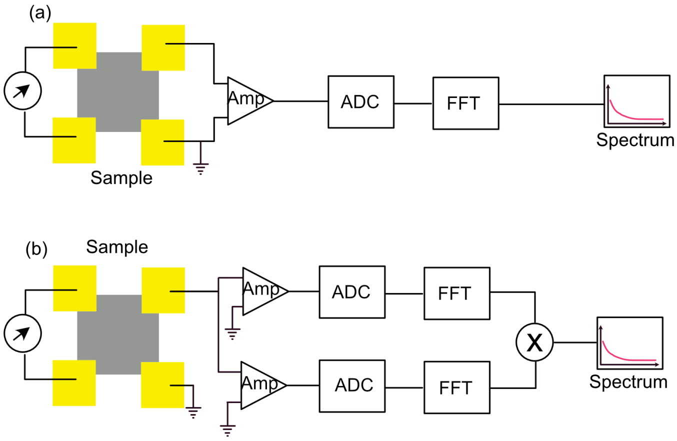

Figure B.1: (a) Single amplifier (SA) spectrum analyzer system. Here, amplifier noise is added on top of the signal of interest. (b) Schematic of cross correlation (CC) spectrum analyzer system. Cross-correlation operation eliminates uncorrelated noise components between the amplifiers, resulting in a lower noise floor for the instrument [7].

For the voltage amplification, a pair of Femto Messtechnik GmbH DLPVA 100-

F-Ds are used. For Analog to Digital Converter (ADC) National instruments NI USB-6259 and NI USB-6363 are used in synchronous mode with time delay ($\tau \sim$ ns). Fourier transform of the signals is performed and the spectrum is plotted using LabVIEW program (Figure B.1(b)).